



UNIVERSITÀ DI PISA

DEPARTMENT OF PHYSICS "*E. Fermi*"

MASTER OF SCIENCE IN PHYSICS

MASTER'S THESIS

BLACK HOLES IN MODIFIED GRAVITY THEORIES

SUPERVISOR

PROF. LEONARDO GUALTIERI

CANDIDATE

DARIO ROSSI

Academic Year

2023/2024

ABSTRACT

Einstein's General Relativity (GR) has revolutionized our understanding of gravity, marking significant advancements from Newtonian gravitational framework and leading to groundbreaking discoveries in Astrophysics and Cosmology. However, it has mostly been tested in its weak field regime. With the birth of gravitational wave (GW) astronomy we have the opportunity to study the gravitational interaction in the strong-field regime. In order to use observations by present and future GW detectors like LIGO, Virgo, LISA and the Einstein Telescope, to test general relativity in the strong-field regime, going beyond null-tests, we need to know which deviations we may expect. In particular, since most of the observed signal are produced by binary black hole mergers, we need to study how black holes (BH) behave when GR is modified. In addition, GR encounters issues when confronted with the strong-field scenarios, which further motivates the investigation of modifications to the theory.

This work deals with scalar-Gauss-Bonnet gravity (sGB). This modification of General Relativity involves the inclusion of quadratic curvature terms, precisely the Gauss-Bonnet invariant, coupled to a scalar field within the Einstein-Hilbert action. These additions represent arguably the simplest extension of GR in the large-curvature regime [8] in which BH solutions are modified. Indeed, within these theories, no-hair theorems that characterize GR black holes do not apply. Specifically, for sGB gravity, depending on the coupling function to the Gauss-Bonnet invariant, the solutions of the equations of motion can exhibit different behaviors and eventually admit BHs with non-trivial scalar hair [31], [3]. Furthermore, it is possible to manifest both hairy BHs and GR solutions simultaneously. In these scenarios, when the curvature becomes sufficiently large, a phenomenon known as *Spontaneous BH Scalarization* can occur. This mechanism allows for the emergence of hairy configurations as a result of the instability of GR solutions.

However, sGB gravity with spontaneous scalarization framework presents some issues that this thesis aims to address. The first one is that typically sGB black holes have a minimum mass for scalarized solutions, a feature that is still not fully understood. The other one is that physical solutions should be stable under radial perturbations. Through numerical investigation, the objective is to identify coupling functions capable of inducing spontaneous scalarization while ensuring stability against radial perturbations down to infinitesimal black hole masses. Furthermore, the study will explore \mathbb{Z}_2 -symmetry-violating coupling functions¹, which are usually not considered in literature, in order to pursue an Effective Field Theory approach.

This research contributes to the investigation of modified gravity theories, focusing on delving deeper into one of the most promising among them: sGB gravity. It aims to advance the exploration of physical alternative solutions to those proposed by GR, that can be tested by present and upcoming GW detectors, and introduces original aspects that have not been previously contemplated in the existing literature.

¹These include all coupling functions that are not necessarily symmetric under transformations like $\phi \rightarrow -\phi$, where ϕ is the scalar field.

Contents

1	Introduction	1
2	State of Art	5
2.1	Overview of General Relativity	5
2.1.1	Einstein equations	5
2.1.2	Black Holes	8
2.1.3	Tortoise coordinate in GR	10
2.2	Modified theories of gravity	12
2.2.1	Quadratic Gravity	13
3	Scalar-Gauss-Bonnet Gravity	17
3.1	sGB Action	17
3.1.1	Equations of motion	17
3.1.2	Evading no-hair Theorem with sGB gravity	19
3.2	Spontaneous Scalarization	20
3.2.1	Boundary and regularity conditions	21
3.2.2	Numerical implementation	23
3.3	Stability analysis	28
3.3.1	Schrödinger-like perturbed equation and boundary conditions	32
3.3.2	Sufficient condition for Bound states existence	35
3.3.3	Numerical implementation	39
3.4	Quartic coupling function	43
3.4.1	Numerical results	44
4	Exploring diverse coupling functions	49
4.1	Pure Quartic coupling function	50
4.2	Cubic coupling function	52
4.3	Exponential coupling function	56
4.3.1	Numerical results	57
4.3.2	Stability of the solutions	58
4.3.3	Effective potential analysis	60
4.3.4	Hyperbolicity Analysis	63
4.4	Lorentzian coupling function	65
5	Conclusions	71
	References	80

Appendix	I
A Perturbed equation	I
B Gravitational Waves	V

Chapter 1

Introduction

The gravitational interaction is currently well described by Einstein's General Relativity (GR), a theory that has propelled us to significant accomplishments, surpassing the gravitational law proposed by Newton. Notable achievements of this theory include the accurate prediction of the open trajectories of planets orbiting close to their stars, such as Mercury in our Solar System. Additionally, General Relativity has elucidated the phenomenon of time dilation for clocks operating at varying strengths of gravitational fields, facilitating the development of high-precision tools like GPS. Moreover, GR has unveiled "unusual" phenomena like light bending, gravitational waves (GW), and Black Holes (BH), all of them being directly demonstrated through empirical observations. Much of our understanding of Cosmology, from the Big Bang theory to the Hubble law, stems from insights derived from Einstein's theory.

Nevertheless, General Relativity has been tested experimentally mostly in the *weak-field* regime [8], principally through *null tests*. These are consistency tests, used to examine the validity of GR predictions. However, binary pulsar¹ systems, that represent the primary objects of study for conducting this type of tests, are composed of compact objects that are separated by a distance comparable to $1AU^2$, therefore they experience weak curvature effects [36].

Nonetheless, the Gravitational Wave (GW) astronomy, thanks to the LIGO-Virgo collaboration, has opened a new era in the study of the gravitational interaction, allowing us to study the strong-field regime of gravity. In particular, the observation of GW signals from the coalescence of binary black holes (BBH) represents the only available tool to study the gravitational interaction in large-curvature scenarios. In Fig. 1.1 is shown the curvature scale due to objects of mass M and radius r as $k = \sqrt{\frac{GM}{c^2 r^3}}$ (km^{-1}), with respect to the compactness parameter $\Phi = GM/c^2 r$ (dimensionless gravitational potential) for different experiments. It illustrates how current and upcoming GW observations can further investigate gravity at extreme curvature environments, thanks to the present interferometers of LIGO, Virgo and to future experiments such as Einstein Telescope and LISA.

¹A pulsar is a highly magnetized rotating Neutron Star, with typical mass of around $1 \div 2 M_\odot$ and radius of ~ 10 km. It emits beams of electromagnetic radiation out of its magnetic poles, observed with short, regular periods ($10^{-3} \div 10$ s).

²This is the Astronomical Unit, namely the average Earth-Sun distance, whose value is $\sim 1.5 \times 10^8$ km.

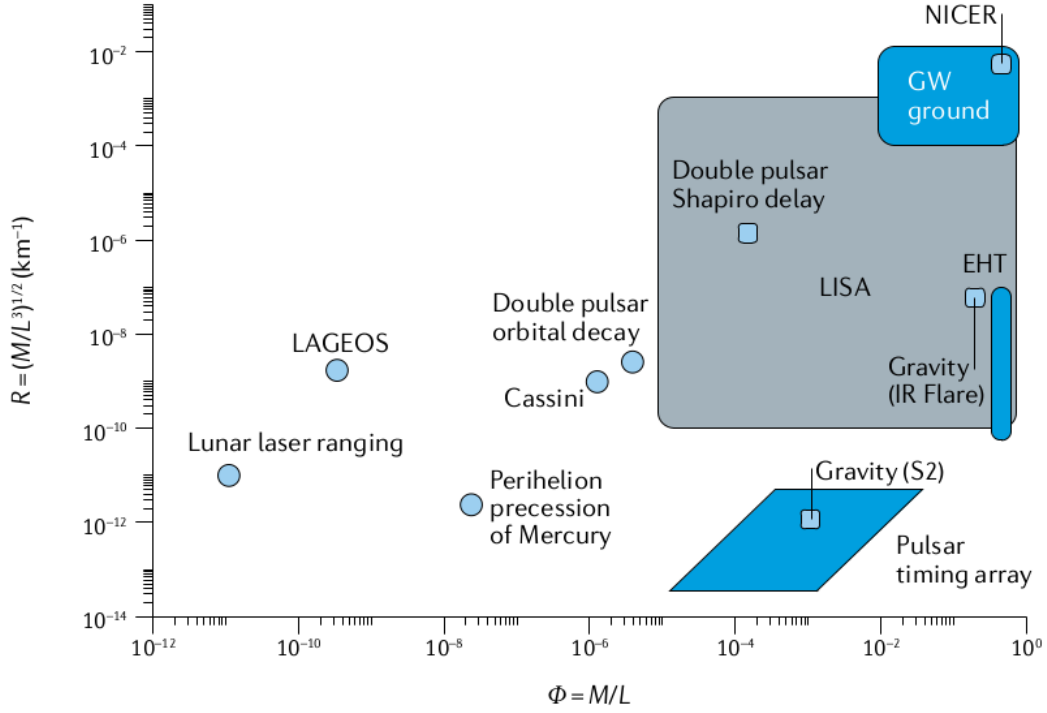


Figure 1.1: Curvature scale $k = \sqrt{\frac{GM}{c^2 r^3}}$ (km^{-1}) with respect to the compactness parameter $\Phi = GM/c^2 r$ (dimensionless gravitational potential) for different experiments. Filled circles represent past experiments that have tested GR in the weak-field regime. Rectangles and the rhombus represent ongoing or future experiments that will probe ever greater scales of curvature and compactness. LAGEOS stands for the Laser Geometric Environmental Observation Survey; NICER is the Neutron star Interior Composition Explorer; EHT stands for Event Horizon Telescope and is represented by the blue vertical rectangle; S2 and IR Flare refer to monitoring of the star S2 and near-infrared flaring near Sagittarius A*; GW ground are the ground-based GW detectors. The figure is taken from [6].

Hence, the opportunity to test GR in strong-field regime gives also the possibility to go beyond null-tests towards more informative ones, aimed to compare GR predictions against those of modified theories. This is crucial because it permits to eventually set restrictions on the validity of the latter, and constraints on the parameters that characterize them. Therefore it is important to analyze the behavior of the sources of GW signals, namely BHs, in modified gravity theories, in order to arrange significant tests.

Additionally, general relativity encounters some issue when we analyze both the *weak-field* and *strong* regimes.

The former concerns affairs related to Cosmology. The *cosmological constant problem* is a discrepancy of about 120 orders of magnitude between the theoretical and observed values of the cosmological constant. Moreover, the *cosmic coincidence problem* is an unexpected similarity of the order of magnitude of current cosmological constant and of matter density values. These issues are currently explained by assuming the existence of a still mysterious *dark energy*, but a modification of GR may provide an alternative interpretation [38].

On the other side, in large-curvature spacetime regions, for example in proximity of extreme

compact objects like Black Holes or Neutron Stars (NS), gravity becomes so strong that a quantum description is needed. GR is purely classic and cannot be renormalized in the standard quantum field sense [8]. This issue can be circumvented by high-energy corrections to the Einstein-Hilbert action. For example in [34] the authors demonstrated that adding quadratic curvature terms can lead to a renormalization of the theory. Although this does not solve the problem (the resulting theory is not unitary), it gives an indication of possible modifications of GR that should be tested.

This further motivates the investigation of corrections to the theory of gravity.

The thesis presented delves into a widely studied modification of GR for *strong-field gravity*, which is known as ***scalar-Gauss-Bonnet*** gravity (sGB). Therefore, the work will deal with the best source of large curvature of spacetime, i.e. Black Holes, close to whom gravity dominates over the other fundamental interactions.

In particular, the aim of this work is to investigate the phenomenon of *spontaneous scalarization* in sGB gravity, a mechanism that allows for the existence of BH solutions with non-trivial scalar hair when GR solutions (that have no hair) are not stable. This represents a promising alternative gravity theory, because it guarantees the validity of GR within the weak-field regime, where it has been deeply tested and verified, while providing alternative solutions when the gravitational field becomes stronger.

Such a phenomenon has been studied in the existing literature for some specific theories (see Chapter 3 for details), but still presents some open issues that need to be addressed. The main goal of this thesis is to identify conditions able to induce spontaneous scalarization while ensuring stability against radial perturbations down to infinitesimal black hole masses.

Organization of the document

The text is organized as follows.

In Chapter 2 a brief overview of the state of art in General Relativity black holes and the no-hair theorems will be provided, alongside with the introduction to the main classes of modified gravity theories, among which sGB stands in.

Chapter 3 will deal with scalar-Gauss-Bonnet gravity, focusing on spontaneous scalarization and presenting the results already obtained in literature so far. These results are of major importance for the thesis work, since they allowed to test the developed algorithms with existing results, in order to verify their viability, before presenting original contributions. Thus, all numerical results shown in this chapter have been obtained with our programs.

In Chapter 4 the original part of the thesis will be finally illustrated. Here we analyze a wider class of coupling functions to address the aim of the work written above.

Lastly, in Chapter 5 the conclusions will be drawn together with suggestions of some possible future developments of the study.

Chapter 2

State of Art

Firstly, a brief overview of Black Holes (BH) in General Relativity (GR) should be useful for follow-up.

2.1 Overview of General Relativity

2.1.1 Einstein equations

The Einstein-Hilbert action is defined as

$$S = \frac{1}{2} \int d^4x \sqrt{|g|} R, \quad (2.1)$$

where g is the determinant of the metric tensor $g_{\mu\nu}$, that is taken with the mostly-plus signature $(-1,1,1,1)$; R is the Ricci scalar, obtained by the trace of the Ricci tensor $R_{\mu\nu}$. It is possible to add a matter action S_{mat} to include the effects of matter fields on the spacetime configuration.

Notably, here and after units such that $8\pi G = c = 1$ are used, where c is the speed of light and G the Newtonian gravitational constant. These are the units usually employed in the literature for studying black holes [22].

Ricci tensor $R_{\mu\nu}$, in turn, is computed as the trace (between indexes α and β) of Riemann tensor $R_{\beta\mu}{}^{\alpha}{}_{\nu}$, whose components are

$$R_{\beta\mu}{}^{\alpha}{}_{\nu} = \nabla_{\beta} \Gamma_{\mu}{}^{\alpha}{}_{\nu} - \nabla_{\mu} \Gamma_{\beta}{}^{\alpha}{}_{\nu} + \Gamma_{\beta}{}^{\rho}{}_{\nu} \Gamma_{\mu}{}^{\alpha}{}_{\rho} - \Gamma_{\mu}{}^{\rho}{}_{\nu} \Gamma_{\beta}{}^{\alpha}{}_{\rho}. \quad (2.2)$$

The ∇_{μ} symbol represents the affine connection (or covariant derivative) that acts on vectors (covectors) A^{μ} (A_{μ}) like

$$\nabla_{\mu} A^{\nu} = \partial_{\mu} A^{\nu} \pm \Gamma_{\mu}{}^{\nu}{}_{\alpha} A^{\alpha}, \quad (2.3)$$

where the minus sign stands for covectors.

$\Gamma_{\mu}{}^{\nu}{}_{\alpha}$ are the Christoffel symbols, whose components for a metric and symmetric connection¹ are written, in terms of $g_{\mu\nu}$, as

$$\Gamma_{\mu}{}^{\alpha}{}_{\beta} = \frac{1}{2} g^{\alpha\gamma} (\partial_{\mu} g_{\gamma\beta} + \partial_{\beta} g_{\mu\gamma} - \partial_{\gamma} g_{\mu\beta}) \quad (2.4)$$

¹An affine connection is said to be metric-compatible when it vanishes when evaluated on $g_{\mu\nu}$; it is symmetric if the torsion tensor $T_{\mu}{}^{\nu}{}_{\alpha} = \Gamma_{\mu}{}^{\nu}{}_{\alpha} - \Gamma_{\alpha}{}^{\nu}{}_{\mu}$ is identically null.

In this case, ∇_μ is called *Levi-Civita* connection. It is notable that the Christoffel symbols are not tensors, as they transform under coordinate system changing $x^\mu \rightarrow y^\mu$ like

$$\tilde{\Gamma}^\gamma{}_\mu{}^\alpha{}_\beta = \frac{\partial x^\rho}{\partial y^\mu} \frac{\partial y^\alpha}{\partial x^\sigma} \frac{\partial x^\gamma}{\partial y^\beta} \Gamma^\sigma{}_\rho{}^\gamma{}_\sigma + \frac{\partial y^\alpha}{\partial x^\rho} \frac{\partial^2 y^\rho}{\partial y^\mu \partial y^\beta}. \quad (2.5)$$

where $\tilde{\Gamma}^\gamma{}_\mu{}^\alpha{}_\beta$ are the Christoffel symbols in the new coordinate system.

Nevertheless, the difference between two Christoffel symbols, like the torsion $T_\mu{}^\nu{}_\alpha = \Gamma_\mu{}^\nu{}_\alpha - \Gamma_\alpha{}^\nu{}_\mu$, are tensors, since the second term in the right-hand side of the equation above simplifies, as it does not depend on the connection but only on the transformation of the coordinates.

Killing vectors

A vector $\vec{\xi}(x^\mu)$, defined at every point in spacetime, can identify a symmetry of the metric, when an infinitesimal translation along $\vec{\xi}$ leaves the line element $ds^2 = g_{\mu\nu} dx^\mu dx^\nu$ unchanged. Namely, the metric is invariant under the transformation $x^\mu \rightarrow x^\mu + \varepsilon \xi^\mu$. The variation of the line element is

$$0 = \delta(ds^2) = \delta(g_{\mu\nu} dx^\mu dx^\nu) = \delta g_{\mu\nu} dx^\mu dx^\nu + g_{\mu\nu} [\delta(dx^\mu) dx^\nu + dx^\mu \delta(dx^\nu)]. \quad (2.6)$$

If we write $\delta(dx^\mu) = x'^\mu - x^\mu = \xi^\mu \delta\lambda$, with λ that parametrizes the curve $\xi_\mu = \frac{dx^\mu}{d\lambda}$ tangent to the direction of $\vec{\xi}$, then Eq. 2.6 can be written as

$$g_{\mu\nu,\alpha} \xi^\alpha \delta\lambda dx^\mu dx^\nu + g_{\mu\nu} [\xi^\mu{}_{,\alpha} dx^\alpha \delta\lambda dx^\nu + \xi^\nu{}_{,\gamma} dx^\mu \delta\lambda dx^\gamma] = 0 \quad (2.7)$$

and relabeling indexes

$$[g_{\mu\nu,\alpha} \xi^\alpha + g_{\gamma\nu} \xi^\gamma{}_{,\mu} + g_{\mu\gamma} \xi^\gamma{}_{,\nu}] dx^\mu dx^\nu \delta\lambda = 0. \quad (2.8)$$

The notation $f_{,\mu}$ stands for the partial derivative with respect to x^μ .

The *Killing equation* that has to be satisfied by a **Killing vector** ξ^μ which generates a symmetry of the metric is

$$g_{\mu\nu,\alpha} \xi^\alpha + g_{\gamma\nu} \xi^\gamma{}_{,\mu} + g_{\mu\gamma} \xi^\gamma{}_{,\nu} = 0. \quad (2.9)$$

Actually, the physically proper **Killing equation** is the one written in the covariant form

$$\xi_{\mu;\nu} + \xi_{\nu;\mu} = 0. \quad (2.10)$$

where the symbol $_{;\mu}$ is used to represent the covariant derivative ∇_μ .

Indeed, using the Levi-Civita connection (Eq. 2.4) it is possible to demonstrate that

$$g_{\mu\nu,\alpha} = g_{\mu\gamma} \Gamma^\gamma{}_\nu{}_\alpha + g_{\nu\gamma} \Gamma^\gamma{}_\mu{}_\alpha \quad (2.11)$$

and writing explicitly the covariant derivative in Eq. 2.10 follows Eq. 2.9.

Einstein Equation

The equations of motion can be found by applying variational principle to the Einstein-Hilbert action, varying with respect to the metric.

The action has three terms depending on $g_{\mu\nu}$, since the integrand can be written as $\frac{1}{2}\sqrt{|g|}g^{\mu\nu}R_{\mu\nu}$. Note that $g^{\mu\nu}$ is the inverse of the metric tensor and it is used to raise lower indexes. In this case it permits to obtain the trace of Ricci tensor, which is of rank (0,2). Hence, we must compute $\delta\sqrt{|g|}$ and $\delta R_{\mu\nu}$.

For the former, it is useful considering that the determinant of the exponential of a generic matrix A is $\det[\exp(A)] = \exp(\text{Tr}(A))$ with $\text{Tr}(A)$ being the matrix trace. Naming $A = \ln(g_{\mu\nu})$ and plugging it into the aforementioned relation, it follows

$$\det(g_{\mu\nu}) = e^{\text{Tr}(\ln(g_{\mu\nu}))}. \quad (2.12)$$

Now differentiating with respect to the metric yields

$$\partial_\mu \sqrt{|g|} = \frac{1}{2} \sqrt{|g|} g^{\alpha\beta} \partial_\mu g_{\alpha\beta}. \quad (2.13)$$

Using Eq. 2.4 and tracing over the last two indexes, it is possible to derive the following relation

$$\partial_\mu \sqrt{|g|} = \sqrt{|g|} \Gamma_\mu^\alpha{}_\alpha \quad (2.14)$$

that will be useful later-on.

For the derivative of Ricci tensor, Palatini identity can be employed, i.e. the relation between the variation of the Riemann tensor and the variation of the connection [25]:

$$\delta R_{\mu\nu}{}^\alpha{}_\beta = \nabla_\mu \delta \Gamma_\nu{}^\alpha{}_\beta - \nabla_\nu \delta \Gamma_\mu{}^\alpha{}_\beta. \quad (2.15)$$

Thus the variation of the Ricci tensor is

$$g^{\mu\nu} \delta R_{\mu\nu} = g^{\mu\nu} [\delta \Gamma_\mu{}^\gamma{}_{\nu;\gamma} - \delta \Gamma_\gamma{}^\gamma{}_{\nu;\mu}] = \nabla_\mu [\delta \Gamma_\alpha{}^\mu{}_\beta g^{\alpha\beta} - \delta \Gamma_\gamma{}^\gamma{}_\nu g^{\mu\nu}] = \nabla_\mu V^\mu. \quad (2.16)$$

In addition, the metricity of the connection, according to which $g_{\mu\nu;\gamma} = 0$, has been employed. Note that V^μ is a vector since it is a composition of properly defined vectors, from the fact that $\delta \Gamma_\mu{}^\gamma{}_\nu$ is a tensor, as highlighted above.

Everything is ready to apply variational principle to Eq. 2.1 writing $\delta S = 0$:

$$\begin{aligned} \delta S &= \frac{1}{2} \int d^4x \left[\delta(\sqrt{|g|}) R + \delta(g^{\mu\nu}) R_{\mu\nu} \sqrt{|g|} + \delta(R_{\mu\nu}) g^{\mu\nu} \sqrt{|g|} \right] + \delta S_{mat} = \\ &= \frac{1}{2} \int_M d^4x \sqrt{|g|} \left(-R^{\mu\nu} + \frac{1}{2} R g^{\mu\nu} \right) \delta g_{\mu\nu} + \int_M V^\alpha{}_{;\alpha} \sqrt{|g|} + \delta S_{mat} = 0. \end{aligned} \quad (2.17)$$

Here we used the relation $0 = \delta(\delta^\mu_\nu) = \delta(g^{\mu\alpha} g_{\alpha\nu}) = \delta(g^{\mu\alpha}) g_{\alpha\nu} + g^{\mu\alpha} \delta(g_{\alpha\nu})$ to collect $\delta(g_{\alpha\nu})$.

Then using Eq. 2.14 it is possible to show that $\sqrt{|g|} V^\alpha{}_{;\alpha} = \partial_\mu (\sqrt{|g|} V^\mu)$. From Stokes theorem [27], it follows that $\int_M V^\alpha{}_{;\alpha} \sqrt{|g|} = \int_{\partial M} \sqrt{\gamma} V^\alpha n_\alpha$, where $\gamma = \det(\gamma_{ij})$ is the determinant of the metric induced by $g_{\mu\nu}$ on the boundary of the manifold M denoted by ∂M , and n^α represents its normal vector. This boundary term vanishes for boundless manifolds or if the

variation of the metric is null at boundaries. This is an additional condition that should be imposed. However, adding to the Einstein-Hilbert action a proper boundary contribution, namely the Gibbons-Hawking-York term [17], the surface term above can be simplified when the variational principle is applied, without changing the equations of motions.

In the end, calling the **Einstein Tensor**

$$G_{\mu\nu} = R_{\mu\nu} - \frac{1}{2}Rg_{\mu\nu} \quad (2.18)$$

and the **stress-energy tensor**

$$T^{\mu\nu} = \frac{2}{\sqrt{|g|}} \frac{\delta S_{mat}}{\delta g_{\mu\nu}} \quad (2.19)$$

we can finally write the famous Einstein Equation

$$G_{\mu\nu} = T_{\mu\nu} \quad (2.20)$$

2.1.2 Black Holes

A black hole is a particular solution of Eq. 2.20 with $T_{\mu\nu} = 0$, i.e. in vacuum. It is an extremely compact massive body such that its gravitational field is capable to prevent anything, including light, from escaping. In general, black holes are any solutions of the Einstein equations with a curvature singularity enclosed in an event horizon. The *event horizon* (EH) is defined as the surface beyond which the escape velocity of particles exceeds the speed of light, therefore making it impossible for any kind of particle to fly away from there. The *Schwarzschild radius* R_s is the critical distance from the center of a non-rotating spherical object beyond which the latter must be compressed in order to become a black hole. For spherically symmetric static BHs the EH is a sphere of radius exactly equal to R_s . The Schwarzschild radius can be classically computed as $R_s = 2M$, with M being the mass of the BH.

The line element $ds^2 = g_{\mu\nu}dx^\mu dx^\nu$ for a generic static and spherically symmetric spacetime can be written, in a spherical coordinate system $(t, r, \theta, \varphi)^2$, as

$$ds^2 = -A(r)dt^2 + B(r)^{-1}dr^2 + r^2(d\theta^2 + \sin^2(\theta)d\varphi^2) \quad (2.21)$$

where A and B only depend on the radial distance r from the BH center and are called *metric functions*.

Using this kind of metric and the symmetries mentioned above it is possible to solve Eq. 2.20 in vacuum (with $T_{\mu\nu} = 0$), getting the **Schwarzschild metric**, whose line element is

$$ds^2 = -\left(1 - \frac{R_s}{r}\right)dt^2 + \frac{1}{\left(1 - \frac{R_s}{r}\right)}dr^2 + r^2(d\theta^2 + \sin^2(\theta)d\varphi^2). \quad (2.22)$$

We can see how the metric becomes singular for $r \rightarrow R_s$ and for $r \rightarrow 0$. The former is actually just an apparent singularity, due to the selected coordinate system, as showed in Sec. 2.1.3. Conversely, towards the center of the BH the singularity of the metric represents a real singularity of the spacetime, where the curvature becomes infinite. In order to demonstrate

²Where t is the coordinate related to "time", r the radial distance, θ the zenithal angle and φ the azimuthal angle.

this, we can determine the curvature of the spacetime by computing the Kretschmann scalar $K = R_{\mu\nu\alpha\beta}R^{\mu\nu\alpha\beta}$, which for Schwarzschild metric is

$$K_{Schw} = \left[R_{\mu\nu\alpha\beta}R^{\mu\nu\alpha\beta} \right]_{Schw} = 12 \frac{r_h^2}{r^6}, \quad (2.23)$$

where r_h is the horizon radius. Thus, it is straightforward from Eq. 2.23 that the curvature diverges as r tends to 0. In the following section Sec. 2.1.3 a brief parenthesis on the fictitious singularity that arises in Schwarzschild coordinate at the EH is presented, and it will be extremely useful for the following chapters either.

The Schwarzschild result can be generalized to rotating BHs with axisymmetric spacetime yielding the *Kerr metric*

$$ds^2 = \left(1 - \frac{R_s r}{\rho^2} \right) c^2 dt^2 - \frac{\rho^2}{\Delta} dr^2 - \rho^2 d\theta^2 + \\ - \left(r^2 + \alpha^2 + \frac{R_s r \alpha^2}{\rho^2} \sin^2 \theta \right) \sin^2 \theta d\varphi^2 + \frac{2R_s r \alpha \sin^2 \theta}{\rho^2} dt d\varphi, \quad (2.24)$$

where

$$R_s = 2M, \quad \rho^2 = r^2 + \alpha^2 \cos^2 \theta, \quad \Delta = (r^2 - R_s r + \alpha^2), \quad \alpha = \frac{J}{M}$$

with J the angular momentum. We can see that in the spinless limit $\alpha \rightarrow 0$ we obtain Eq. 2.22 again as expected.

No-Hair theorem In the second half of XX century, lots of physicists stated that, within General Relativity, black holes are only described by 2 free parameters only (3 including electromagnetic charge): its mass and angular momentum³. Therefore, choosing a proper reference frame, Kerr metric (Eq. 2.24) is the unique external spacetime solution [13] of the Einstein Equation Eq. 2.20. This means that the only thing that affects the geometry of spacetime around such kind of celestial objects is how much mass is enclosed within its event horizon and how much it spins. Even the type of matter that composes the mass inside the BH becomes irrelevant: nor Baryon nor Lepton numbers, neither whether it is matter or antimatter or any other additional characteristic are important. J. A. Wheeler expressed this feature saying that "Black Holes have no hair", from which the name of the conjecture. Rigorous mathematical proof in the case of stationary black holes can be found in [19].

However, modified gravity theories can elude the statement and include additional "hair", like scalar-Gauss-Bonnet gravity that is studied in this thesis. Since this theorem characterizes completely black holes in general relativity, only theories that admit solutions with additional degrees of freedom can modify effectively the phenomenology of BHs.

³Reissner-Nordström and Kerr-Newman metrics are the ones that describe respectively electric charged static and rotating black holes, see [2] for an overview.

2.1.3 Tortoise coordinate in GR

Let us write again Schwarzschild metric in GR

$$ds^2 = -\left(1 - \frac{R_s}{r}\right) dt^2 + \frac{1}{\left(1 - \frac{R_s}{r}\right)} dr^2 + r^2(d\theta^2 + \sin^2(\theta)d\varphi^2). \quad (2.25)$$

We already said that when $r \rightarrow R_s$ we have an apparent singularity, but we have not shown yet why it is called "apparent".

Take into account light world-lines, i.e. null geodesics for which $ds^2 = 0$. We consider radial motions where $d\Omega^2 = d\theta^2 + \sin^2(\theta)d\varphi^2 = 0$. Thus, from Eq. 2.22 it follows

$$0 = \left(1 - \frac{R_s}{r}\right) dt^2 + \frac{1}{\left(1 - \frac{R_s}{r}\right)} dr^2, \quad (2.26)$$

therefore

$$\frac{dt}{dr} = \left(1 - \frac{R_s}{r}\right)^{-1}. \quad (2.27)$$

We can now integrate by parts Eq. 2.27 with respect to r obtaining

$$t = \int \frac{1}{1 - \frac{R_s}{r}} dr = r + R_s \ln |r - R_s|. \quad (2.28)$$

From Eq. 2.28 it is notable that when $r \rightarrow R_s$ the time t diverges, meaning that light in Schwarzschild coordinate takes infinite time to reach the event horizon.

Nevertheless this issue can be circumvented by naming the **tortoise coordinate**

$$r_* = r + R_s \ln \left| \frac{r}{R_s} - 1 \right| \quad (2.29)$$

and changing variables in favour of **Eddington-Finkelstein** coordinates, defined as

$$v = t + r_* \quad \text{for ingoing rays} \quad (2.30)$$

$$u = t - r_* \quad \text{for outgoing rays.} \quad (2.31)$$

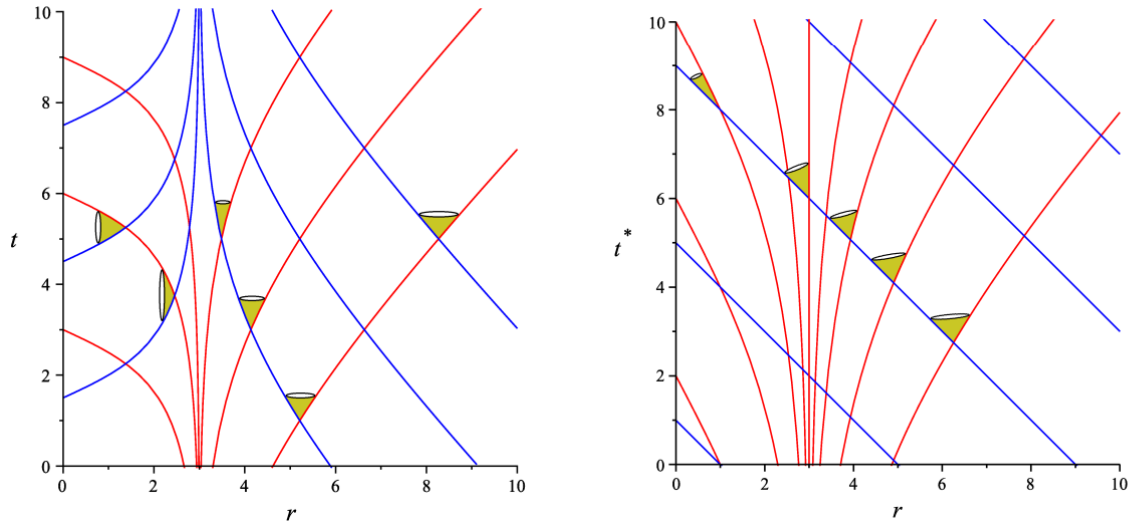
This definition can be justified if we write Schwarzschild's metric (with $d\Omega^2 = 0$) like

$$ds^2 = -F \left(dt - \frac{1}{F} dr \right) \left(dt + \frac{1}{F} dr \right) = -F du dv \quad (2.32)$$

with $F = 1 - R_s/r$. Hence, if we take the couple (u, v) as new coordinates, the metric remains still singular at the horizon. On the contrary, if the two of them are taken as new "time" coordinates, coupled together with Schwarzschild radial coordinate r - i.e. (v, r) and (u, r) separately - the line element can be written as

$$ds^2 = -\left(1 - \frac{R_s}{r}\right) dv^2 + 2dvdr + r^2 d\Omega^2 \quad (2.33)$$

$$ds^2 = -\left(1 - \frac{R_s}{r}\right) du^2 + 2dvdr + r^2 d\Omega^2. \quad (2.34)$$



(a) Scheme representing radial ingoing and outgoing rays with Schwarzschild coordinates (t, r) .

(b) Scheme representing radial ingoing and outgoing rays with coordinates (v, r) of Eddington-Finkelstein.

Figure 2.1: In these scheme, taken from [28], we can appreciate how the event horizon is never reached by light in the case of Fig. 2.1a, and how the light cone shrinks towards that surface; in Fig. 2.1b on the contrary the EH is a normal passing point for light, and it only signs the passage from time-like Killing vector $(1, 0, 0, 0)$ to a space-like one coming from outside and going into the BH.

The former stands for ingoing particles, with radial light rays satisfying equation $v = \text{const}$; the latter for outgoing ones (radial light rays $u = \text{const}$).

Now we can see how the metric is no more singular for $r \rightarrow R_s$, even if the element $(0, 0)$ of the metric vanishes, because of the presence of the mixing term between the new temporal coordinate and r .

Thus we have solved the fictitious singularity of the event horizon just by changing coordinate system.

Note lastly that with r_* the EH is moved to $-\infty$ so the range of space can be mapped in whole \mathbb{R} .

The tortoise coordinate name comes from the famous paradox "Achilles and the tortoise" by Zeno. The name refers to the fact that, according to the paradox, Achilles cannot reach the turtle in finite time if it starts walking a little further then him, even if he is way faster, so light cannot reach the event horizon if we analyze the problem with Schwarzschild time coordinate.

2.2 Modified theories of gravity

As already mentioned, cosmological observation and fundamental physics considerations suggest that GR must be extended to solve the problems occurring at very low and very high energies. Therefore we need to renounce at least to one of the assumptions on which Einstein's GR is constructed. Indeed, Lovelock's theorem states that GR emerges as the unique theory of gravity under specific hypothesis [8].

Lovelock Theorem *In 4 spacetime dimensions the only divergence-free symmetric rank-2 tensor constructed solely from the metric $g_{\mu\nu}$ and its derivatives up to second differential order, and preserving diffeomorphism invariance, is the Einstein tensor plus a cosmological term.*

This theorem naturally brings to Einstein's field equations Eq. 2.20 with the addition of a cosmological constant Λ term: $G_{\mu\nu} + \Lambda g_{\mu\nu} = T_{\mu\nu}$.
From the metricity of the affine connection together with second Bianchi identity

$$R_{\mu\nu}{}^{\alpha}{}_{\beta;\rho} + R_{\nu\rho}{}^{\alpha}{}_{\beta;\mu} + R_{\rho\mu}{}^{\alpha}{}_{\beta;\nu} = 0 \quad (2.35)$$

follows that $G_{\mu\nu}$ is divergence free and so the stress-energy tensor is, using Einstein equations. This implies that geodesic equation

$$u^{\mu}\nabla_{\mu}u^{\nu} = 0, \quad (2.36)$$

where u^{μ} is the 4-velocity of the particle, depends just on the gravitational field in which the test particle is moving, guaranteeing the *weak equivalence principle* (WEP), i.e. the universality of free fall⁴. The WEP is included in the *strong equivalence principle* (SEP), which states the universality of free-fall (i.e. the equality of gravitational and inertial masses), the local Lorentz invariance (which implies that the laws of physics are the same in all locally inertial reference frames), and local position invariance (which implies that the outcome of any local non-gravitational experiment is independent of where and when in the universe it is performed). In other words, a freely falling frame can cancel out the effects of a gravitational field, making the local laws of physics appear as they would in the absence of gravity.

Upon detailed analysis, the theorem has several assumptions. By relaxing some of these assumptions, it is possible to circumvent its thesis and develop modified theories. There are at least four ways to accomplish this task:

- **Additional fields:** adding manually extra degrees of freedom in the action coupling non-minimally with the metric
 - *Dynamical fields.* This leaves more options to construct the left-hand side of Eq. 2.20, but the SEP is usually violated due to the coupling with additional dynamical fields.
 - *Non-Dynamical fields.* In this way the left-hand side of Einstein's equation is left unchanged, $T_{\mu\nu}$ keeps on being divergence free but it appears non-linearly in the equation. The WEP is preserved, and the theory only differs from General Relativity (GR) in its coupling to matter.

⁴All uncharged, freely falling test particles, regardless of their composition, follow the same trajectories, once an initial position and velocity have been prescribed.

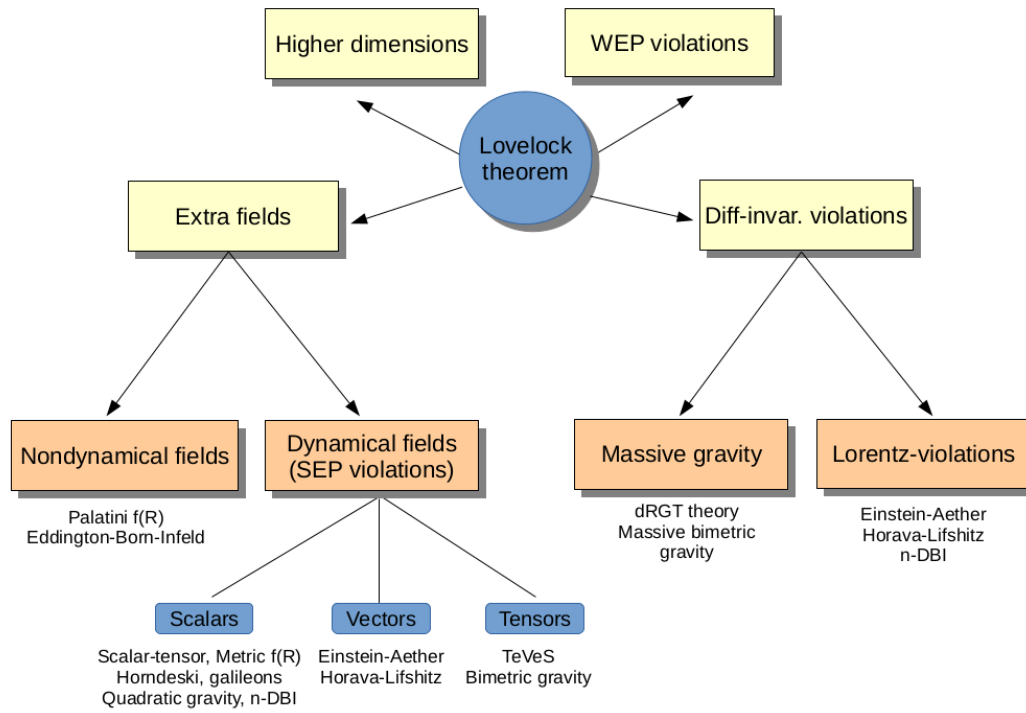


Figure 2.2: A diagram exposed in [8] that sums up all the classes of modified theories of gravity, starting from Lovelock's theorem.

- **Violation of Diffeomorphism invariance:** theories of this kind arise by considering Lorentz invariance as an emergent symmetry that is broken at high energies or by assuming the mediator of gravity to be massive instead of massless.
- **Higher Dimension:** if the assumption of four spacetime dimensions is neglected, even while adhering to all other assumptions of Lovelock's theorem, the Einstein-Hilbert action is no longer unique. It becomes interesting to explore how the gravitational field behaves when considering the spacetime dimension as a variable parameter.
- **WEP violation:** just considering a non-minimal coupling to the matter sector Weak Equivalence Principle is violated. However, theories incorporating this assumption are not very credible, as the WEP has been tested with a precision of one part in 10^{13} .

For a complete overview on all the possible theories beyond GR and the references to the related articles, Berti et al. paper [8] is worth a lecture. Here it is reported from that paper a diagram in Fig. 2.2 summing up the possible modification of Einstein's gravity exposed above.

2.2.1 Quadratic Gravity

As previously mentioned, General Relativity (GR) is not renormalizable within the framework of quantum field theory (QFT), which is a significant obstacle to developing a quantum theory of gravity. However, if the Einstein-Hilbert action is considered the first term in an effective field theory (EFT) expansion that includes all possible curvature invariants, this

perspective may provide new insights⁵. Adding higher-order curvature terms to the Einstein-Hilbert action can benefit the theory, as demonstrated in [34]. It is crucial to stress that the resulting theory is not a viable QFT of gravity at high energy, but it suggests that such theories could represent an effective field theory description, way below the Planck energy scale, of a still unknown quantum model of gravity. Still, even at low energies, these additions introduce higher-derivative terms in the field equations, potentially leading to pathologies (the so-called Ostrogradsky instability [38]).

Considering terms up to the second power of curvature, the aforementioned problem can be avoided by carefully selecting the proper combination of algebraically independent quadratic curvature invariants. These are

$$R^2 \quad R_{\mu\nu}^2 \quad R_{\mu\nu\alpha\beta}^2 \quad {}^*RR \quad (2.37)$$

where the last term is ${}^*RR \equiv \frac{1}{2} R_{\mu\nu\rho\sigma} \epsilon^{\nu\mu\lambda\kappa} R_{\rho\sigma\lambda\kappa}$. The Gauss-Bonnet term

$$\mathcal{G} = R^2 - 4R_{\mu\nu}R^{\mu\nu} + R_{\mu\nu\alpha\beta}R^{\mu\nu\alpha\beta}. \quad (2.38)$$

represents exactly the unique combination of these terms that we were looking for.

The GB term in 4 spacetime dimensions yields a boundary term contribution since it is a total divergence (brief demonstration in [33]), so it does not affect the field equation for the metric if it stands alone in the action. Conversely, coupling this term to an extra dynamical field (scalar for simplicity), the related term does not disappear, entering the equation of motion non-trivially. Moreover, due to the vanishing of its divergence, the GB term is the only quadratic curvature contribution that leads to second order equation of motion, free from pathological degrees of freedom.

In this thesis we shall delve deeper into scalar-Gauss-Bonnet gravity (sGB), which is located in the branch of "extra dynamical fields" of Fig. 2.2.

⁵This approach is also suggested by low-energy effective string theory [18].

Chapter 3

Scalar-Gauss-Bonnet Gravity

This chapter is dedicated to introduce the theory of scalar-Gauss-Bonnet gravity and the phenomenon of spontaneous scalarization of BHs. In particular two different coupling functions will be examined, the quadratic and the quadratic+quartic couplings. Both of them have already been widely studied in literature (e.g. [31], [30], [22]). The results presented in this chapter are not original, but they are all computed through the algorithms that we have implemented. Original contributions will be reported all in Chap. 4.

3.1 sGB Action

The action of scalar-Gauss-Bonnet gravity with general coupling is [31]

$$S = \frac{1}{2} \int d^4x \sqrt{|g|} \left(R - \frac{1}{2} \nabla_\mu \phi \nabla^\mu \phi + V(\phi) + \mathcal{F}(\phi) \mathcal{G} \right) + S_{mat} \quad (3.1)$$

where g is the determinant of the metric tensor $g_{\mu\nu}$, $V(\phi)$ is the potential for the scalar field, $\mathcal{F}(\phi)$ a generic coupling function (which depends only on ϕ) between the scalar field ϕ and the Gauss-Bonnet (GB) invariant term \mathcal{G} .

For our study we will consider for simplicity the case $V = 0$, i.e. of a massless scalar field without self-interaction.

3.1.1 Equations of motion

At first, the action Eq. 3.1 can be varied with respect to the scalar field ϕ . We can neglect the matter action contribution since we are going to study BH solutions, therefore in vacuum. Expressing $\nabla_\mu \phi \nabla^\mu \phi = g_{\mu\nu} \phi_{;\mu} \phi_{;\nu}$ and twisting it by parts we get ¹

$$\delta_\phi S = \int d^4x \delta \phi \left[\partial_\mu (\sqrt{g} \partial^\mu \phi) + \mathcal{F}'(\phi) \sqrt{g} \mathcal{G} \right] = 0 \quad (3.2)$$

Then, from Eq. 2.14 we can write $\frac{1}{\sqrt{g}} \partial_\mu (\sqrt{g} \partial^\mu \phi) = \nabla_\mu \partial^\mu \phi = \nabla_\mu \nabla^\mu \phi = \square \phi$ ², so the final equation of motion for the scalar field is

$$\square \phi = -\mathcal{F}'(\phi) \mathcal{G} \quad (3.3)$$

¹Hereinafter g stays for $|g|$ for brevity.

²The \square is the d'Alembertian operator.

where the prime indicates the derivative of the coupling function \mathcal{F} with respect to the field.

Next, differentiate the action with respect to the metric. In order to do that, we need to explicit the dependence of all the terms in Eq. 2.1 from $g_{\mu\nu}$, e.g. in the Ricci scalar or in the kinetic part of the scalar field Lagrangian. We already know from Eq. 2.17 that the Ricci term returns the Einstein's tensor $G_{\mu\nu}$ after applying variational principle. In the end, we get ([22],[21])

$$G_{\mu\nu} = T_{\mu\nu}^\phi - \mathcal{K}_{\mu\nu} \quad (3.4)$$

where

$$T_{\mu\nu}^\phi = \frac{1}{2} \partial_\mu \phi \partial_\nu \phi - \frac{1}{4} g_{\mu\nu} (\partial_\alpha \phi)^2 \quad (3.5)$$

$$\mathcal{K}_{\mu\nu} = g_{\alpha(\mu} g_{\nu)\beta} \epsilon^{\rho\beta\sigma\tau} \nabla_\lambda [{}^* R^{\alpha\lambda}_{\sigma\tau} \mathcal{F}'(\phi) \nabla_\rho \phi] \quad (3.6)$$

with $T_{\mu\nu}^\phi$ associated to the kinetic part for ϕ in the action and $\mathcal{K}_{\mu\nu}$ related to the GB term coupled with the scalar field (see [33] for the analytical derivation). $T_{\mu\nu}^\phi$ is actually the stress-energy tensor coming out of a matter action of a free massless scalar particle. In Eq. 3.6 the parenthesis around indexes means symmetrization: $g_{\alpha(\mu} g_{\nu)\beta} = \frac{1}{2} (g_{\alpha\mu} g_{\nu\beta} + g_{\alpha\nu} g_{\mu\beta})$. $\epsilon^{\rho\beta\sigma\tau}$ is the Levi-Civita tensor, with $\epsilon^{0123} = \frac{1}{\sqrt{g}}$. Lastly, ${}^* R^{\alpha\lambda}_{\sigma\tau}$ represents the dual Riemann tensor obtained as ${}^* R^{\alpha\lambda}_{\sigma\tau} = \epsilon^{\alpha\lambda\alpha'\lambda'} R_{\alpha'\lambda'\sigma\tau}$.

To summarize, starting from the action of sGB gravity, we derive a generalized form of Einstein's equation (Eq. 2.20) featuring a modified effective stress-energy tensor. This modification arises from the presence of the scalar field and the Gauss-Bonnet term coupled to it (Eq. 3.4). Additionally, we obtain a separate field equation for the scalar field ϕ (Eq. 3.3), which manifests as a Klein-Gordon equation with a source term resulting from the Gauss-Bonnet coupling

$$G_{\mu\nu} = T_{\mu\nu}^\phi - \mathcal{K}_{\mu\nu} \quad (3.7)$$

$$\square \phi = -\mathcal{F}'(\phi) \mathcal{G} \quad (3.8)$$

It is also evident from Eqs. 3.7,3.8 that if the scalar field is constant at a certain value ϕ_0 and if the coupling function has null derivative at that value,

$$\mathcal{F}'(\phi_0) = 0 \quad (3.9)$$

then we can obtain the GR equation Eq. 2.20 in vacuum again. So GR solutions such as Kerr and Schwarzschild ones are enclosed in sGB theory if we consider particular coupling functions that satisfies condition Eq. 3.9 for a certain ϕ_0 .

In this thesis we will only take into account theories that satisfy Eq. 3.9, since we are interested in the spontaneous scalarization phenomenon and because we want GR to be a particular case of the new models. Therefore, we will exclude theories like Einstein-dilaton-Gauss-Bonnet gravity³ (EdGB) analyzed for example in [21],[20] or in [26], where the coupling function is $\propto e^\phi$, which is derived from low-energy effective string theory [18], but that does not fulfill the condition here imposed.

³See [24] for more details.

3.1.2 Evading no-hair Theorem with sGB gravity

In this section we demonstrate how sGB gravity can elude the no-hair theorem, which states that black holes are uniquely described by their mass and angular momentum in General Relativity.

The symmetries of a metric can be expressed in terms of *Killing vectors* ξ^μ , that satisfy the *Killing equation* Eq. 2.10 exposed in Chap. 2. For example, time-like⁴ Killing vectors are associated to the invariance under time translations.

In papers [31] and [3] it is shown how to elude no-hair theorems within sGB gravity framework, with a proof that is quiet similar to the one in [32] for generic scalar tensor theories.

Taking into account BH solutions that are asymptotically flat and stationary, these admit a Killing vector ξ^μ that is time-like at infinity and acts as a generator of the event horizon. In fact, the event horizon, defined in Chap. 2, can be also identified as the surface where the time-like Killing vector changes its norm, becoming null. Assuming that ϕ respects stationarity, namely $\xi_\mu \phi_{;\mu} = 0$, we can multiply Eq. 3.3 by $\mathcal{F}'(\phi)$ and integrate the equation in a volume \mathcal{V}

$$\int_{\mathcal{V}} d^4x \sqrt{g} \left[\mathcal{F}'(\phi) \square \phi + (\mathcal{F}'(\phi))^2 \mathcal{G} \right] = 0. \quad (3.10)$$

Integrating by parts the first term and using Stokes theorem we obtain

$$\int_{\mathcal{V}} d^4x \sqrt{g} \left[\mathcal{F}''(\phi) \phi_{;\mu}^2 - (\mathcal{F}'(\phi))^2 \mathcal{G} \right] = \int_{\partial\mathcal{V}} d^3x \sqrt{h} \mathcal{F}'(\phi) n^\mu \phi_{;\mu} \quad (3.11)$$

where $\partial\mathcal{V}$ is the boundary of the volume, n_μ is the normal versor to the boundary, h is the determinant of the 3-D spatial metric induced by $g_{\mu\nu}$ on $\partial\mathcal{V}$. We choose \mathcal{V} such that it is bounded by the BH horizon, spatial infinity and two partial Cauchy surfaces⁵. In this way, the whole right-hand side integral vanishes: in fact, at the horizon $n^\mu = \xi^\mu$ and we supposed $\xi_\mu \phi_{;\mu} = 0$ for stationarity; at infinity, because of asymptotic flatness, $\phi_{;\mu} = 0$; the contributions of the two partial Cauchy surfaces cancel each other, as they can be generated by mapping one in another by an isometry [31]. Hence the left-hand side integral of Eq. 3.11 must be zero as well. With our metric signature, the term $\phi_{;\mu}^2 = \phi(r)_{;r}^2$ is positive in the BH exterior, therefore if

$$\mathcal{F}''(\phi) \mathcal{G} < 0 \quad (3.12)$$

the whole integrand on the left-hand side of Eq. 3.11 is sign-definite and must vanish at every point in \mathcal{V} . Moreover, in order to do that the two terms must be null simultaneously and this can be obtained only if $\phi = \phi_0$, where ϕ_0 is the constant value of the scalar field where the coupling function \mathcal{F} vanishes, as it has been called in Sec. 3.1.1.

So a theory that satisfies both conditions Eq. 3.9 and Eq. 3.12 admits a no-hair theorem

⁴A time-like vector A^μ is a vector with negative norm $A^\mu A_\mu < 0$, considering the mostly-plus metric signature of the riemannian spacetime; space-like vectors instead have positive norm; light-like ones (null vectors) have norm equal to zero.

⁵These are surfaces that divide the spacetime in two regions, one containing future events the other past ones. A partial Cauchy surface is a hypersurface on which no two points are connected by a causal curve (time-like or null).

(within the selected hypothesis), whose proof can be considered the one just written. The quantity in Eq. 3.12 can be seen as an effective mass for the perturbations of the scalar field. Indeed, if Eq. 3.3 is linearized around ϕ_0 we get the common wave equation

$$[\square + \mathcal{F}''(\phi_0)\mathcal{G}]\delta\phi = [\square - m_{eff}^2]\delta\phi = 0. \quad (3.13)$$

Thus a theory where this effective mass $m_{eff} = -\mathcal{F}''(\phi_0)\mathcal{G}$ is negative does not satisfy the conditions for the no-hair theorem, therefore it can circumvent it, triggering a *tachyonic instability* and eventually giving birth to a nontrivial scalar "hairy BH".

3.2 Spontaneous Scalarization

We focus now on BH solutions of the field equations Eqs. 3.7-3.8. Thus we consider a spherical symmetric spacetime, whose metric can be written⁶ as in Eq. 2.21. By substituting the metric into the equations of motion, we can reduce the system of differential equations to just four of them [9]-[31]: three stemming from the generalized Einstein equation Eq. (3.7) for the components (t,t) , (r,r) , and (θ,θ) , while the fourth equation pertains to the scalar field (Eq. 3.8)

$$(t, t): \quad B \left\{ (\phi'')^2 [16(B-1)\mathcal{F}_{,\phi\phi} - r^2] + 16(B-1)\phi''\mathcal{F}_{,\phi} - 4 \right\} + \\ - 4B' [2(1-3B)\phi'\mathcal{F}_{,\phi} + r] + 4 = 0, \quad (3.14)$$

$$(r, r): \quad \frac{1}{4}A \left\{ B [4 - r^2(\phi'')^2] + r^2 - 4 \right\} + BA' [2(1-3B)\phi'\mathcal{F}_{,\phi} + r] = 0, \quad (3.15)$$

$$(\theta, \theta): \quad -rBA'' \left(r - 4B\phi'\mathcal{F}_{,\phi} \right) + 4rB^2A'\phi''\mathcal{F}_{,\phi} - \frac{1}{2}r^2AB\phi'^2 \\ + \frac{1}{2A} \left[rBA'^2 \left(r - 4B\phi'\mathcal{F}_{,\phi} \right) \right] + A' \left\{ rB [4B\phi'^2\mathcal{F}_{,\phi\phi} - 1] - \frac{1}{2}rB' \left(r - 12B\phi'\mathcal{F}_{,\phi} \right) \right\} \\ - rAB' = 0 \quad (3.16)$$

$$(\phi): \quad AB\phi'' + \frac{1}{2}\phi' \left[BA' + A \left(\frac{4B}{r} + B' \right) \right] + \frac{4}{r^2} [(B-1)BA''\mathcal{F}_{,\phi}] + \\ - \frac{1}{2r^2A} \left\{ 4A' [(B-1)BA' + A(1-3B)B'] \mathcal{F}_{,\phi} \right\} = 0. \quad (3.17)$$

We wrote the derivatives of the coupling function with respect to its argument ϕ as $\mathcal{F}'(\phi) \equiv \mathcal{F}_{,\phi}$ and so for the next orders. The potential $V(\phi) = 0$ has already been set to 0. The prime indicates derivatives with respect to the radial coordinate r .

⁶We use classical radial coordinates (t, r, θ, φ) as previously done for BHs in GR in Sec. 2.1.2

As we can see here, but also from the generic form Eqs. 3.7-3.8, the equations do not depend on the coupling function itself but just on its derivatives.

Now, we note that the kinetic part of the action is *shift symmetric*, i.e. it does not change under transformations like $\phi \rightarrow \phi + c$. If the coupling function satisfies condition Eq. 3.9, it can be expanded around ϕ_0 as $\mathcal{F}(\phi) = \mathcal{F}(\phi_0) + \frac{1}{2}\mathcal{F}_{,\phi\phi}(\phi_0)(\phi - \phi_0)^2 + \dots$. So, thanks to the divergence-freedom of \mathcal{G} , the first term does not contribute to the equation of motion. By redefining $\phi \rightarrow \phi - \phi_0$, we can simplify the quadratic expansion of any coupling function to the form

$$\mathcal{F}(\phi) = \frac{\eta}{8}\phi^2, \quad (3.18)$$

of the so-called **quadratic-scalar-Gauss-Bonnet** (qsGB) gravity. This represents then the simplest kind of coupling satisfying Eq. 3.9, and studying qsGB can permit to learn much about most of the theories that fulfill that condition.

We can summarize here the conditions that the coupling function must satisfy for spontaneous scalarization to be possible

1. $\mathcal{F}_{,\phi}(\phi_0) = 0 \rightarrow$ for the existence of GR solutions;
2. $\mathcal{F}_{,\phi\phi}\mathcal{G} > 0 \rightarrow$ for the onset of a scalarized solution.

QsGB satisfies both requests with $\eta > 0$ and $\phi_0 = 0$.

Moreover the qsGB coupling function is symmetric under "parity" transformations of the field ($\phi \rightarrow -\phi$). This is important because, in a general EFT approach, assuming a fundamental parity symmetry (or \mathbb{Z}_2 -symmetry) would prevent the term $\phi\mathcal{G}$ from appearing in the action([31]). This kind of coupling, indeed, violates condition 1, yielding only scalarized BH solutions [32], excluding GR ones.

The system of differential equations above Eqs. 3.14-3.17 can be reduced to 3 coupled ordinary differential equations for A, B and ϕ . If we write $A = \exp(\Gamma)$ and $B = \exp(-\Lambda)$ it is also possible to solve analytically for the metric function Λ in terms of Γ and ϕ , and we would only need to integrate 2 second order differential equation [31]. Actually the equation for Λ only involves its derivatives, so it reduces to a first order differential equation [14]. However, for our study, even if the numerical implementation is less efficient, we will solve directly the 3 ODEs for A, B and ϕ , because it will simplify the stability analysis later.

3.2.1 Boundary and regularity conditions

We must impose asymptotic flatness at infinity and regularity at the BH horizon $r \rightarrow r_h$ ⁷.

Boundary at infinity Asymptotic flatness requires the metric to be Minkowski-like when $r \rightarrow \infty$ ⁸ and the scalar field to be vanishing

$$A|_{r \rightarrow \infty} \rightarrow 1, \quad B|_{r \rightarrow \infty} \rightarrow 1, \quad \phi|_{r \rightarrow \infty} \rightarrow 0. \quad (3.19)$$

Up to second order in powers of $1/r$ we get:

⁷We will use from now on r_h for event horizon's radius, to distinguish from R_s used for Schwarzschild's in GR.

⁸Minkowski's metric is $ds^2 = -dt^2 + dr^2 + r^2 d\Omega^2$ in spherical coordinate.

- $A(r) = 1 - \frac{2M}{r} + O((1/r)^3)$
- $B(r) = 1 - \frac{2M}{r} + O((1/r)^3)$
- $\phi(r) = \phi_{inf} + \frac{Q}{r} + \frac{MQ}{r^2} + O((1/r)^3)$.

with $\phi_{inf} = 0$. Here we have introduced as integration constants the Mass of the black hole M^9 and its **scalar charge** Q . This is the charge associated to BH solutions that manifests non-trivial scalar field profile. Despite its name, it is not a Noether charge, as it is not associated to a symmetry of the action and it is not dynamically conserved. It is only defined as an integration constant.

Boundary at the event horizon On the other side, towards the event horizon (EH) the metric should manifest a singularity in the coordinate system that we chose (the tt component goes to zero while the rr one diverges as in Schwarzschild solution, in Chap. 2). Hence

$$A|_{r \rightarrow r_h} \rightarrow 0, \quad B|_{r \rightarrow r_h} \rightarrow 0. \quad (3.20)$$

To find the condition towards the EH for the scalar field, we need to expand the equations around r_h . Truncating at zeroth order into powers of $(r - r_h)$ we can solve analytically¹⁰ for the coefficient of the first term of the expansion of ϕ and we get

$$\phi'(r)|_{r \rightarrow r_h} = \left[\frac{r_h}{4\mathcal{F}_{,\phi}} \left(-1 \pm \sqrt{1 - \frac{96\mathcal{F}_{,\phi}^2}{r_h^4}} \right) \right]_{r \rightarrow r_h}. \quad (3.21)$$

The solution we are interested in is the one with + sign, because when $\phi = 0$, meaning that $\mathcal{F}'(\phi = 0) = 0$ as it satisfies condition Eq. 1 in Sec. 3.2, we want to retrieve GR solution, where $\phi' = 0$ as well([21]). Moreover, to manifest regularity at the horizon ([14],[31]) we need to impose the positiveness of the argument of the square root in Eq. 3.21. Thus, we obtain the condition

$$r_h^4 > 96 \left(\mathcal{F}_{,\phi}(\phi_h) \right)^2. \quad (3.22)$$

where ϕ_h is the value of the scalar field at the EH.

Notably, if \mathcal{F} satisfies Eq. 3.9, for GR solutions, when $\phi = \phi_0$, condition 3.22 in Sec. 3.2 is automatically fulfilled. Conversely, for scalarized solutions it has to be verified.

In the end, we can write the boundary conditions at the EH as

- $A(r) = (r - r_h) + O((r - r_h)^2)$
- $B(r) = (r - r_h) + O((r - r_h)^2)$
- $\phi(r) = \phi_h + \phi'(r)(r - r_h) + O((r - r_h)^2)$
- $\phi'(r) = \frac{r_h}{4\mathcal{F}_{,\phi}(\phi_h)} \left[-1 \pm \left(1 - \frac{96(\mathcal{F}_{,\phi}(\phi_h))^2}{r_h^4} \right)^{\frac{1}{2}} \right] + O((r - r_h)^2)$.

⁹The factor 2 is present in the expansion because we want solutions to be asymptotically like GR metric, i.e. the two metric functions A and B must have the same trend as in Schwarzschild BHs (Eq. 2.22).

¹⁰It is a classical second degree equation.

What is a scalarized solution? We will refer with *scalarized BH* to every solution of sGB gravity with a non-trivial scalar field profile that vanishes towards infinity ($\phi_{inf} = 0$).

3.2.2 Numerical implementation

All the numerical analysis has been done with WOLFRAM MATHEMATICA.

For the beginning we chose quadratic coupling function Eq. 3.18, since qsGB has already been deeply studied (see [9],[31]). In this way, our algorithms can be checked with existing literature results so that they can be later used for other couplings.

From this point onward, all distances and other quantities with the same dimension of a length, within the geometrical units used, will be expressed as pure numbers, implying they are in units of r_h , the horizon radius. The latter will be set to 1 for the whole study, for simplicity.

Step 1: integration of the equations of motion Firstly, we integrate the equations of motion imposing only the boundary conditions at the event horizon. To avoid divergences and to prevent the boundary conditions to be ill-defined, the integration is set to begin from $r_h + \varepsilon$, with ε the horizon proximity parameter. Before computing the numerical values of the mass and the scalar charge, we need to normalize the integrated metric function A , since it is defined up to an integration constant. Therefore, the function $A(r)$ returned by the integration is divided by the value that it assumes at infinity. In this way, at first order, $A(r)|_{r \rightarrow \infty} = 1$, as requested by asymptotic flatness in Eq. 3.19.

Now we impose the boundary conditions (BCs) at infinity and solve them numerically for M, Q and ϕ_{inf} . The infinite value is actually finite, obviously, but sufficiently large such that quantities like ϕ_{inf} , M and Q are not affected by its variations.

In Fig. 3.1 we show the comparison of the metric function $A(r)$ for a Schwarzschild BH in GR and a scalarized BH in qsGB gravity.

Step 2: shooting method In order to integrate the equations of motions we need to provide a value for the scalar field at the event horizon ϕ_h , so that the boundary conditions are well defined. We perform a shooting method, trying different values of ϕ_h and checking the resulting value of ϕ_{inf} returned by the integration. We select as a scalarized solution the one that manifests $\phi_{inf} \sim 0$, as requested by BCs at infinity Eq. 3.19.

The procedure for the search of scalarized solutions is the one just described, however we should specify how to select the possible shooting values for ϕ_h . We will refer to those as ϕ_{h_0} .

Let us consider an explicit coupling function, the quadratic one $\mathcal{F}(\phi) = \frac{\eta}{8}\phi^2$. Note that the coupling constant η has the dimension of a mass² = length² ($\equiv L^2$), since GB term's dimension is L^{-4} and the scalar field is dimensionless [31].

The regularity condition Eq. 3.22 restricts the range of η for which scalarized solutions are possible. We can compute analytically the value of $\phi_{h_{max}}$ for which the square root in Eq. 3.21 vanishes. This represents the maximum value of ϕ_h for which the scalarized solution is still regular at the EH. Hence, it is also the maximum value of ϕ_{h_0} that we can use in the shooting method. In Fig. 3.2 we show the possible values of ϕ_{h_0} for $\eta = 0.7$ for quadratic

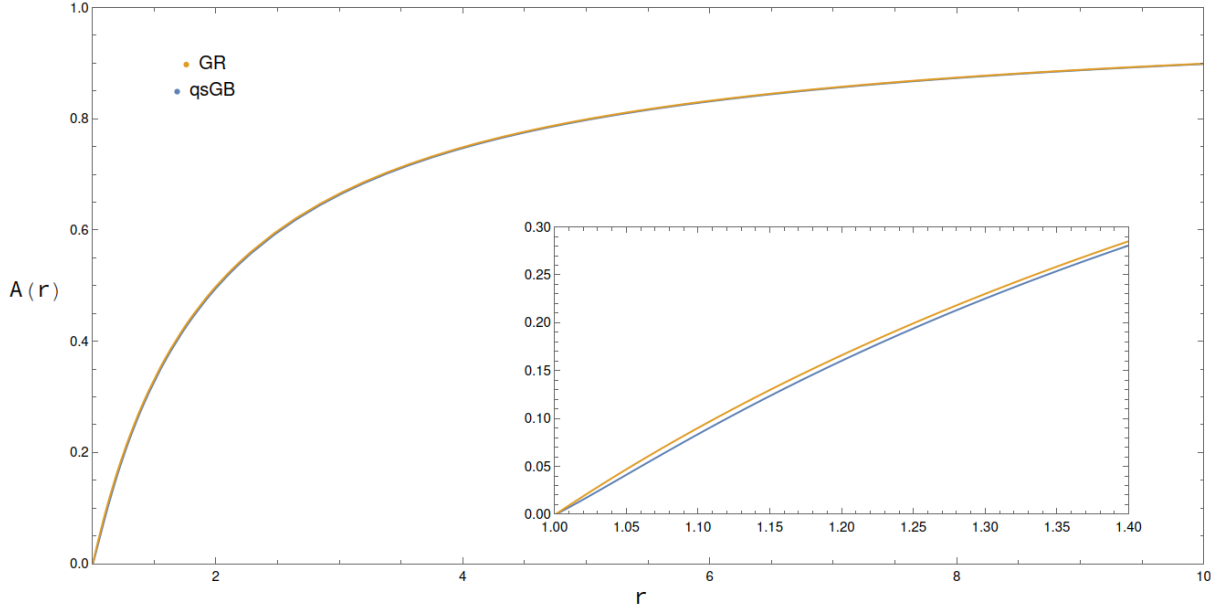


Figure 3.1: Comparison of the profile of the tt component of the metric tensor between the Schwarzschild solutions of GR (where $A(r) = 1 - 1/r$) and a scalarized black hole solution within qsGB gravity. The value of the coupling constant is $\eta = 0.7$ and the scalar field at the EH is $\phi_{h_0} = 0.50925$, at which scalarized solution arises.

coupling. Indeed, the function

$$f_{reg} = r_h^4 - 96 \left(\mathcal{F}_{,\phi}(\phi_h) \right)^2 \quad (3.23)$$

is always positive for $\phi_{h_0} \in [-\phi_{h_{max}}, \phi_{h_{max}}]$, consequently the regularity condition Eq. 3.22 in that region is satisfied. As shown in Fig. 3.2, however, we consider only positive values of the scalar field ϕ_{h_0} , since the coupling function is \mathbb{Z}_2 -symmetric. Hence, we will shoot different values of ϕ_{h_0} from 0 to $\phi_{h_{max}}$, spacing them by a small, adjustable increment.

In order to understand when we can have scalarized solutions, we can plot the value of ϕ_{inf} as a function of ϕ_{h_0} for different values of the coupling constant η . This is illustrated in Fig. 3.3.

As we can see in Fig. 3.3, every curve starts from the origin of the plot. This is expected, since the point $(\phi_h, \phi_{inf}) = (0, 0)$ corresponds to the GR solution, when the scalar field is identically zero. This solution is always present. Nevertheless, for scalarized solutions we are interested in a non-trivial configuration of the scalar field, meaning that the profile of ϕ_{inf} as a function of ϕ_{h_0} , for a given value of η , must admit a second zero. Indeed, as specified above, a solution can be considered scalarized only if it has vanishing value of the scalar field at infinity, alongside with a non-trivial profile of the latter. This happens only for certain values of the coupling constant η , as we can understand from Fig. 3.3, where neither $\eta = 0.69$, neither $\eta = 0.73$ admit a second zero point. Therefore, the range of coupling values for which scalarized solutions arise, for quadratic coupling function, is between 0.69 and 0.73. We stress the fact that the ending points of each curve in Fig. 3.3 correspond to the value of ϕ_{inf} returned by the integration computed with $\phi_h = \phi_{h_{max}}$. Curves are truncated when the resulting scalar field is not regular at the horizon.

We only need to refine this range now, by shooting increasing values of the coupling constant

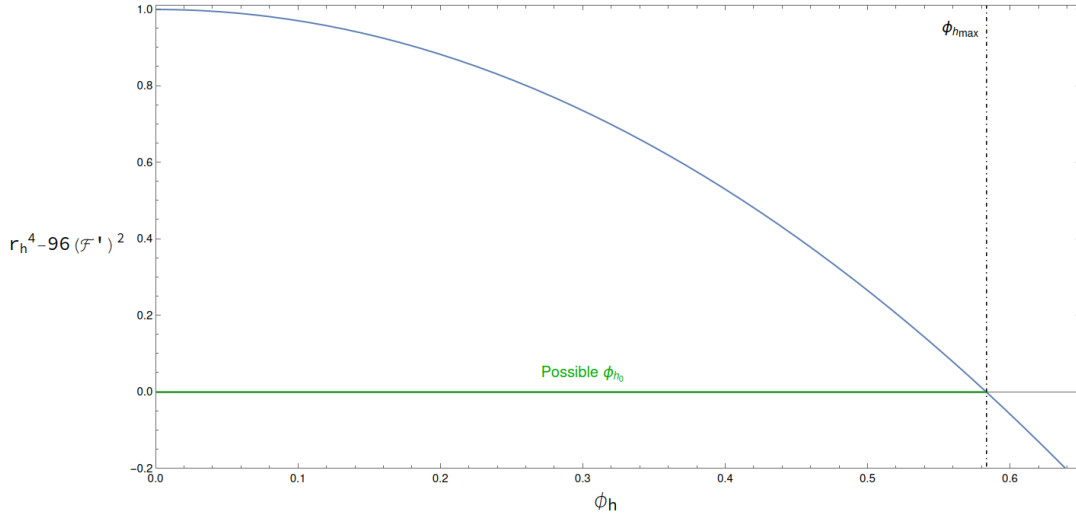


Figure 3.2: Plot of the regularity function $f_{reg} = r_h^4 - 96 \left(\mathcal{F}_{,\phi}(\phi_h) \right)^2$ for $\eta = 0.7$ in qsGB. The maximum value of ϕ_{h_0} for which the scalarized solution is regular at the EH is $\phi_{h_{max}} = 0.583212$. The green line represents all the possible values of ϕ_{h_0} that can be used in the shooting method for finding a scalarized solutions.

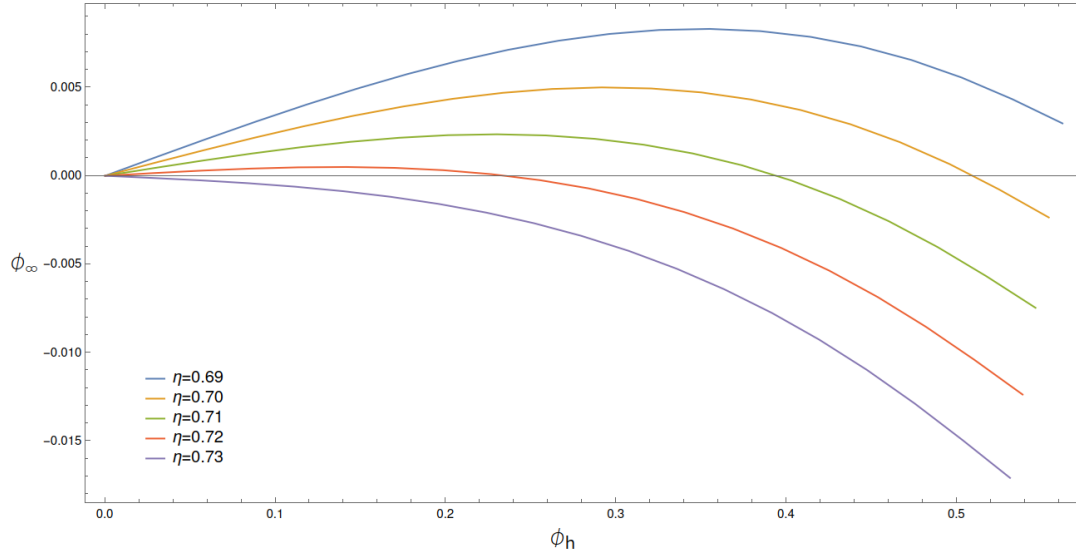


Figure 3.3: Profile of the scalar field value towards infinity ϕ_∞ as a function of the value that it assumes at the event horizon ϕ_h . Varying η from 0.69 to 0.73 we can appreciate how the corresponding curves admit a second zero point alongside with the one in the origin just for certain η . The ending points are not a truncation of the display, but they coincide with the maximum value of the scalar field at the EH $\phi_{h_{max}}$ permitted by the regularity condition Eq. 3.22, which changes for each coupling.

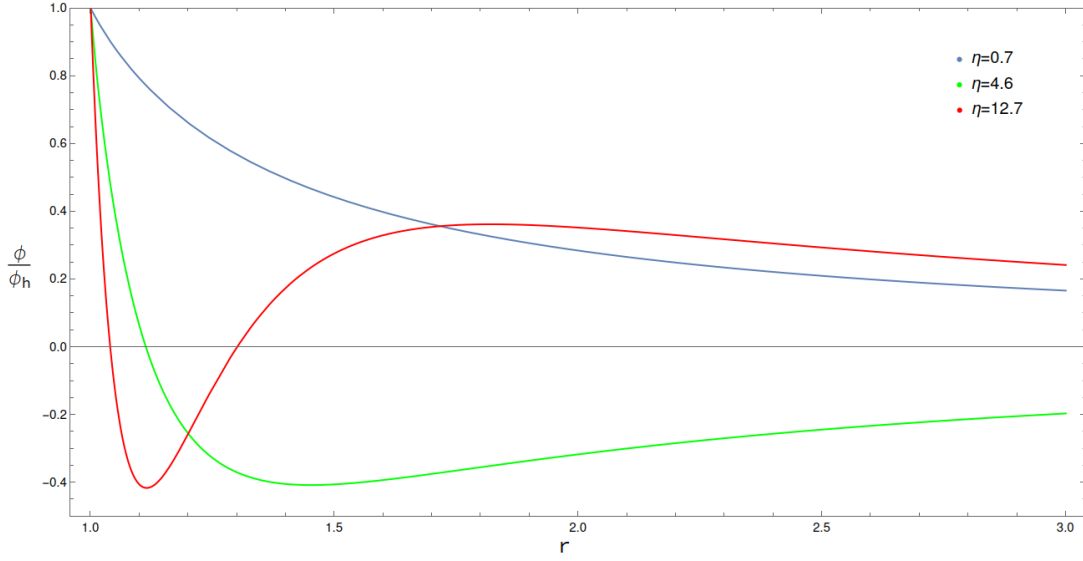


Figure 3.4: Trend of the scalar field, normalized as $\frac{\phi}{\phi_h}$, as a function of the radial distance r from the center of the BH, for different values of the coupling constant η . We can see how the scalar field has more zeroes (nodes) for growing values of η .

and applying the Theorem of zeros for the corresponding functions $\phi_{inf}(\phi_{h_0})$.

We notice that increasing the values of η , we are able to find more ranges where scalarized solutions are allowed. The first three ranges of normalized coupling constant η/M^2 of scalarized solutions that have been computed are

$$\eta/M^2 \in [2.529, 2.894] \quad \eta/M^2 \in [17.89, 19.50] \quad \eta/M^2 \in [47.90, 50.90] \quad (3.24)$$

Plotting the trend of the scalar field as a function of distance r for different values of the coupling constant taken from each range of scalarized solutions that we found in Eq. 3.24 we get the plot in Fig. 3.4.

In Fig. 3.4 we can note how, for growing value of the coupling constant η , the scalar field presents increasing number of zeroes. We will refer to this zeroes as the *nodes* of the solution. Thus it is possible to classify different solutions based on the number of nodes they have. *0-node* solution will be called "*Fundamental*". In Fig. 3.4 a rescaling has been carried out in order to appreciate the nodes, plotting $\frac{\phi}{\phi_h}$, but actually the physical representation is the one in Fig. 3.5, where we can see how the fundamental solution manifests the most significant deviation from GR.

Additionally, we can visualize the existence regions of scalarized BHs in (η, M) plane, as shown in Fig. 3.6. Actually, it is also possible to find scalarized regions with 3 and 4 nodes, with value of $\eta/r_h^2 \simeq 23.7, 246.9$.

Displaying the ratio between the scalar charge Q and the mass M of the black hole as a function of the normalized coupling constant η/M^2 we get the plot in Fig. 3.7.

In Fig. 3.7 the ranges of the coupling constant that yield scalarized solutions are evident, corresponding to the branches that deviate from zero. From left to right they display solutions with growing number of nodes, from the fundamental to the 2-nodes branch. As stated above, the fundamental branch is the one whose related scalar charge is the largest, while the width of the ranges grows as the number of nodes increases.

The first three branches of scalarized solutions are reported in Fig. 3.8, where the normalized charge

$$\hat{Q} = Q/\eta^2 \quad (3.25)$$

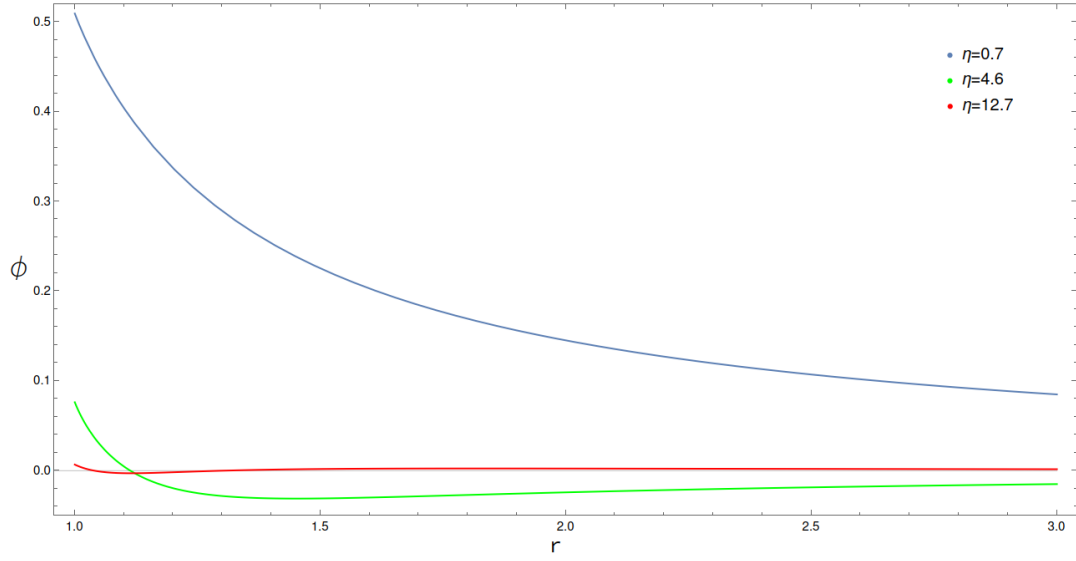


Figure 3.5: Trend of the scalar field ϕ as a function of r for different values of the coupling constant η . These are the same solutions as in Fig. 3.4, but here the scalar field is not normalized, in order to appreciate the physical values.

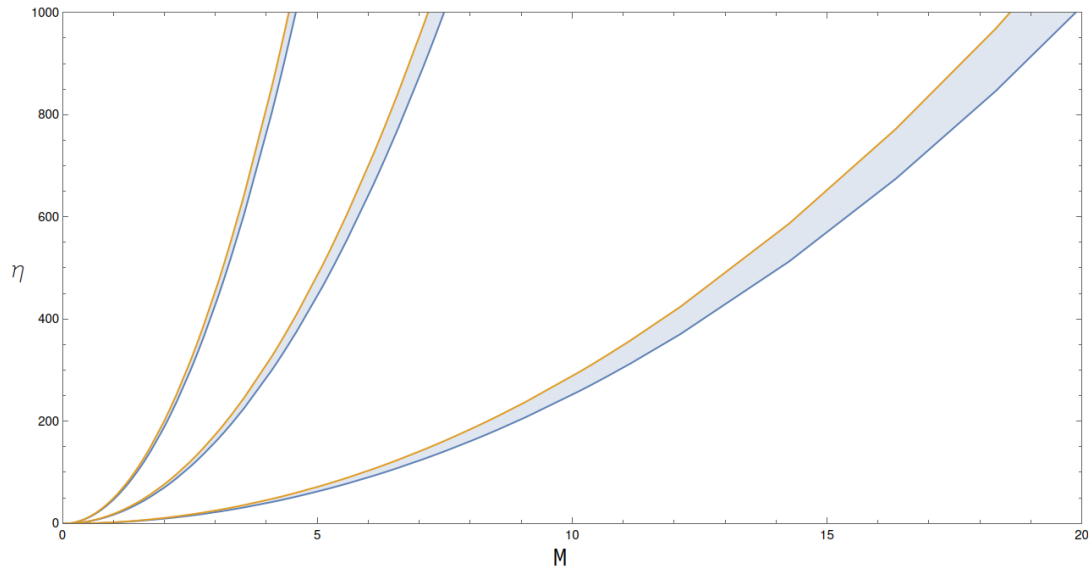


Figure 3.6: Representation of the coupling constant η as a function of the BH mass M for the first three branches of scalarized solutions. The yellow curves correspond to the lower end of the ranges Eq. 3.24, while blue curves are related to the upper end of the same ranges. The gray areas indicate the regions where scalarized BHs arise.

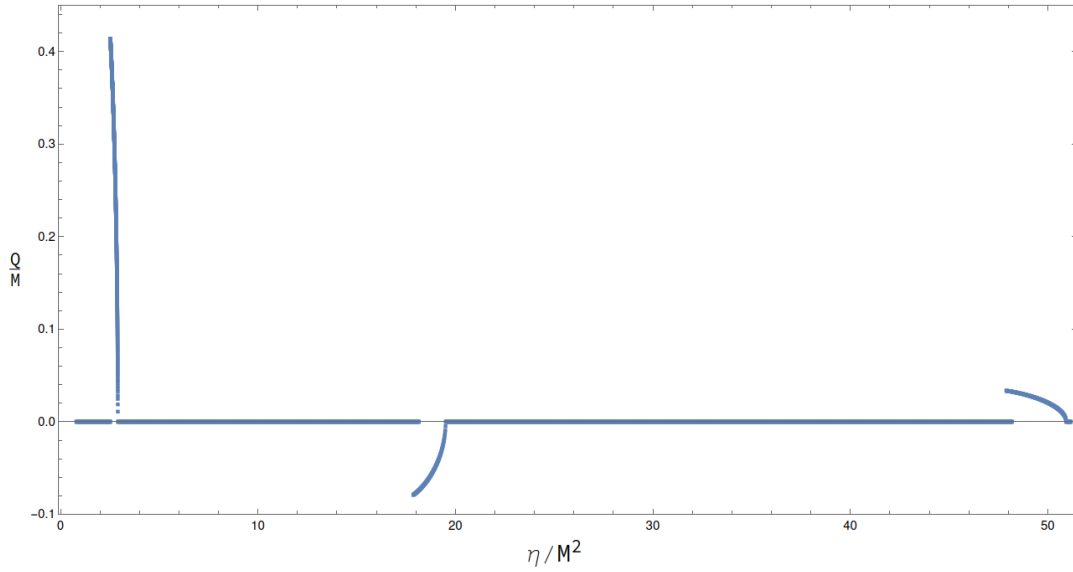


Figure 3.7: Ratio between the scalar charge Q and the mass M of the BH solutions as a function of the normalized coupling constant η/M^2 . The deviations from the abscissa, which stands for the Schwarzschild case that is chargeless, are the fundamental branch, the 1-node and the 2-nodes branches, from left to right.

is depicted as a function of the normalized mass

$$\hat{M} = M/\eta^2. \quad (3.26)$$

Furthermore, the symmetric counterpart associated with negative charge in the branches is also illustrated.

In the end we can show the deviation from GR Schwarzschild mass $M = r_h/2$ of the scalarized solutions in Fig. 3.9. The ratio between the horizon radius and the mass of the BH is plotted as a function of the dimensionless coupling constant η . The fundamental branch is the one that deviates the most from the Schwarzschild case. In every branch we notice how the scalarized black holes are more compact than the Schwarzschild ones, as for fixed horizon radius they enclose larger mass.

All this results can be checked with the literature studies [31] and [14].

3.3 Stability analysis

For the moment, we have established the existence of stationary scalarized black holes within qsGB gravity. However, the stability of these solutions is still undetermined. This feature needs to be addressed, because unstable solutions under perturbations are not viable BHs solutions, as in that case the minimum disturbance can grow in time catastrophically, leading to different configurations from the initial one.

In this thesis we will take into account small radial perturbations, as studied in [30], [9], [22] for specific choices of the coupling function, extending these works to more general couplings. In this chapter we still report stability analysis that have already been performed in current literature, whose results are obtained again and extended with our algorithms.

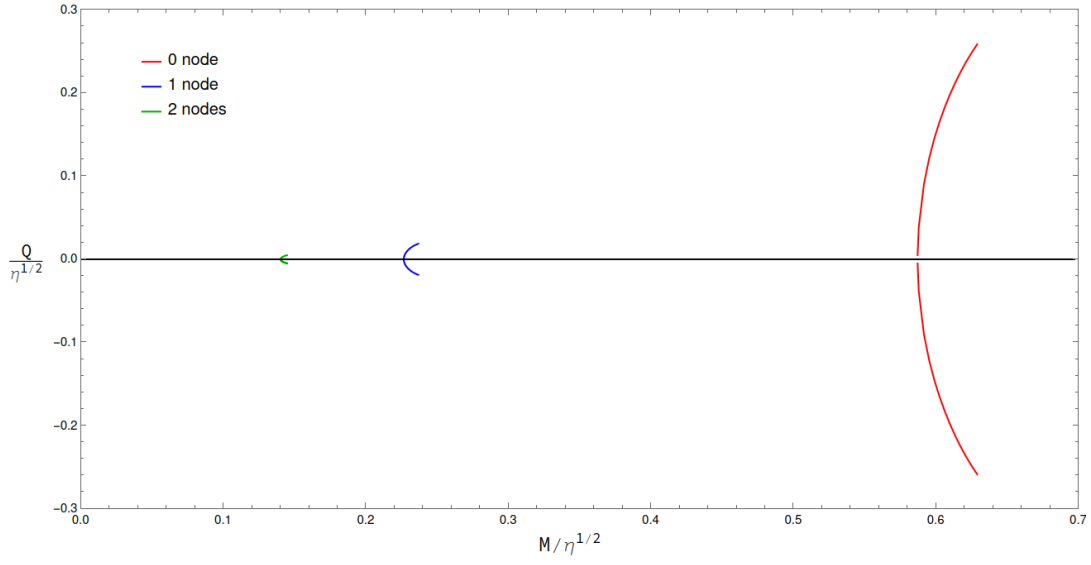


Figure 3.8: Normalized scalar charge $\hat{Q} = Q/\eta^{1/2}$ as a function of the normalized mass $\hat{M} = M/\eta^{1/2}$ of the BH. The black horizontal line is related to the chargeless Schwarzschild solution ([9]).

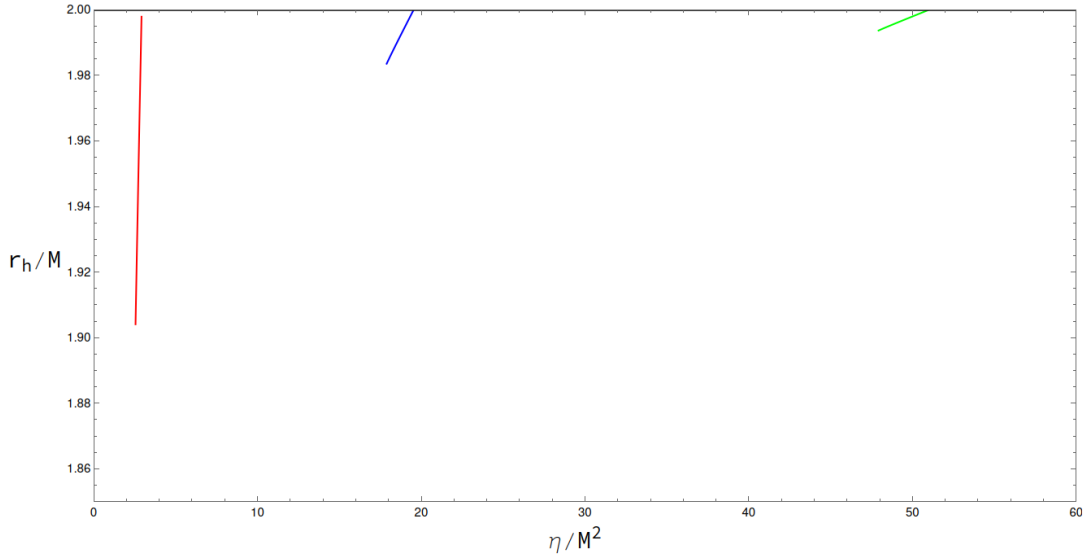


Figure 3.9: Ratio between horizon radius r_h and the BH mass M as a function of the dimensionless quantity η/M^2 . In red the fundamental branch, in blue the 1-node, in green the 2-nodes branches. In black, constantly at ratio equal to 2, the Schwarzschild case is depicted.

In GR radial perturbations describe non-radiative fields. Indeed, the perturbation equation can be solved analytically and correspond to a change of mass of the Schwarzschild BH solution, as expected from Birkhoff theorem. Birkhoff theorem in GR states that any spherically symmetric solution of Einstein field equations in vacuum (without matter) is necessarily static and asymptotically flat. Thus, any spherical distribution of matter (like a non-rotating star) yields a gravitational field in its exterior which corresponds to the Schwarzschild solution. However, for modified theories of gravity, radial perturbations can lead to significant consequences for the stability of the spacetime, since the Birkhoff theorem does not apply.

Perturbed equation

In the previous Sec. 3.2 it has been shown how to integrate the unperturbed sGB equations. From that integration we obtain the metric functions $A(r)$ and $B(r)$ and the scalar field $\phi(r)$ profiles. These will constitute the *background* configuration, that will be perturbed in order to analyze how scalarized BHs behave.

Once the background solutions are given, we perform a perturbation of the metric functions and of the scalar field, as in [30], [9]

$$\phi = \phi_0 + \varepsilon \frac{\varphi_1(t, r)}{r} \quad (3.27)$$

$$ds^2 = -[A(r) + \varepsilon F_t(t, r)]dt^2 + [B(r)^{-1} + \varepsilon F_r(t, r)]dr^2 + r^2 d\Omega^2 \quad (3.28)$$

where A , B and ϕ_0 are the background solutions. F_t and F_r are the first order perturbations of the tt and rr components of the metric tensor, respectively; φ_1 serves as the equivalent for the scalar field. All these perturbation functions depend both on time and radial coordinates. To get the linearized field equations for radial perturbations we need to expand the unperturbed equations of motion up to first order in ε , inserting the ansatz Eq. 3.27 and Eq. 3.28. We derive five equations, the details of which are omitted here due to their complexity and limited relevance. These equations can be manipulated [9] to yield a single second-order partial differential equation for the radial perturbation of the scalar field $\varphi_1(t, r)$. The outcome is the following equation

$$g^2(r) \frac{\partial^2 \varphi_1(t, r)}{\partial t^2} - \frac{\partial^2 \varphi_1(t, r)}{\partial r^2} + k(r) \frac{\partial \varphi_1(t, r)}{\partial r} + U(r) \varphi_1(t, r) = 0 \quad (3.29)$$

where the functions $U(r)$, $g(r)$ and $k(r)$ depend only on the background metric functions and scalar field. Their expressions are written in Appendix A.

The same approach can be used for the Schwarzschild solution case, where we know exactly the metric functions and the scalar field profiles

$$A(r) = B(r) = 1 - \frac{r_s}{r} \quad (3.30)$$

$$\phi_0(r) = 0 \quad (3.31)$$

$$\mathcal{F}(\phi_0) = \mathcal{F}'(\phi_0) = 0. \quad (3.32)$$

The trivial profile of ϕ_0 and Eq. 3.32 for the coupling function comes from the condition Eq. 3.9 and from the choice made for \mathcal{F} to be vanishing when evaluated at $\phi = 0$, which is usually

made in literature (see for example the case of qsGB).

Substituting the expressions above, we obtain the following equation for Schwarzschild background

$$\begin{aligned} & \frac{1}{2r^4} \left[\varphi_1(t, r) \left(-2r^6 + 2r^7 + 24r^3 (\mathcal{F}'')(0) - 24r^4 (\mathcal{F}''')(0) \right) + \right. \\ & \left. - 2r \left((-1+r)r^6 \frac{\partial \varphi_1}{\partial r}(t, r) + r^7 \left((-1+r)^2 \frac{\partial^2 \varphi_1}{\partial r^2}(t, r) - r^2 \frac{\partial^2 \varphi_1}{\partial t^2}(t, r) \right) \right) \right] = 0 \end{aligned} \quad (3.33)$$

QNM approach

A powerful way to study the behavior of physical systems near equilibrium is to analyze their *normal modes*, i.e. the characteristic modes of oscillation in the absence of external forces [16]. These modes can be performed by BHs in different scenarios, e.g. after the coalescence of binary compact systems. In this case, though, the oscillations are not eternal, since the BH loses energy emitting gravitational waves until it becomes stationary.

Therefore, the damped oscillations can be searched through complex mode eigenfrequencies

$$\omega = \omega_R + i\omega_I. \quad (3.34)$$

Indeed, any quantity with a time dependence $\sim e^{-i\omega t}$ with $\omega_I < 0$ describes a damped oscillation

$$e^{-i\omega t} = e^{-i\omega_R t} e^{\omega_I t} \quad (3.35)$$

where ω is the pulsation, which is related to the oscillation frequency of the mode through its real component as $\nu = \omega_R/2\pi$ and to the *damping time* through the imaginary part as

$$\tau = -\frac{1}{\omega_I}. \quad (3.36)$$

The free oscillation modes of a perturbed BH are called **quasi-normal modes (QNM)**, where *quasi* indicates that the eigenfrequencies are complex¹¹. Note that, whether the condition $\omega_I < 0$ is not fulfilled, the oscillations grow exponentially with time, with *growth time* $\tau = 1/\omega_I$, acknowledging that the black hole is not stable.

Radial perturbations can be caused in many processes. For instance, when an external mass falls beyond the event horizon of the BH, or after the gravitational collapse of a sufficiently massive star such that its remnant is indeed a BH. After these events the BH is in general non-stationary, reaching then a quasi-stationary configuration where it oscillates with its characteristic frequencies. We stress the fact that spherically symmetric objects oscillating radially do not emit gravitational waves (GW) in standard GR, since their quadrupole moment remains null (see Appendix B). Radial perturbations can be associated to mass variations in that framework and do not lead to radiation [39]. However, in modified theories of gravity, such as sGB, radial perturbations can be radiative, as we will show in the following.

Our aim is to determine whether the scalarized solutions (and the GR-like ones either) admit positive imaginary part of the eigenfrequencies ω , so that we can claim that those solutions are not viable, due to their instability.

¹¹The normal modes eigenfrequencies of a non-dissipative oscillating system are real frequencies.

3.3.1 Schrödinger-like perturbed equation and boundary conditions

We operate a harmonic-time decomposition of the scalar field perturbation

$$\varphi_1(t, r) = \varphi(r) e^{-i\omega t}. \quad (3.37)$$

Substituting it in Eq. 3.29 we get

$$-\omega^2 g^2(r) - \frac{\partial^2 \varphi(r)}{\partial r^2} + k(r) \frac{\partial \varphi(r)}{\partial r} + U(r) \varphi(r) = 0 \quad (3.38)$$

where the coefficient $e^{-i\omega t}$ has already been simplified. From this point forward, as each function relies exclusively on the radial coordinate, the variable of dependence will be omitted¹².

We rewrite the above expression naming

$$\varphi(r) = f(r) Z(r) \quad (3.39)$$

so we get

$$\left(-\omega^2 g^2 + U\right) f Z - f'' Z - 2f' Z' - f Z'' + k f' Z + k f Z' = 0 \quad (3.40)$$

Dividing by $-f$ and collecting terms of the same order of derivative in Z we obtain

$$Z'' + Z' \left(2 \frac{f'}{f} - k\right) - Z \left(U - \omega^2 g^2 - \frac{f''}{f} + k \frac{f'}{f}\right) = 0. \quad (3.41)$$

We should now define the *tortoise coordinate*¹³ r_* as

$$\frac{dr_*}{dr} = g. \quad (3.42)$$

In this way, changing variables from r to r_* , the derivatives with respect to r become

$$\begin{aligned} \bullet \quad \frac{\partial}{\partial r} &\rightarrow \frac{\partial r_*}{\partial r} \frac{\partial}{\partial r_*} = \tilde{g} \frac{\partial}{\partial r_*} \\ \bullet \quad \frac{\partial^2}{\partial r^2} &\rightarrow \frac{\partial r_*}{\partial r} \frac{\partial}{\partial r_*} \left[\frac{\partial r_*}{\partial r} \frac{\partial}{\partial r_*} \right] = \tilde{g} \frac{\partial}{\partial r_*} \left[\tilde{g} \frac{\partial}{\partial r_*} \right] = \tilde{g}^2 \frac{\partial^2}{\partial r_*^2} + \tilde{g} \tilde{g}' \frac{\partial}{\partial r_*} \end{aligned} \quad (3.43)$$

where with \tilde{g} is indicated the same g as in Eq. 3.42, but depending on the tortoise coordinate. In the following equations each quantity has to be intended as the same as its correspondent without tilde, but as a function of r_* .

Using derivatives in Eq. 3.43 and changing variables in favour of the tortoise coordinate Eq. 3.42, Eq. 3.41 becomes

$$\begin{aligned} g g' Z' + g^2 Z'' + g Z' \left[2g \frac{f'}{f} - k \right] - Z \left[V_{eff} - \omega^2 g^2 \right] &= 0 \\ Z'' + Z' \left[2 \frac{f'}{f} - \frac{k}{g} + \frac{g'}{g} \right] - Z \left[V_{eff} - \omega^2 \right] &= 0 \end{aligned} \quad (3.44)$$

¹²Prime will indicate derivatives with respect to r obviously.

¹³See Page 2.1.3 for details on tortoise coordinate for Schwarzschild solution in GR.

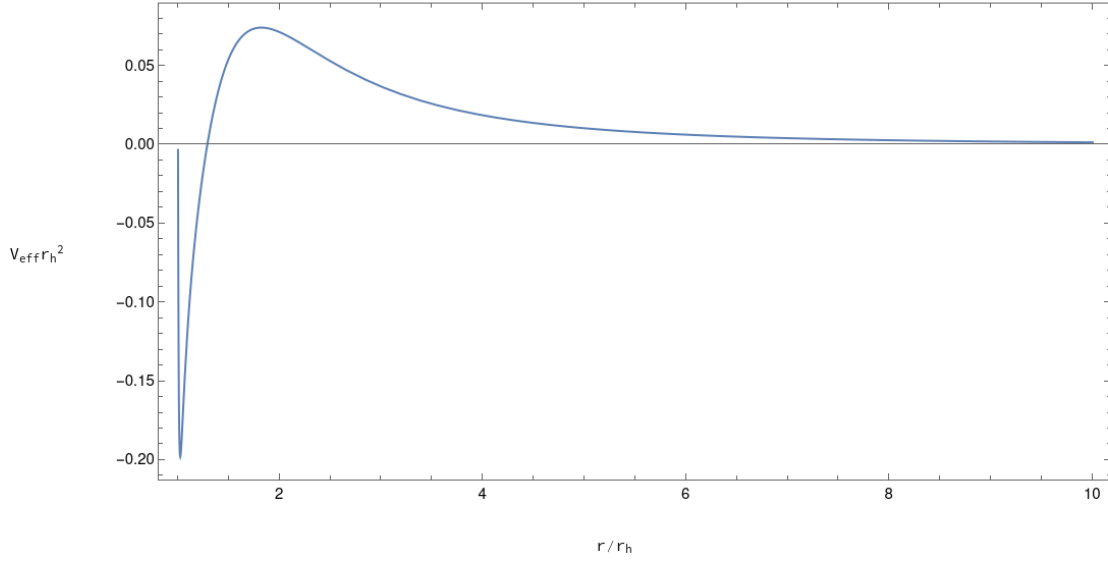


Figure 3.10: Effective potential V_{eff} as a function of the standard radial coordinate r , for qsGB gravity with $\eta = 0.6975$ and $\omega_I = 0.0945$.

The second equation has been obtained dividing by g^2 the first one. We have defined the effective potential V_{eff} as [9]

$$V_{eff} = \frac{\hat{V}_{eff}}{g^2} = \frac{1}{g^2} \left(U - \frac{f''}{f} + k \frac{f'}{f} \right). \quad (3.45)$$

Imposing that the coefficient of the first order derivative term in Eq. 3.44 vanishes [5], the function $f(r)$ must be solution of the equation

$$2 \frac{1}{g} \frac{f'}{f} - \frac{k}{g} + \frac{g'}{g^2} = 0 \quad (3.46)$$

$$2 \frac{f'(r)}{f(r)} = k(r) - \frac{g'(r)}{g(r)}.$$

In conclusion, Eq. 3.38 can be cast into a Schrödinger-like equation for the perturbation field Z in tortoise coordinate

$$\left[\frac{d^2}{dr_*^2} + (\omega^2 - V_{eff}) \right] Z = 0. \quad (3.47)$$

This form is useful as it permits to study the problem in a quantum mechanics approach, by imposing suitable boundary conditions.

The effective potential vanishes both at the event horizon and at infinity, i.e. when $r_* \rightarrow -\infty$ and $r_* \rightarrow \infty$ as we can see from the example in Fig. 3.10 realized for qsGB gravity for a coupling constant value included in the fundamental branch. Thus, the asymptotic behavior of the solution of Eq. 3.47 is simply that of a harmonic oscillator of pulsation ω , since Eq. 3.47 is reduced to the form

$$\left[\frac{d^2}{dr_*^2} + \omega^2 \right] Z \simeq 0. \quad (3.48)$$

Consequently, the general solution of the perturbed equation Eq. 3.47, when $r_* \rightarrow \pm\infty$, is a linear combination of two exponential functions

$$Z \simeq A_{in} e^{-i\omega r_*} + A_{out} e^{i\omega r_*} \quad (3.49)$$

and reintroducing time dependence, the complete solution is

$$Z e^{-i\omega t} \simeq A_{in} e^{-i\omega(r_*+t)} + A_{out} e^{i\omega(r_*-t)}. \quad (3.50)$$

The first term represents an *ingoing* wave with amplitude A_{in} , whereas the second represents an *outgoing* wave with amplitude A_{out} . We are interested in the free oscillations of the BH, so no external events should be taken into account: no wave is incoming from infinity and no wave can escape from the black hole. These two conditions result in fixing $A_{in} = 0$ when $r_* \rightarrow \infty$ and $A_{out} = 0$ as $r_* \rightarrow -\infty$.

To summarize, the asymptotic solution of the perturbed equation Eq. 3.47 is

$$Z e^{-i\omega t} \propto \begin{cases} e^{-i\omega(r_*+t)} & \text{as } r_* \rightarrow -\infty \\ e^{i\omega(r_*-t)} & \text{as } r_* \rightarrow \infty \end{cases} \quad (3.51)$$

Due to the fact that φ_1 is a scalar field, that the perturbed equation Eq. 3.29 has real coefficients and that the perturbations are only radial, it can be demonstrated that an unstable solution has pure imaginary frequency. It is possible to consider solutions with $\omega_r = 0$. Then, at fixed time, the solution in the asymptotic regions can be written as

$$Z \propto \begin{cases} e^{\omega_I r_*} & \text{as } r_* \rightarrow -\infty \\ e^{-\omega_I r_*} & \text{as } r_* \rightarrow \infty. \end{cases} \quad (3.52)$$

We consider the case of unstable modes, i.e. $\omega_I > 0$. Therefore, executing the limits $r_* \rightarrow \infty$ and $A_{out} = 0$ as $r_* \rightarrow -\infty$, we see that at both boundaries the solution goes to zero exponentially. These are the first boundary conditions that we should impose to integrate the perturbed equation in order to find unstable BH configurations.

Since Eq. 3.47 is a second order differential equation, we need to provide also conditions for the first derivative of Z , at both boundaries. Differentiating Eq. 3.52 with respect to r , we find

$$\frac{d}{dr} Z \propto \begin{cases} \omega_I \frac{dr_*}{dr} e^{\omega_I r_*} & = \omega_I g e^{\omega_I r_*} & \text{as } r_* \rightarrow -\infty \\ -\omega_I \frac{dr_*}{dr} e^{-\omega_I r_*} & = -\omega_I g e^{-\omega_I r_*} & \text{as } r_* \rightarrow \infty. \end{cases} \quad (3.53)$$

Note that the exponential term in both limits vanishes for positive ω_I , i.e. in the unstable case. However, the coefficient g is actually coincident with the inverse of the tt component of the metric, so, when approaching the horizon, it diverges. To see what is the result of the limit we can use Schwarzschild tortoise coordinate (with $r_h = 1$)

$$\lim_{r \rightarrow 1} (1 - 1/r)^{-1} e^{r + \ln|r-1|} \stackrel{H}{=} \lim_{r \rightarrow 1} r^2 (e^r (r-1) + e^r) = e \quad (3.54)$$

where the symbol $\stackrel{H}{=}$ means that we used de l'Hôpital theorem.

We conclude that the boundary conditions for the first derivatives of Z can be set to a

constant value.

Summing up, the boundary conditions for the perturbed equation are

$$\begin{cases} Z = 0 & \text{as } r_* \rightarrow \pm\infty \\ \frac{d}{dr}Z = c_{\pm}, c_{\pm} \in \mathbb{R} & \text{as } r_* \rightarrow \pm\infty \end{cases} \quad (3.55)$$

3.3.2 Sufficient condition for Bound states existence

As we have demonstrated in the above section, the perturbed equation can be cast into a Schrödinger-like form. This is useful not only to determine the proper boundary conditions for the direct integration of Eq. 3.47, but also to study the stability of the BH from a different perspective.

In fact, as stated by [35],[9],[5], the sign of the integral of the effective potential V_{eff} written in Eq. 3.45 with respect to the tortoise coordinate can be studied to determine if the black hole admits unstable modes. As suggested by [11], a sufficient condition for the existence of bound states in a one-dimensional quantum system, where the potential $V(x)$ vanishes rapidly at the extremes of the integration, is that the integral of the potential is negative

$$\int_{-\infty}^{+\infty} V dx < 0. \quad (3.56)$$

A brief demonstration is presented below. The time independent Schrödinger equation for a one-dimensional system is

$$-\frac{\hbar^2}{2m} \frac{d^2\psi}{dx^2} + V(x)\psi = E\psi \quad (3.57)$$

where E is the energy of the system.

For the beginning, let us consider the case of a potential well

$$V(x) = \begin{cases} -U_0 & \text{for } x \in [-a, a] \\ 0 & \text{otherwise} \end{cases} \quad (3.58)$$

with $a \in \mathbb{R}^+$ and $U_0 > 0$.

From variational principle we know that the energy of the ground state (GS) is always overestimated by the energy of a trial wave function ψ_0 . Thus if we compute the energy $\langle \psi_0 | H | \psi_0 \rangle = E_{trial}$ and we found a negative value, then $E_{GS} < E_{trial}$, assuring the presence of a bound state.

We can consider as trial function the eigenfunction of a δ -well potential

$$\psi_0(x) = \sqrt{\alpha} e^{-\alpha|x|} \quad (3.59)$$

where α is a constant. The energy of the trial function is

$$\begin{aligned}
\langle T \rangle &= \int_{-\infty}^{+\infty} \psi_0^* \left(-\frac{\hbar^2}{2m} \frac{d^2}{dx^2} \right) \psi_0 dx = \frac{\hbar^2 \alpha^2}{2m} \int_{-\infty}^{+\infty} e^{-2\alpha|x|} dx = \frac{\hbar^2 \alpha^2}{m} \int_0^{+\infty} e^{-2\alpha x} dx = \frac{\hbar^2 \alpha^2}{2m^2} \\
\langle V \rangle &= \int_{-\infty}^{+\infty} \psi_0^* V(x) \psi_0 dx = -U_0 \int_{-a}^a e^{-2\alpha|x|} dx = -U_0 \left(1 - e^{-\alpha a} \right) \\
E_{trial} &= \frac{\hbar^2 \alpha^2}{2m} - U_0 \left(1 - e^{-\alpha a} \right)
\end{aligned}$$

Hence, for sufficiently small α the energy of the trial function (E_{trial}) is negative, and so the energy of the ground state E_{GS} is negative as well.

Now we can generalize the procedure to a generic potential $V(x)$ such that its integral is negative

$$\int_{-\infty}^{+\infty} V(x) dx = c < 0 \quad (3.60)$$

and that goes to zero sufficiently rapidly towards both infinities.

Using the same trial function considered before, the energy obtained in the limit $\alpha \rightarrow 0$ is

$$E_{trial} = \frac{\hbar^2 \alpha^2}{2m} + c\alpha \quad (3.61)$$

and for α small enough E_{trial} is negative, attesting that the system admits bound states.

For our case, we can apply the same reasoning, replacing

- $V(x)$ with the effective potential V_{eff}
- x with the tortoise coordinate r_*
- c with the integral of the effective potential V_{eff} with respect to the tortoise coordinate
- E_{GS} with the frequency ω^2
- $\frac{\hbar^2}{2m}$ with 1.

It is important to emphasize that the condition Eq. 3.56 is only a sufficient condition, not necessary as well. In particular, if the integral of the effective potential is positive, it does not mean that the system is stable; conversely, if it is negative, the system is surely unstable. Qualitatively speaking we could think that, when it is negative, the perturbation has a bound state that "bounces" back and forth leading to exponential growth and instability.

Estimation of the threshold mass for Schwarzschild stable solution

We can use the condition Eq. 3.56 to give a first approximation of the normalized mass \hat{M} below which the Schwarzschild solution becomes unstable.

We examine a Schwarzschild spacetime characterized by a mass M , and a time-independent scalar field in the decoupling limit, wherein the backreaction of the scalar field

on the metric is neglected. We look for static bound state solutions, following the procedure explained in [30]. The scalar field can be expanded in spherical harmonics [31] as

$$\phi = \frac{1}{r} \sum_{l,m} \bar{\varphi}_{lm}(r) Y_{lm}(\theta, \varphi) \quad (3.62)$$

Considering spherically symmetric solutions, namely with $l = m = 0$, and naming $\bar{\varphi}_{00} = \bar{\varphi}$, the d'Alembertian operator for the scalar field becomes

$$\begin{aligned} \square\phi &= \frac{1}{r^2} \partial_r \left(r^2 g^{rr} \partial_r \phi \right) = \frac{1}{r^2} \partial_r \left(r^2 \left(1 - \frac{r_h}{r} \right) \partial_r \left(\frac{\bar{\varphi}}{r} \right) \right) = \\ &= \frac{1}{r^2} \partial_r \left(\bar{\varphi}''(r - r_h) + r_h \frac{\bar{\varphi}'}{r} - \bar{\varphi} \frac{r_h}{r^2} \right) \end{aligned} \quad (3.63)$$

where we fixed $\theta = \pi/2$. We omitted the spherical harmonic contribution, as it will be simplified out when the expression in Eq. 3.62 will be inserted in the Eq. 3.8.

Next, we introduce dimensionless variables defined as

$$\varphi = \frac{\bar{\varphi}}{r_h} \quad \rho = \frac{r}{r_h} \quad (3.64)$$

subsequently obtaining

$$\square\phi = \frac{\rho - 1}{r_h^2 \rho^2} \left[\varphi'' + \frac{1}{\rho - 1} \left(\frac{\varphi'}{\rho} - \frac{\varphi}{\rho^2} \right) \right]. \quad (3.65)$$

For the right-hand side of Eq. 3.8, we need to know the value of the Gauss-Bonnet invariant for Schwarzschild background. In Schwarzschild spacetime the Ricci tensor and the curvature scalar are both null, so from Eq. 2.38 the only term contributing to \mathcal{G} is the Kretschmann scalar Eq. 2.23. For Schwarzschild solution, its value in dimensionless variables is

$$K = R_{\mu\nu\alpha\beta} R^{\mu\nu\alpha\beta} = 12 \frac{r_h^2}{r^6} \rightarrow \frac{12}{r_h^4 \rho^6}. \quad (3.66)$$

The coupling constants included in \mathcal{F} have all dimension of a mass squared. Redefining all of them expressing them explicitly in terms of the event horizon radius squared times a dimensionless constant, we can simplify the r_h in the equation. Specifically, for instance in qsGB case, with coupling function $\frac{\eta}{8}\phi^2$, we transform the coupling constant as

$$\eta = \bar{\eta} r_h^2. \quad (3.67)$$

with $\bar{\eta}$ dimensionless.

Keeping for the moment the general form of the coupling function \mathcal{F} , from Eq. 3.8 we obtain

$$\begin{aligned} (\rho - 1) \left[\varphi'' + \frac{1}{\rho - 1} \left(\frac{\varphi'}{\rho} - \frac{\varphi}{\rho^2} \right) \right] &= -\mathcal{F}'(\varphi/\rho) \frac{12}{\rho^4} \\ \varphi'' + \frac{1}{\rho - 1} \left(\frac{\varphi'}{\rho} - \frac{\varphi}{\rho^2} + \mathcal{F}'(\varphi/\rho) \frac{12}{\rho^4} \right) &= 0 \end{aligned} \quad (3.68)$$

Now we introduce the tortoise coordinate ρ_* as in Eq. 2.29, but using ρ instead of r

$$\rho_* = \rho + \ln|\rho - 1| \quad (3.69)$$

with

$$\frac{d\rho_*}{d\rho} = \left(1 - \frac{1}{\rho}\right)^{-1} \equiv f. \quad (3.70)$$

Making the substitution of the variable in the previous equation and using the chain rule for derivatives as in Eqs. 3.43 we find

$$f^2 \frac{d^2\varphi}{d\rho_*^2} + \frac{d\varphi}{d\rho_*} \left(f' + \frac{f^2}{\rho^2}\right) + \frac{f}{\rho} \left(-\frac{\varphi}{\rho^2} + \frac{12}{\rho^4} \mathcal{F}'\right) = 0. \quad (3.71)$$

It is notable that the coefficient of the first derivative term vanishes, as

$$f' + \frac{f^2}{\rho^2} = \frac{1}{\rho-1} - \frac{\rho}{(\rho-1)^2} + \frac{1}{(\rho-1)^2} = 0 \quad (3.72)$$

so the equation simplifies to

$$\frac{d^2\varphi}{d\rho_*^2} - \frac{f}{\rho} \left(\frac{\varphi}{\rho^2} - \frac{12}{\rho^4} \mathcal{F}'\right) = 0. \quad (3.73)$$

Now a perturbation of the scalar field $\varphi \rightarrow \varphi_0 + \delta\varphi$, with φ_0 a solution of Eq. 3.68 is performed. We expand the Eq. 3.73 to first order in $\delta\varphi$, neglecting the terms of the order of $\delta\varphi^2$. We obtain

$$\frac{d^2\delta\varphi}{d\rho_*^2} - V_{eff}(\rho)\delta\varphi = 0 \quad (3.74)$$

where the effective potential has been defined as

$$V_{eff}(\rho) = \left(1 - \frac{1}{\rho}\right) \left(\frac{1}{\rho^3} - \frac{12}{\rho^5} \mathcal{F}'\right) \quad (3.75)$$

Thus, we finally got an expression for V_{eff} which can be integrated in the tortoise coordinate to check if the system admits bound states.

Let us assume quadratic coupling at first, with dimensionless coupling constant $\bar{\eta}$ as defined in Eq. 3.67. In this case, the integral of the effective potential is

$$\int_{-\infty}^{+\infty} V_{eff} d\rho_* = \int_1^{+\infty} \frac{V_{eff}}{1-1/\rho} d\rho = \int_1^{+\infty} \left(\frac{1}{\rho^2} - 3\frac{\bar{\eta}}{\rho^6}\right) d\rho = \frac{1}{2} - \frac{3\bar{\eta}}{5} \quad (3.76)$$

If we want this integral to be negative as suggested by Eq. 3.56, the coupling constant must be $\bar{\eta} > 5/6 \simeq 0.83$. Therefore we are sure that for coupling constant greater than 0.83 the Schwarzschild solution is unstable. Actually, as we will show in the next section through numerical analysis, the limiting value of the coupling constant for which Schwarzschild solution is stable¹⁴ is $\bar{\eta} = 0.7256$. For that value, the effective potential integral is still positive: we recall once again that condition Eq. 3.56 is only sufficient for instability.

¹⁴We will refer to it as the *bifurcation point* in the next section, when speaking about the correspondent normalized mass \hat{M}

Let us now anticipate results of Sec. 3.4 for quartic coupling function Eq. 3.88. In this case the integral in Eq. 3.76 is¹⁵

$$\int_1^{+\infty} \frac{V_{eff}}{1-1/\rho} d\rho = \frac{1}{2} - \frac{3\bar{\eta}}{5} - 9\bar{\lambda} \int_1^{\infty} \frac{\sigma_0^2}{\rho^6} d\rho < 0. \quad (3.77)$$

where $\sigma_0 = \varphi_0/\rho$.

This means that the Schwarzschild solution is unstable for $\bar{\lambda} > 0.8\bar{\eta}$.

So now the value of the scalar field does get involved in the stability, together with the coupling constant of the quartic term. We see how the result can be positive even in the region of unstable solution for the quadratic case if $\bar{\lambda}$ is negative, greater in module than a certain value $\bar{\lambda}_{lim}$, and for $\varphi_0 \neq 0$. Thus, in the quartic case, where Schwarzschild solution are guaranteed for $\varphi_0 = 0$ and for $\varphi_0 = \varphi_{\pm} = \pm \sqrt{-\frac{\bar{\eta}}{\bar{\lambda}}}$, if we consider the second option alongside with $\bar{\lambda} < -\bar{\lambda}_{lim}$ ¹⁶ even GR solution can be stable for the whole mass range. This will be shown in the next Section, in particular in Fig. 3.17 where we obtain numerically the results just presented.

Moreover this also suggests that, in theories where the coupling function has more terms than just the quadratic one, in regions of mass \hat{M} where the Schwarzschild BH is unstable, conversely the scalarized solution may be not. This is exactly the spontaneous scalarization phenomenon.

3.3.3 Numerical implementation

For the whole analysis of stability it is worth to work with compactified variables. Defining

$$x = 1 - \frac{r_s}{r} \quad (3.78)$$

it is possible to map the whole space in the interval $[0, 1]$, where $x = 0$ corresponds to the event horizon and $x = 1$ to infinity.

We proceed with the integration of the background field equations, necessary for the computation of the coefficients of the perturbed equation Eq. 3.29. It is less complicated to integrate directly Eq. 3.29 in compactified coordinates, rather than its Schrödinger-like form Eq. 3.47, therefore we will use the former.

For the integration method we follow the algorithm explained in [9] and in [30]. Firstly, we select a guess value of the frequency ω_I . Only the imaginary part of the actual pulsation is considered, as already explained.

We conduct two separate integrations. The first one starts from the horizon and the other from infinity, both ending at an intermediate point x_m , where the two solutions will be matched. The solution of the former will be called $\varphi^{(-)}$ while the other $\varphi^{(+)}$. Numerical issues, due to the ill definition of coordinate towards $x \rightarrow 0$ and $x \rightarrow 1$, prevent us to start the integration exactly from those values. This also implies that the boundary conditions are no longer the ones written in Eqs. 3.52, 3.53, i.e. the solution is not purely ingoing/outgoing waves, respectively at values that are not exactly $x = 0$ and $x = 1$. Towards infinity we checked that it is not necessary to go that far to reach asymptotic behavior of the solution, because

¹⁵Here also the coupling constant $\bar{\lambda}$ has to be intended as dimensionless, as $\lambda = \bar{\lambda} r_h^2$. Indeed λ has dimension of a mass squared too.

¹⁶We will see that $\bar{\lambda}_{lim}$ is roughly $\bar{\lambda}_{lim} = 0.8\bar{\eta}$

the effective potential vanishes slightly soon, as shown as an example in Fig. 3.10. This allows us to choose as "infinity" the value $x_{max} = 0.99$, which corresponds to $r = 100$ with $r_h = 1$ in radial coordinates. Boundary conditions for the integration that starts from infinity are then

$$\begin{cases} \varphi^{(+)}(x_{max}) = 0 \\ \varphi'^{(+)}(x_{max}) = \text{const} \end{cases} \quad (3.79)$$

with the constant set to a value different from zero. φ' indicates the first derivative of the perturbation of the field with respect to x .

For the other boundary, the situation is somewhat more intricate. Indeed, the effective potential exhibits a steep slope towards the horizon. This makes it challenging to identify a sufficiently close distance different from 0 where BCs Eq. 3.80 can be applied. We should expand the equation around $x = 0$ and compute analytically the conditions that the perturbation must satisfy at a finite distance greater than the horizon radius. However, considering the tortoise coordinate of the scalarized solution as well described by the Schwarzschild tortoise coordinates Eq. 2.29 represents a viable first approximation. Thus we select a finite x_{min} for example $x_{min} = 10^{-8}$ and impose

$$\begin{cases} \varphi^{(-)}(x_{min}) = e^{\omega_I r_\star^{Sch}(x)} \\ \varphi'^{(-)}(x_{min}) = \frac{d}{dx}(e^{\omega_I r_\star^{Sch}(x)}) \end{cases} \quad (3.80)$$

where $r_\star^{Sch}(x)$ is

$$r_\star^{Sch}(x) = \frac{r_h}{1-x} + r_h \ln\left(\frac{x}{1-x}\right), \quad (3.81)$$

i.e. the tortoise coordinate for Schwarzschild BH as a function of the compactified coordinate.

Clearly this approximation is suitable not so close to the horizon where the effect of the scalar field on the background field is less significant.

Once the two solutions are computed, we should demand whether they are linearly dependent on a given pulsation ω_I . For this purpose we analyze the Wronskian of the two solutions, defined as

$$W = \left[\varphi^{(-)} \varphi'^{(+)} - \varphi'^{(-)} \varphi^{(+)} \right]_{x=x_m}. \quad (3.82)$$

When the Wronskian vanishes, the ω_I is an eigenfrequency of the system. Conversely, if there are no frequencies for which $W = 0$ then the scalarized solution is supposed stable under radial perturbations.

Naturally, the Wronskian should not depend on the choice of the intermediate point x_m , where the two solutions are matched together and where W is evaluated. This is true for second order differential equations that can be cast into the form

$$\mathbf{L}\varphi = \left[\frac{1}{w}(\mathbf{D}p\mathbf{D} + q) \right] \varphi = 0 \quad (3.83)$$

with \mathbf{L} a linear operator, \mathbf{D} the differential operator, p and q two different functions of the independent variable and w a positive function [7]. As we have already demonstrated, the

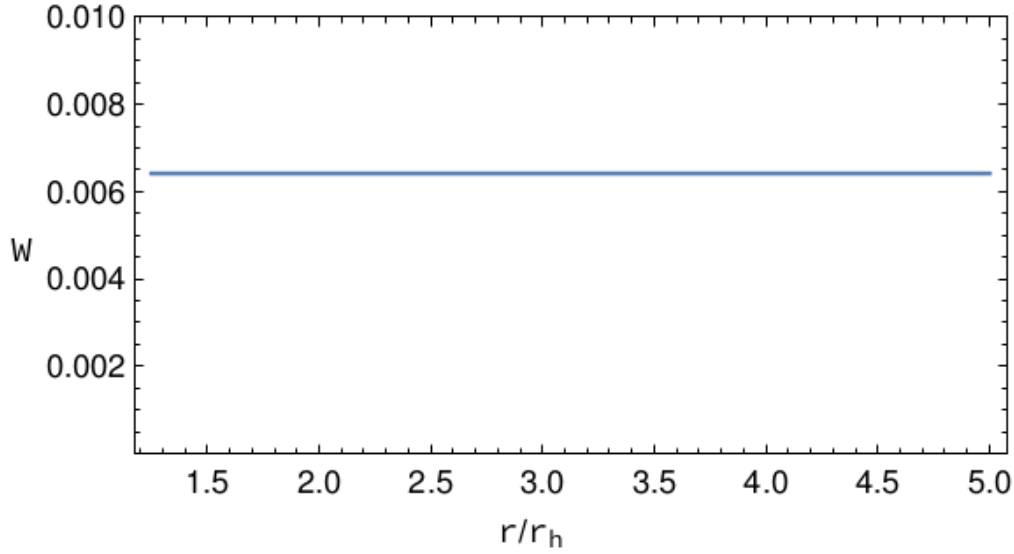


Figure 3.11: Wronskian $W = \left[\varphi^{(-)} \varphi'^{(+)} - \varphi'^{(-)} \varphi^{(+)} \right]_{x=x_m}$ as a function of the intermediate point x_m written in radial coordinate r for a scalarized solution in sGB gravity with $\eta = 0.6975$ and $\omega_I = 0.0359$. We can appreciate how the Wronskian is constant as expected.

perturbed equation can actually be written in that form, as shown in Eq. 3.47, identifying $p = 1$, $w = 1$, $q = (\omega^2 - V_{eff})$ and $D = \frac{d}{dr_*}$. Thus we check the independence of the Wronskian on x_m through this change of variables and we obtain the result exposed in Fig. 3.11.

Shooting method for the eigenfrequencies To accomplish the task of finding the eigenfrequencies of unstable mode we perform a shooting method. We start from a guess value of ω_I and integrate the perturbed equation from the horizon and from infinity. Subsequently, we compute the Wronskian and verify if it equals zero. If not, we adjust the value of ω_I and repeat the process. Since it is independent on the value of the intermediate point, we set $x_m = 0.5$. In order to enhance precision, we first evaluate Wronskians over a wide frequency range with larger interval between them. Subsequently, we focus on the region surrounding the frequencies where W vanishes and conduct further computations with increased precision. We apply the Theorem of zeros on the resulting trend of the Wronskian as a function of ω_I .

For quadratic coupling, plotting the Wronskian value as a function of the imaginary part of the frequency, we obtain a curve like the one in Fig. 3.12.

Following this method, it is possible to derive that the whole fundamental branch of scalarized solutions for quadratic coupling is unstable under radial perturbations, as shown in Fig. 3.13.

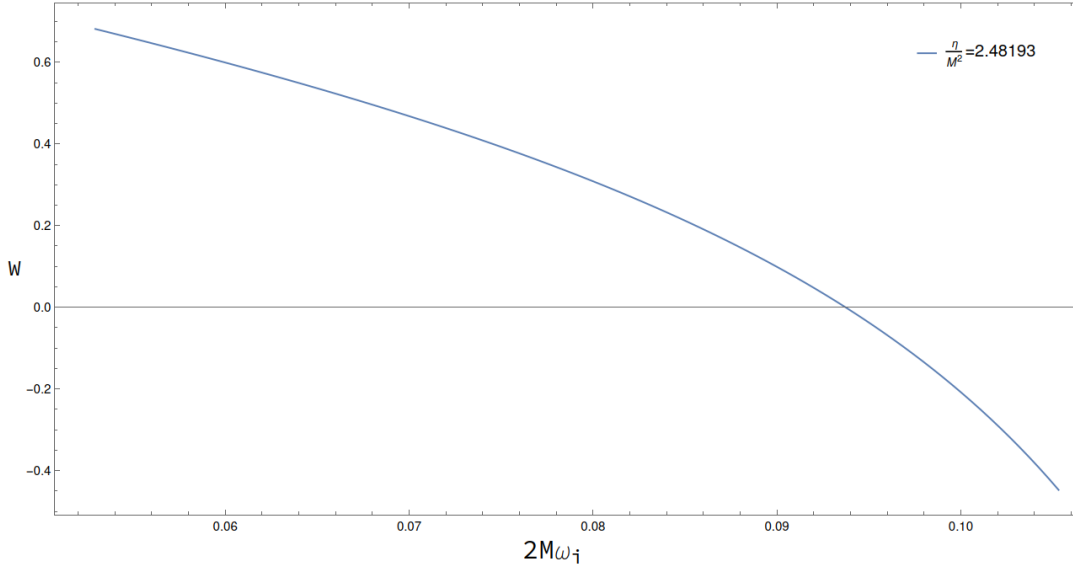


Figure 3.12: Wronskian as a function of $2M\omega_I$ for a scalarized solution for quadratic coupling with $\eta/M^2 = 2.47836$. The curve crosses the abscissa axis, meaning that the corresponding scalarized solution is unstable.

Stability of the Schwarzschild solution It is important to verify the stability of the Schwarzschild solution as well.

In order to do that, the metric functions of the background spacetime should be set equal to the Schwarzschild metric ones and the scalar field needs to be trivial. Explicitly, in compactified coordinate, we request

$$\begin{cases} A_{sch}(x) = B_{sch}(x) = x \\ \phi(x) = 0. \end{cases} \quad (3.84)$$

The perturbed equation Eq. 3.29 is manipulated imposing the conditions Eq. 3.84 above obtaining an expression which is way shorter than the general one¹⁷ so we can report it here

$$-\frac{\varphi(x)[x(x-1)^3 + \omega^2 + 12x(x-1)^6 \mathcal{F}''(0)] + x(x-1)^3[(3x-1)\varphi'(x) + x(x-1)\varphi''(x)]}{(x-1)^6} = 0. \quad (3.85)$$

For quadratic coupling function it becomes

$$-\frac{\varphi(x)[x(x-1)^3 + \omega^2 + 3x(x-1)^6 \eta] + x(x-1)^3[(3x-1)\varphi'(x) + x(x-1)\varphi''(x)]}{(x-1)^6} = 0 \quad (3.86)$$

We follow the same procedure illustrated above for scalarized solutions to identify the eigenfrequencies of the unstable modes for the Schwarzschild case. The result is shown in Fig. 3.13.

The result is in accordance with the one illustrated in [30]. We can appreciate how the Schwarzschild solution starts to be unstable at higher coupling constant values (lower masses), exactly when scalarized BHs are no longer included in the spectrum of solutions. On the contrary, where the fundamental branch exists, i.e. in ranges Eq. 3.24, only

¹⁷See Appendix A.

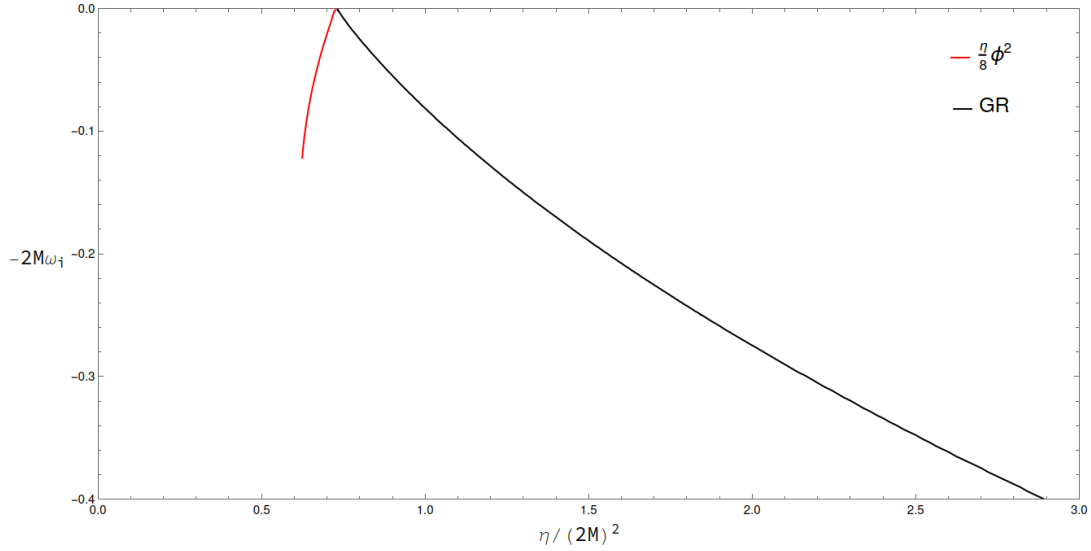


Figure 3.13: Dimensionless eigenfrequencies of the unstable modes $-2M\omega_I$ as a function of the normalized coupling constant η/M^2 for quadratic coupling function. In red the fundamental branch of scalarized solutions is shown, while in black the Schwarzschild solution.

Schwarzschild BH is stable.

The value of the normalized mass $\hat{M} = M/\eta^{1/2}$ at which the onset of scalarized solutions arise is called *bifurcation point* \hat{M}_{bp} . Here, for quadratic coupling, this point coincides with the beginning of the instability region of GR solution, meaning that there are no physical solutions for masses below the threshold value \hat{M}_{bp} [30]. \hat{M}_{bp} can be estimated to be

$$\hat{M}_{bp} = \left(\frac{M}{\eta^{1/2}} \right)_{bp} \simeq 0.58697. \quad (3.87)$$

In Fig. 3.14 we illustrate the phenomenology of quadratic coupling function, plotting the same results of Fig. 3.8 updated with the stability analysis as in [9]. Note that also branches of multiple nodes-solutions are unstable.

3.4 Quartic coupling function

In [30] the authors showed that adding a quartic term to the quadratic coupling function could eventually lead to stable scalarized BH, depending on the value of the coupling constants. In this section we reproduce the results of [30].

We consider the following coupling function

$$\mathcal{F}(\phi) = \frac{\eta}{8}\phi^2 + \frac{\lambda}{16}\phi^4 \quad (3.88)$$

with η and λ both of mass squared dimension.

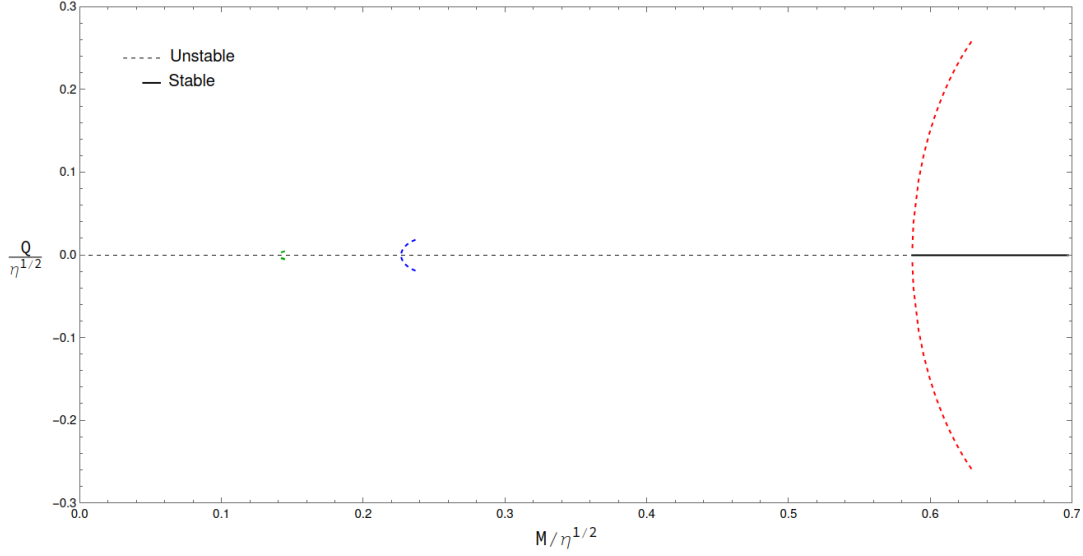


Figure 3.14: Normalized scalar charge \hat{Q} as a function of \hat{M} for quadratic coupling function. In red the fundamental branch, in blue the one-node branch, in green the two-nodes branch, in black Schwarzschild BHs branch. Dashed lines represent the unstable solutions while straight lines the stable ones. We notice the absence of stable solutions for masses below the bifurcation point $\hat{M}_{bp} = 0.58697$.

3.4.1 Numerical results

We can proceed with the numerical analysis of solutions for coupling Eq. 3.88. The method is analogue to the one used in the previous chapter for quadratic coupling. The only thing we should pay attention at is that the regularity condition in Eq. 3.22 cannot be reduced to the study of the sign of a parabola. Indeed, depending on the sign of λ , the coupling constant of the quartic term, the function

$$f_{reg}(\phi_h) = r_h^4 - 96(\mathcal{F}'(\phi_h))^2 \quad (3.89)$$

can have more than one zeros¹⁸ and can be positive in detached ranges of ϕ . This happens for $\lambda < 0$, while for positive values the function never changes its concavity and admits only one zero. In Fig. 3.15 is illustrated an example of what we have just explained, for three different values of η and for $\lambda = -1.5\eta$.

When we shoot the values of the scalar field at the horizon in order to find scalarized solution, then we should take into account the shape of the function f_{reg} and consider all the regions where it is positive, otherwise we could miss some solutions.

We can expose the results that we got for three different values of λ : $\lambda = \pm 0.5\eta$, $\lambda = \pm 1\eta$ and $\lambda = \pm 1.5\eta$. Firstly, the scalarized solution branches have been computed and subsequently we checked their stability.

In Fig. 3.16 we illustrate the normalized scalar charge \hat{Q} as a function of the normalized mass \hat{M} for quartic and quadratic couplings. The left (right) region in yellow (purple) corresponds to stable (unstable) scalarized solutions. Opposite, stable (unstable) Schwarzschild

¹⁸We still analyze only positive values of ϕ_h , as the coupling function Eq. 3.88 is \mathbb{Z}_2 -symmetric like for qsGB.

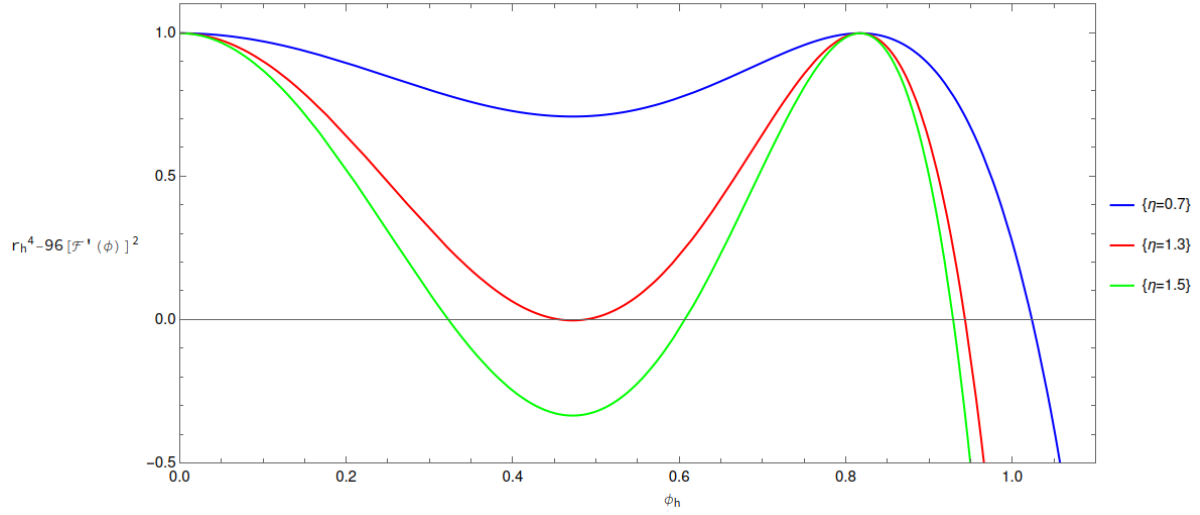


Figure 3.15: Regularity condition function Eq. 3.89 for quartic coupling Eq. 3.88 with $\lambda = -1.5\eta$ and for different values of η .

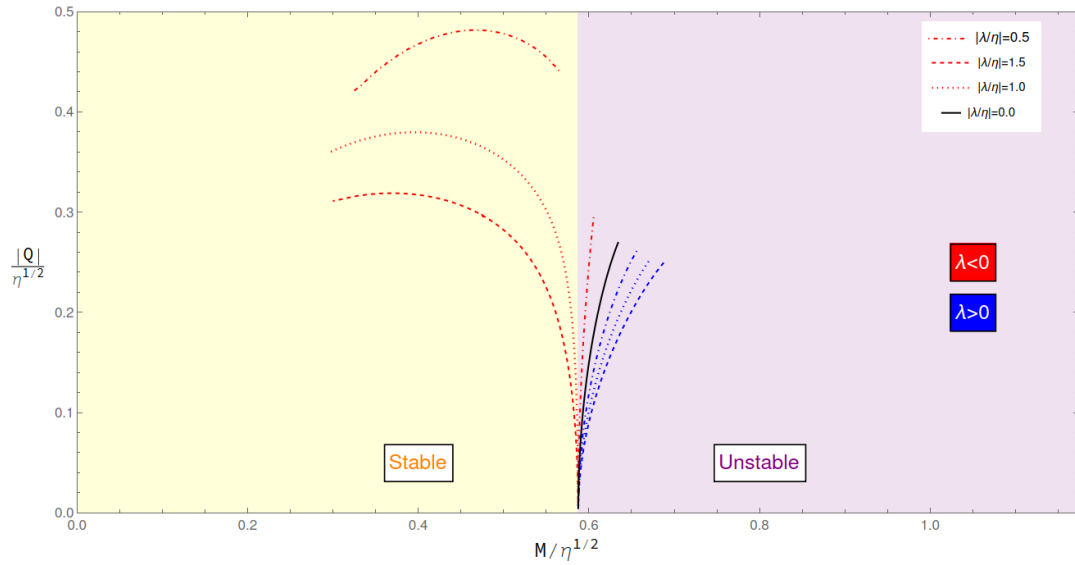


Figure 3.16: Scalar charge \hat{Q} against mass \hat{M} for quartic coupling function (in red and blue) and purely quadratic (in black). Only fundamental branches are shown. Red lines refer to positive values of λ , while blue ones to negative values. The purple region indicates for which values of \hat{M} Schwarzschild solution is stable, and scalarized solutions are unstable; the yellow region conversely hosts unstable Schwarzschild BHs and stable scalarized ones. The two regions are divided by the bifurcation point \hat{M}_{bp} (Eq. 3.87). Schwarzschild solutions are not shown, as they stand on the $\hat{Q} = 0$ line.

BHs occupy the right (left) side of the abscissa, with $\hat{Q} = 0$. The bifurcation point \hat{M}_{bp} separates the two regions.

As expected from the reasoning made in the previous section, we cannot get stable solution if all terms in the coupling function are positive (see Eq. 3.77). Indeed, in Fig. 3.16 is illustrated how blue lines, for which λ values are positive, stand all in the "unstable region". Red lines whose λ values are negative, can manage to stand in the stable side for values of the quartic coupling constant greater (in module) than $|\lambda/\eta|_{thr} = 0.8$.

All these results are in accordance with the ones obtained in [30].

Stability of the other scalar trivial solutions

Let us consider again the coupling function Eq. 3.88. Analyzing Fig. 3.16 we note that even if negative λ can yield stable solutions, the regularity condition Eq. 3.22 still imposes a restriction on the extension of the branch towards lower masses. It seems that even in this case the theory does not admit physical solutions within a certain range of masses $[0, \hat{M}_{min}]$, where \hat{M}_{min} represents the minimum value of normalized mass \hat{M} where scalarized solution is computed. Its value depends on the ratio of the coupling constants λ/η .

However, we have not taken into account all the possible black hole solutions permitted by the quartic theory. In fact, from condition Eq. 3.9 we derive that, in quartic case, two more trivial values the scalar field, alongside with $\phi_0 = 0$, are included within the Schwarzschild-like background. Indeed, solving $\mathcal{F}_{,\phi} = 0$ we obtain

$$\begin{cases} \phi_0 = 0 \\ \phi_{\pm} = \pm \sqrt{-\frac{\eta}{\lambda}}. \end{cases} \quad (3.90)$$

We can analyze, then, the stability of these trivial solutions. Actually, it is possible to study just ϕ_+ case, thanks to the symmetry of the potential.

The perturbed equation for Schwarzschild background for quartic coupling considering $\phi = \phi_+$ is slightly different from the one with constantly null $\phi_0 = 0$ scalar field, since the second derivative of the coupling function is not vanishing at $\phi = \phi_+$ (see Eq. 3.85). We can write it, using compactified coordinate, as

$$\frac{1}{(x-1)^6} \left\{ x(1-x)^3 \varphi(x) [1 + 3(x-1)^3 (\eta + 3\lambda\phi_+^2)] - \omega^2 \varphi(x) - x(x-1)^4 \varphi'(x) - x^2(x-1)^3 [2\varphi'(x) + (x-1)\varphi''(x)] \right\} = 0. \quad (3.91)$$

With the substitution $\phi_+ \rightarrow 0$ Eq. 3.91 reduces to Eq. 3.86 for Schwarzschild background in qsGB, as expected.

Solving the Eq. 3.91 with $\phi_+ = \sqrt{-\frac{\eta}{\lambda}}$ and ratio $\frac{\eta}{\lambda} < 0$ we can compute the Wronskian W and check the stability of the solutions. We figure out that there are no frequency values for any coupling constant η for which $W = 0$, therefore we conclude that these solutions are stable. In Fig. 3.17 are summarized the results exposed.

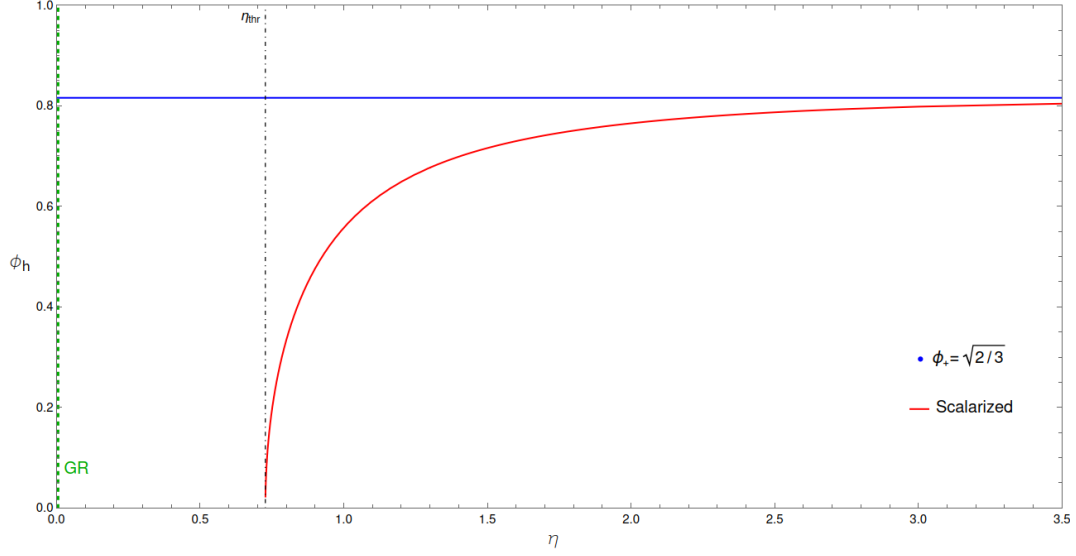


Figure 3.17: Value of the scalar field at the horizon as a function of the coupling constant η of the quadratic term of $\mathcal{F}(\phi)$. In red it is reported the fundamental branch for the ratio $\frac{\lambda}{\eta} = -1.5$. The vertical dot-dashed line represents the threshold value of the mass for the onset of scalarization, i.e. the bifurcation point. In blue, the Schwarzschild solution with constant scalar field at the fixed value $\phi_+ = \sqrt{-\frac{\eta}{\lambda}} = \sqrt{2/3}$. This branch is stable for all values of η .

Although we have found a stable solution even in the range of masses below the minimum mass \hat{M}_{min} , this branch does not represent a viable physical result. In fact, as discussed in Sec. 3.2, we want to find solutions that are compatible with the empirical evidences that we observe, which state that GR is trusted in the asymptotic region, far from large curvature environments. Consequently, we should discard the BH which induces a Schwarzschild-like metric but with a scalar field different from zero, since the latter does not vanish towards infinity.

Chapter 4

Exploring diverse coupling functions

In the previous chapter we showed how the mechanism of spontaneous scalarization works and we checked the reliability of our methodology and our algorithms by comparing the results obtained in the existing literature within the quadratic and quartic sGB theories. Now we can move a step forward, using the tools just developed to analyze wider classes of coupling functions.

The following chapter is dedicated to show all the original results found in this thesis work.

Why considering other couplings? Although we have demonstrated that black holes with non-trivial scalar hair do exist within the scalar-Gauss-Bonnet gravity, the coupling functions investigated thus far exhibits important issues. Quartic coupling can yield stable scalarized branches (Fig. 3.16), but these are still limited because of the regularity condition Eq. 3.22. Below the threshold value of the mass at which there is the onset of scalarization, the bifurcation point \hat{M}_{bp} of Eq.3.87, Schwarzschild solution is unstable either. This implies that the theory is ill posed because there is an entire range of masses where no physical black hole solutions are admitted. Moreover, our aim is to find different solutions from GR predictions in the strong-field regime, which is towards the small mass limit/small horizon radii. It is important to investigate that limit through other couplings as well because it should provide restrictions on the viability of the theory in extreme regions.

In this chapter we will analyze the phenomenology of BH solutions for the following couplings:

- **Pure Quartic coupling function** (Sec. 4.1)
- **Cubic coupling functions** (Sec. 4.2)
- **Exponential coupling function** (Sec. 4.3)
- **Lorentzian coupling function.** (Sec. 4.4)

4.1 Pure Quartic coupling function

After the analysis of the combination of the quadratic and quartic terms in Sec. 3.4, we proceed studying the case where only the quartic term is present, i.e. with $\eta = 0$ in Eq. 3.88 :

$$\mathcal{F}(\phi) = \frac{\eta}{16}\phi^4. \quad (4.1)$$

Thus far, every coupling function examined has exhibited the same form in the vicinity of $\phi = 0$, namely $\mathcal{F}(\phi) = \eta\phi^2/8 + \dots$. This is the first time we consider a coupling function that has not that behavior for small scalar field.

In this case we should pay attention also to the behavior of the Schwarzschild solution. The effective potential in the decoupling limit is, from Eq. 3.75,

$$V_{eff}(\rho) = \left(1 - \frac{1}{\rho}\right) \left(\frac{1}{\rho^3} - \frac{3}{\rho^5} \mathcal{F}'\right) = \left(1 - \frac{1}{\rho}\right) \left(\frac{1}{\rho^3} - \frac{9}{\rho^8} \bar{\eta} \varphi_0^2\right). \quad (4.2)$$

where we took into account only linear terms in the scalar field perturbation. The integral of the effective potential in the tortoise coordinate is

$$\int_1^{+\infty} \frac{V_{eff}}{1 - 1/\rho} d\rho = \frac{1}{2} - 9\bar{\eta} \int_1^{\infty} \frac{\sigma_0^2}{\rho^6}. \quad (4.3)$$

where $\sigma_0 = \varphi_0/\rho$.

In Sec. 3.3.2 we showed that if this integral is negative this automatically implies that the solution is unstable. For Schwarzschild solution, however, the scalar field for pure quadratic coupling must be zero. Therefore, the integral Eq. 4.3 is positive for all coupling constants η . This means that from this condition we cannot determine whether Schwarzschild solution is unstable or not. We should remember that such a condition is just sufficient to determine the stability of the solution, thus we proceed investigating numerically its solutions spectrum.

The perturbed equation for the Schwarzschild solution with pure quartic coupling is

$$\frac{x(1-x)^3\varphi(x) - \omega^2\varphi(x) - x(x-1)^4\varphi'(x) - x^2(x-1)^3[2\varphi'(x) + (x-1)\varphi''(x)]}{(x-1)^6} = 0, \quad (4.4)$$

which is slightly different from the one for quadratic coupling (Eq. 3.86) since here the second derivative of $\mathcal{F}(\phi)$ is vanishing when evaluated in $\phi = 0$ (see Eq. 3.85). Nevertheless, performing the shooting method to find the eigenfrequencies of the unstable modes for the Schwarzschild solution, we were not able to find any of them for any value of \hat{M} . Thus, we can conclude, basing on the analysis of the effective potential and on the numerical results, that Schwarzschild solution is always stable, for the whole range of masses down to $\hat{M} = 0$.

This finding does not prevent us from searching for scalarized solutions, though. In Fig. 4.1 we show the scalarized branch of pure quartic coupling function compared with the fundamental branch of qsGB.

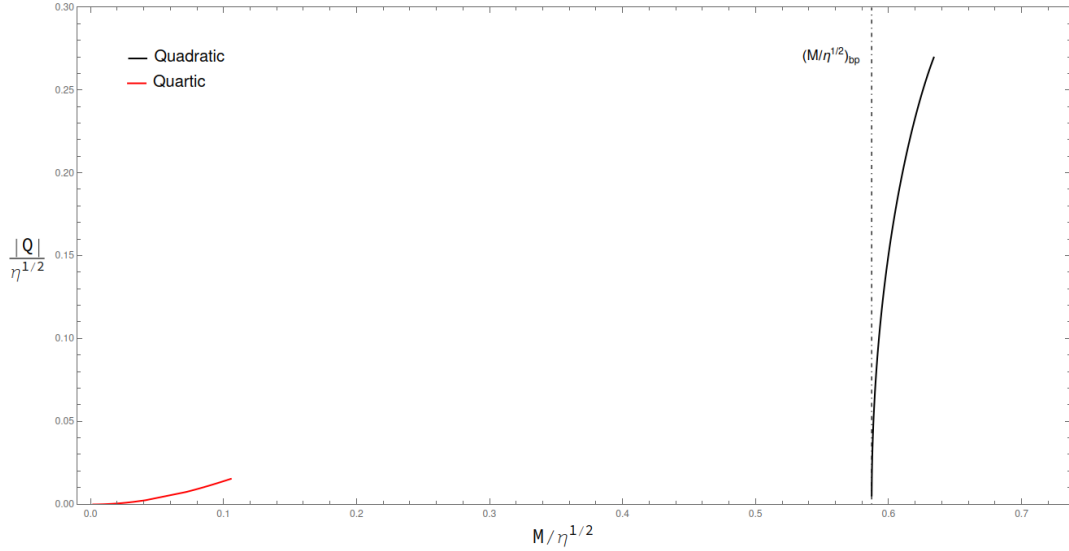


Figure 4.1: Normalized scalar charge \hat{Q} against normalized mass \hat{M} for purely quartic coupling function Eq. 4.1 (in red) and purely quadratic Eq. 3.18 (in black). Only fundamental branches are shown. The dot-dashed line represents the bifurcation point for quadratic case, Eq. 3.87.

We note that there are some similarities with the case of the quadratic coupling, since, as expected, the whole fundamental branch is unstable. In fact, similar to qsGB, the scalarized branch emerges in the region where the Schwarzschild solution is stable, which corresponds to the entire positive abscissa axis in Fig. 4.1 for purely quartic coupling. In contrast to the quadratic case, the concavity of the branch is upward. Continuing with similarities, there exists a mass limit imposed by the regularity condition, which manifests as an upper mass limit. Scalarized solutions only exist for masses satisfying $\hat{M} < \hat{M}_{max} = 0.105185$. This behavior is common for all unstable branches of polynomial coupling functions encountered thus far (Fig. 3.16). Nevertheless, in the quartic case there is no minimum mass and no proper bifurcation point. Indeed, the latter is actually translated towards $\hat{M} \rightarrow 0$, since the Schwarzschild solution is always stable. Moreover, scalarized solutions manage to reach infinitesimal masses as well. Differently from the quadratic and quadratic+quartic couplings, here the theory shows no mass gaps where no standing physical solutions are admitted. However, due to the instability of the scalarized branch we can affirm that this case is effectively analogue to GR.

One might speculate that the scalarized branch arises merely due to algorithmic failure at small masses. To address this concern in Fig. 4.2 we display the value of the scalar field at infinity as a function of the scalar field at the horizon for different values of the coupling constant η . For coupling constant $\eta = 0.7$, where the fundamental branch of qsGB occurs, the regularity condition prevents the existence of scalarized solution, truncating the function before it encounters a second zero, aside from the origin.

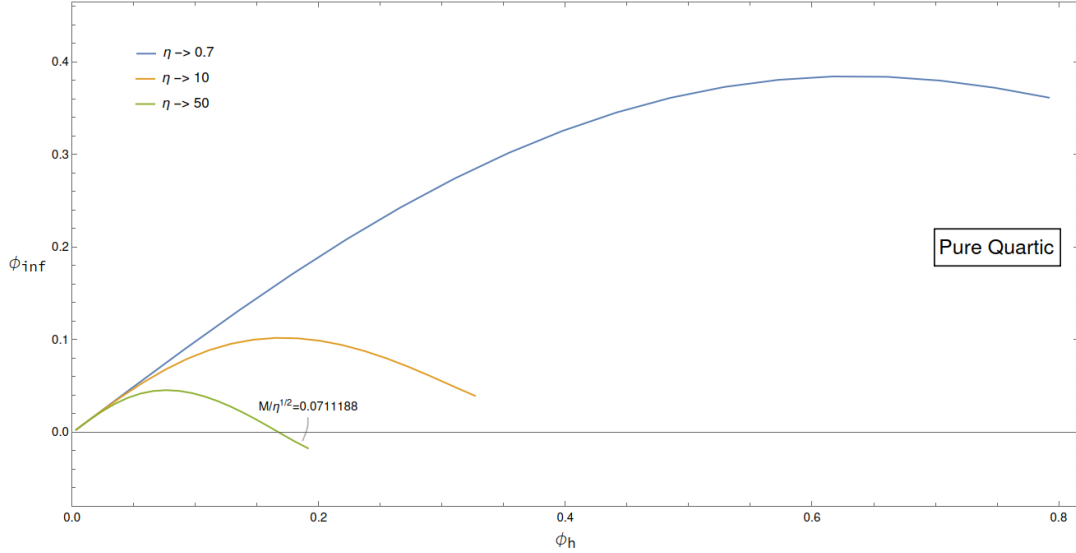


Figure 4.2: Value of the scalar field at infinity ϕ_∞ as a function of the scalar field at the horizon ϕ_h for quartic coupling function, for different values of the coupling constant η .

4.2 Cubic coupling function

We have stated in Sec. 3.2 that one of the common requirements in the literature is that the coupling function must be symmetric under the transformation $\phi \rightarrow -\phi$. This has been demanded because a shift symmetric term¹ in the action, such as $\phi\mathcal{G}$, would induce hairy black holes, but it would exclude GR solutions [32]. Therefore, in order to maintain the mechanism of spontaneous scalarization and to regard our action as an Effective Field Theory (EFT) expansion of a more fundamental theory, we should ensure that the exclusion of the linear term arises from a symmetry of the theory.

Nevertheless, the only necessary condition that the coupling function must satisfy for the spontaneous scalarization to manifest is that its first derivative must vanish when evaluated at a certain ϕ_0 . Thus, in principle, nothing prevents us from considering a \mathbb{Z}_2 -violating coupling function as

$$\mathcal{F}(\phi) = \frac{\eta}{12} \phi^3. \quad (4.5)$$

We search for scalarized solutions with the coupling in Eq. 4.5. Even if the result now varies if we change sign to the scalar field at the horizon, we still consider only positive values of ϕ_h . Indeed, our investigation revealed that not only we found no solutions with vanishing ϕ_{inf} for negative values of ϕ_h , but ϕ_{inf} diverges negatively as ϕ_h becomes more negative. This may justify our choice. In Fig. 4.3 we present the results.

As we can observe, scalarized solutions do emerge for the cubic coupling. Comparing its fundamental branch with those of purely quadratic and purely quartic couplings, we notice similarities between the cubic and quartic cases. Indeed, cubic scalarized branch reaches infinitesimal masses with an upward concavity and presents no bifurcation points, standing

¹It is shift symmetric since under global shifting transformations like $\phi \rightarrow \phi + \delta\phi$ (with $\delta\phi$ constant) the extra term $\delta\phi\mathcal{G}$ does not affect the equations of motions since Gauss-Bonnet term \mathcal{G} is a total divergence in four dimension [21].

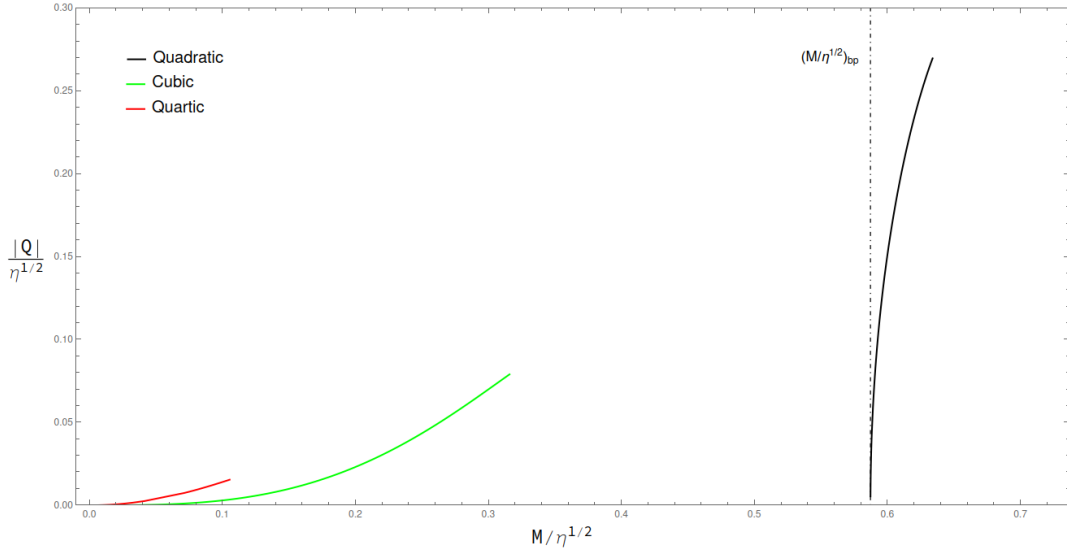


Figure 4.3: Normalized scalar charge \hat{Q} against normalized mass \hat{M} . It displays the comparison between one-term polynomial coupling functions: quadratic (Eq. 3.18), cubic (Eq. 4.5), quartic (Eq. 4.1). All the branches shown are the fundamental ones and are unstable under radial perturbations. The bifurcation point of Eq. 3.87 for quadratic coupling is also highlighted.

on the left side of the bifurcation point \hat{M}_{bp} of quadratic theory. All the displayed branches are fully unstable under radial perturbations. Indeed, as for quartic case in Sec. 4.1, the perturbed equation for Schwarzschild background is the one written in Eq. 4.4, because both first and second derivatives of the coupling function vanish for $\phi_0 = 0$. This implies that the solutions are the same, meaning that Schwarzschild BHs are always stable, as demonstrated above.

Even in this case the integral of the effective potential for Schwarzschild scalar field configuration is positive no matter the value of the coupling constant, as we can see from Eq. 4.6 with $\sigma_0 = 0$.

$$\int_1^{+\infty} \frac{V_{eff}}{1 - 1/\rho} d\rho = \frac{1}{2} - 6\bar{\eta} \int_1^{+\infty} \frac{\sigma_0}{\rho^6} d\rho. \quad (4.6)$$

In Fig. 4.4 we show how, due to the regularity condition Eq. 3.22, the function $\phi_{inf}(\phi_h)$ manifests a second non-trivial zero only in qsGB case, for a value of the coupling constant that stands in the fundamental branch of quadratic coupling.

However, we think that adding a cubic term to the pure quadratic coupling could yield stable scalarized solutions, similarly to the quadratic + quartic coupling Eq. 3.88, with negative λ values. In fact, it should make the integral of the effective potential positive (see Sec. 3.3.2) with the proper sign of its coupling constant, as we have demonstrated in the decoupling limit for the quartic case in Eq. 3.77.

Thus, if we take into account the coupling function:

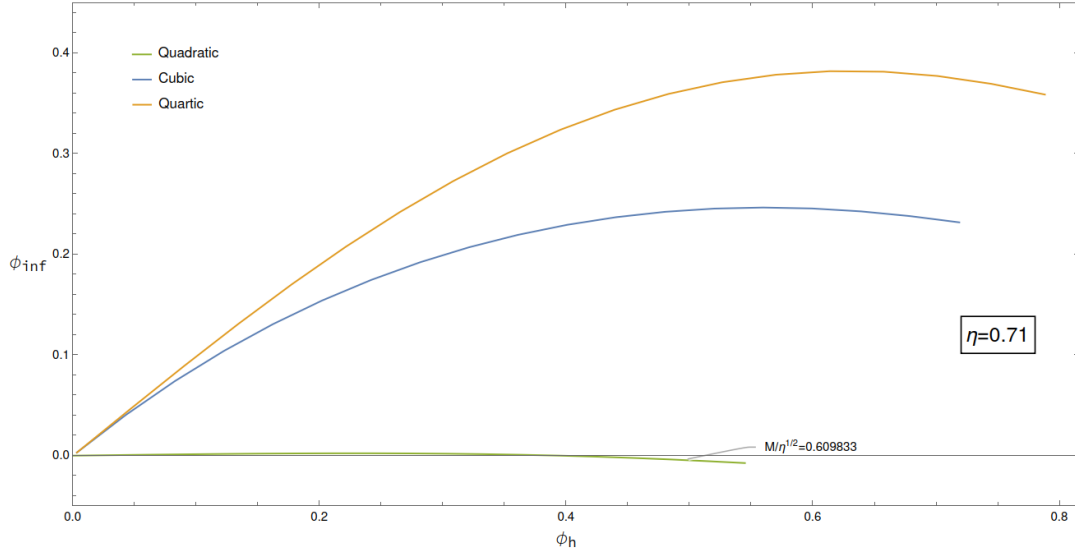


Figure 4.4: Value of the scalar field at infinity as a function of the scalar field at the horizon for quadratic, cubic and quartic coupling functions.

$$\mathcal{F}(\phi) = \frac{\eta}{8}\phi^2 + \frac{\lambda}{12}\phi^3 \quad (4.7)$$

the integral of the effective potential for Schwarzschild background is

$$\int_1^{+\infty} \frac{V_{eff}}{1-1/\rho} d\rho = \frac{1}{2} - \frac{3}{5}\bar{\eta} - 6\bar{\lambda} \int_1^{\infty} \frac{\sigma_0}{\rho^6}. \quad (4.8)$$

Hence, we can deduce that the integral is positive if $\bar{\lambda} < 0$ and greater in module than a certain limit value λ_{lim} .

The perturbed equation for Schwarzschild background is the same as the one in Eq. 3.86, then the bifurcation point should coincide with \hat{M}_{bp} of quadratic theory in Eq. 3.87. We expect the same behavior of scalarized solutions as quadratic + quartic case

We search for scalarized solutions only using positive values of the scalar field at the horizon, since solutions are invariant under transformations

$$\phi \rightarrow -\phi \quad \text{together with} \quad \lambda \rightarrow -\lambda. \quad (4.9)$$

The results, reported in Fig. 4.5, confirm our hypothesis. Exactly like the quartic coupling case, fundamental branches of scalarized solutions are stable for negative values of λ , exceeding in magnitude a certain threshold value λ_{lim} . These stable solutions arise on the left side of the bifurcation point \hat{M}_{bp} . We conducted a rough estimation of the threshold value of λ_{lim} for the onset of scalarization and we found that it is $\lambda_{lim} = k\eta \approx -0.7\eta$. Indeed, with the sensitivity of the algorithm, no hairy BHs were produced for $k \in [-0.7, 0]$.

For positive values of λ , instead, every solution is unstable, no matter the value it has, as we expected. In Fig. 4.6 we show the eigenfrequencies of the unstable modes for $\lambda = \eta$, compared with the one of the pure quadratic coupling.

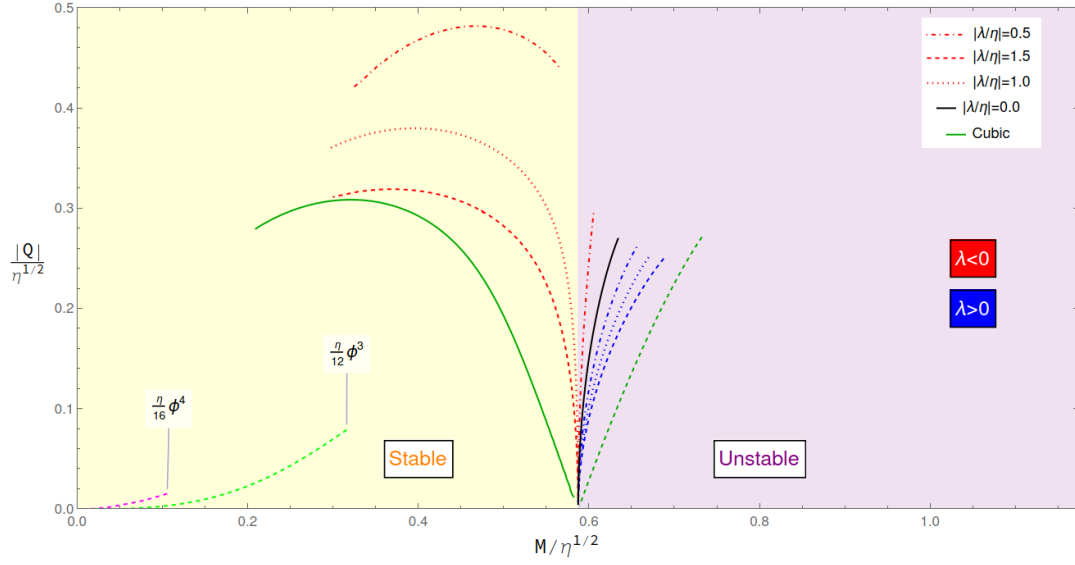


Figure 4.5: Scalar charge against Mass for all polynomial coupling functions considered up to this point. The light-yellow side labeled with "stable" is referred to the branches coming up from the bifurcation point; the purely ϕ^3 and ϕ^4 branches are unstable despite their location on the stable side in the plot. Dark-green branches refers to the solutions for coupling Eq. 4.5 with $|\frac{\lambda}{\eta}| = 1$: the dashed line in the unstable region has $\lambda = \eta$, while the straight line in the stable region has $\lambda = -\eta$.

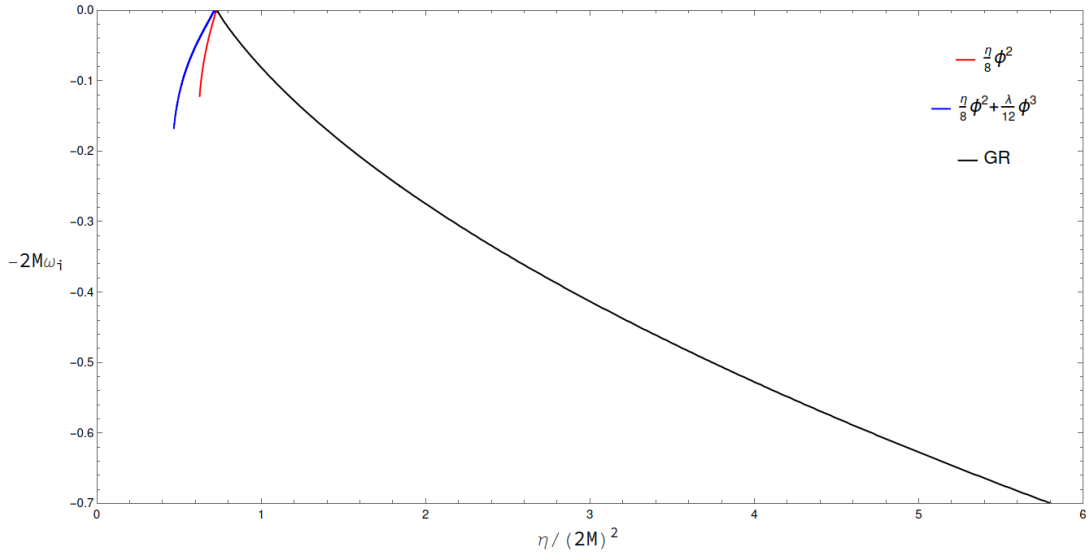


Figure 4.6: Dimensionless eigenfrequencies of the unstable modes $-2M\omega_I$ as a function of the normalized coupling constant η/M^2 for cubic+quadratic coupling (Eq. 4.7) with $\lambda = \eta$ (in blue) and for purely quadratic coupling (in red). In black the Schwarzschild solution's unstable modes, starting from \hat{M}_{bp} onward.

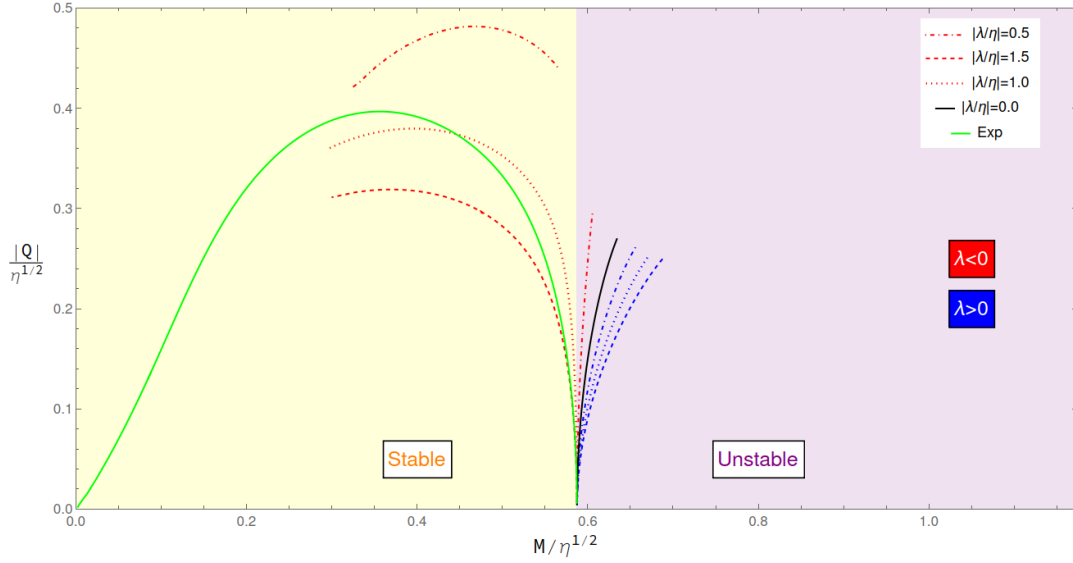


Figure 4.7: Same plot as in Fig. 3.16 where we added the fundamental branch of exponential coupling Eq. 4.10 with $\beta = 1.5$ in green. We appreciate how the curve related to the exponential coupling is coincident with the quartic one with $\lambda = -1.5\eta$ when $\hat{M} \rightarrow \hat{M}_{bp}$.

4.3 Exponential coupling function

Quartic term added to the qsGB coupling function is sufficient to yield stable BHs solutions. Still, the theory admits a minimum mass \hat{M}_{min} below which there are no stationary solutions of the field equations with the proper BCs, neither scalarized nor Schwarzschild-like. We could try to overcome this issue by adding other terms with growing powers of ϕ to the coupling function. However, in paper [15] it is demonstrated that a coupling function of the form

$$\mathcal{F}(\phi) = \frac{\eta}{8\beta} \left(1 - e^{-\beta\phi^2} \right) \quad (4.10)$$

is suitable for our purpose. Indeed, the authors show that the theory allows branches that are not restricted to low masses in the case of β values that satisfy

$$\beta > \beta_{crit} \approx 1.165625. \quad (4.11)$$

A particular case of this statement had already been examined in [9] for $\beta = 3/2$. Note that, within our notation, ϕ is defined differently from the scalar field in [15] by the factor $1/\sqrt{2}$ and by $1/2$ with respect to ϕ in [9].

Notably, the expansion of the coupling function Eq. 4.10 around $\phi = 0$ up to forth order is exactly coincident with the quartic coupling function Eq. 3.88 with $\lambda = -\beta\eta$. This is also evident when we compare the scalar charge \hat{Q} of scalarized solutions towards the bifurcation point \hat{M}_{bp} , where $\phi \rightarrow 0$, for the two couplings (Fig. 4.7). Thus, the exponential coupling can be regarded as an addition to the quartic coupling function of an infinite number of terms with increasing powers of ϕ , with a specific selection of coefficients, while ensuring that each term retains \mathbb{Z}_2 -symmetry.

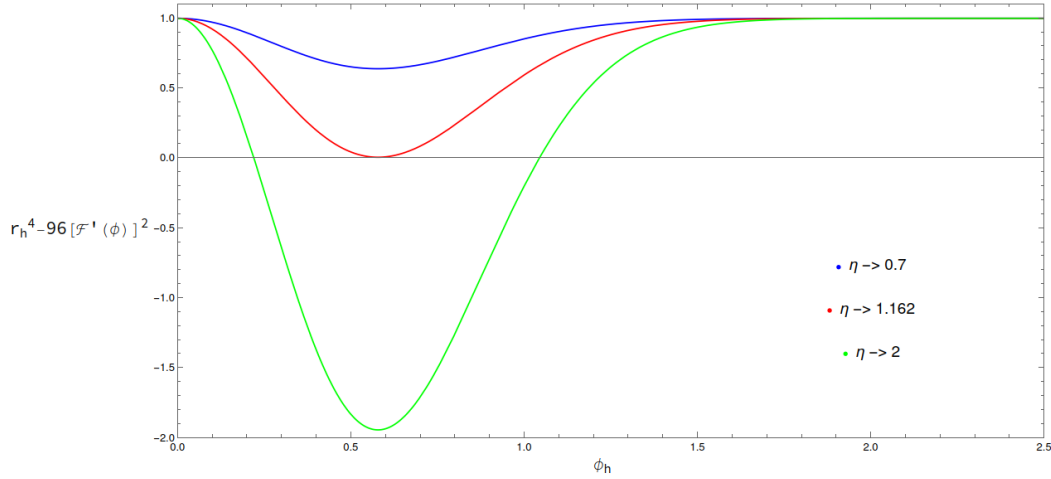


Figure 4.8: Regularity condition function f_{reg} (Eq. 3.89) for exponential coupling with fixed $\beta = 1.5$, and three different values of the coupling constant $\eta = 0.7, 1.162, 2$. The abscissa is the scalar field at the horizon ϕ_h .

4.3.1 Numerical results

We have computed the scalarized branches for different values of β in order to confirm the results shown in [15]. Moreover, in that paper, the authors do not address the stability of the solutions, which is what we intend to study to complete the examination.

For the scalarization analysis we should take care of the shape that the regularity function Eq. 3.89 reports when evaluated using the exponential coupling Eq. 4.10. In Fig. 4.8 we illustrate f_{reg} for three different values of η .

Similarly to quartic coupling function in Fig. 3.15, varying the coupling constant η , the regularity function f_{reg} (Eq. 3.89) can show different behaviors. For $\eta < \eta_{edge}$, where η_{edge} is referred to the value at which f_{reg} admits real zeros², is always positive. This means that we can search for scalarized solutions changing all positive $\phi_h \in \mathbb{R}^+$. Conversely, for $\eta > \eta_{edge}$ we get two real zeros that split into two distinct regions the interval where $f_{reg} > 0$, the suitable range for the choice of ϕ_{h_0} . However, differently from the quartic case (Fig. 3.15), the region after the second zero is not limited, as the function goes asymptotically to 1.

We also observe that the regularity condition function f_{reg} , for fixed value of the coupling constant η , varies with changes in β , as illustrated in Fig. 4.9. The smaller the β , the lower the function's absolute minimum is. For sufficiently small values of β , then, the minimum of f_{reg} will have a negative ordinate. As this parameter is further reduced, the function will become negative over larger intervals before approaching its asymptote at 1. This is the reason why the β_{crit} of paper [15] exists: the ϕ_h value that could yield scalarized solution for small β is excluded as it lies in the negative region of $f_{reg}(\phi_h)$.

In Fig. 4.10 we show the normalized scalar charge \hat{Q} of scalarized black holes branches as a function of \hat{M} for different values of the parameter β : three of them are greater than β_{crit} : they are $\beta = 1.5, 3, 6$. The forth one is $\beta = 1 < \beta_{crit}$. For the first three values, scalarized fun-

²The value of η_{edge} varies depending on the choice of the β parameter.

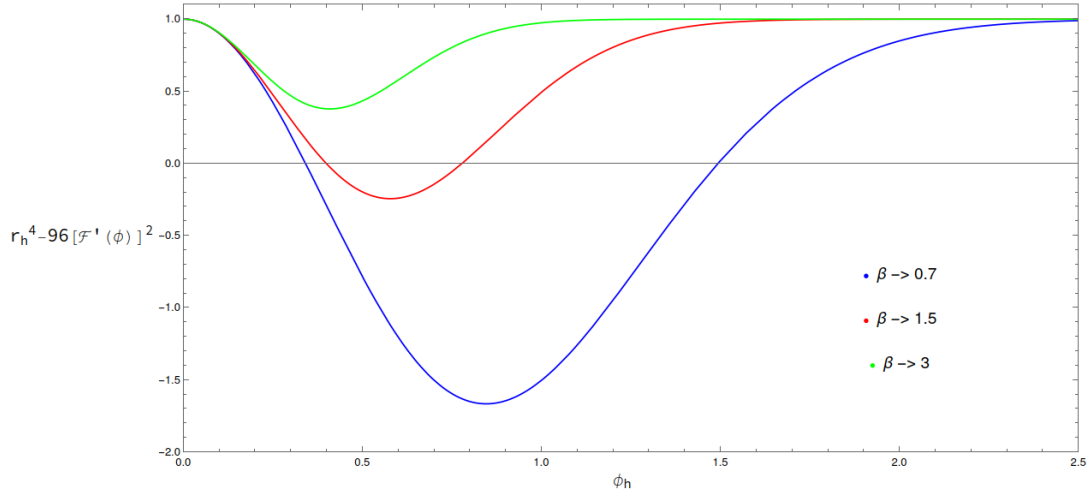


Figure 4.9: Regularity condition function f_{reg} (Eq. 3.89) as a function of ϕ_h for exponential coupling with fixed $\eta = 1.3$, and three different values of $\beta = 0.7, 1.5, 3$.

damental branches reaches infinitesimal masses $\hat{M} \rightarrow 0$; the related scalar charge decreases as the β parameter grows up. Conversely for the scalarized branch related to $\beta = 1$ we are not able to integrate the Eqs. 3.7,3.8 for values of the coupling constant η larger than $\eta = 0.9525$, which means for $\hat{M} < \hat{M}_{min} = 0.562431$.

In Fig. 4.11 we also display the branches of scalarized solutions characterized by one, two and three nodes, using the same β values that appear in Fig. 4.10. We see that the onset of each branch does not depend on β and the shape of the scalar charge \hat{Q} as a function of \hat{M} is not affected that much by changing the parameter, unlike the fundamental.

4.3.2 Stability of the solutions

In [9] the authors demonstrate that the fundamental branch of scalarized solutions for exponential coupling with $\beta = 1.5$ is stable from \hat{M}_{bp} down to a threshold mass value $\hat{M}_{thr} = 0.171$. We want to reproduce this result and also investigate whether it changes when we vary β parameter. Nevertheless, towards $\hat{M} \rightarrow \hat{M}_{thr}$, coming from below, the eigenfrequencies of the unstable modes diverge, as stated in [9]. The trend of the unstable modes $-\omega_I M^2 \eta^{1/2}$ as a function of \hat{M} is exhibited in Fig. 4.12, which reproduces the plot shown in [9], for $\beta = 3$. As the direct numerical integration for the search of unstable modes of scalarized BHs fails when approaching \hat{M}_{thr} , for the moment we will just chase for the maximum value of the normalized mass at which we are able to compute numerically the ω_I value. We will refer to that mass limit as \hat{M}_{lim} in order to distinguish from the proper threshold value for the onset of instability named as \hat{M}_{thr} . We should remember, then, that \hat{M}_{lim} represents an underestimation of \hat{M}_{thr} . Subsequently, we will refine the analysis by studying the behavior of the effective potential Eq. 3.45 in order to determine the actual \hat{M}_{thr} value.

Our analysis yield for $\beta = 1.5$ a value of $\hat{M}_{lim} = 0.152425$, which is, as expected, lower than the $\hat{M}_{thr} = 0.171$ found in [9]. In Tab. 4.1 we report the values of \hat{M}_{lim} for different values of $\beta = 1.5, 3, 6$, whose fundamental scalarized branch has been plotted in Fig. 4.10.

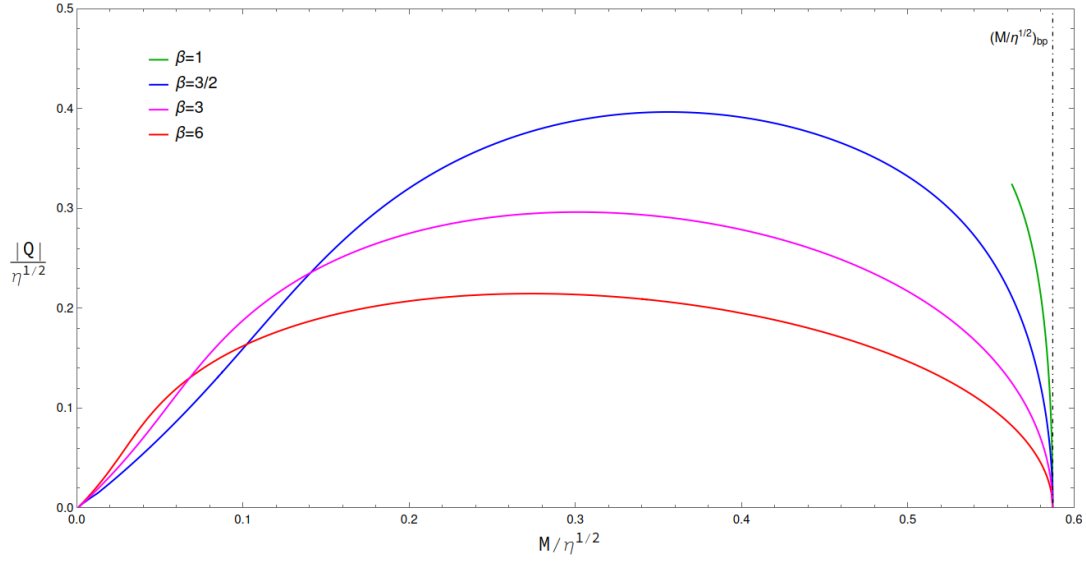


Figure 4.10: Normalized scalar charge \hat{Q} against normalized mass \hat{M} for exponential coupling function with different values of β parameter. The dot-dashed line represents the bifurcation point \hat{M}_{bp} , threshold value of the mass for the onset of stable scalarized solutions.

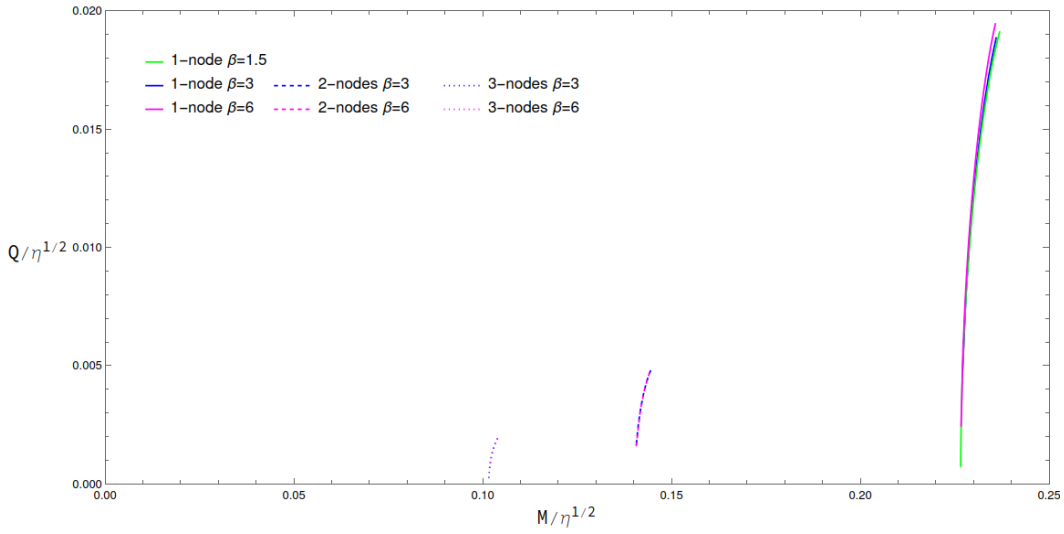


Figure 4.11: \hat{Q} as a function of \hat{M} for exponential coupling function with different values of β . Moving from the right side of the plot we encounter the 1-node, 2-nodes and 3-nodes branches.

β	\hat{M}_{lim}
1.5	0.152425
3	0.069286
6	0.035869

Table 4.1: Values of the normalized mass \hat{M}_{lim} below which the fundamental branch of scalarized solutions for exponential coupling is unstable for different values of β . \hat{M}_{lim} has been determined as the maximum value of \hat{M} for which we are able to numerically compute the eigenfrequencies of the unstable modes.

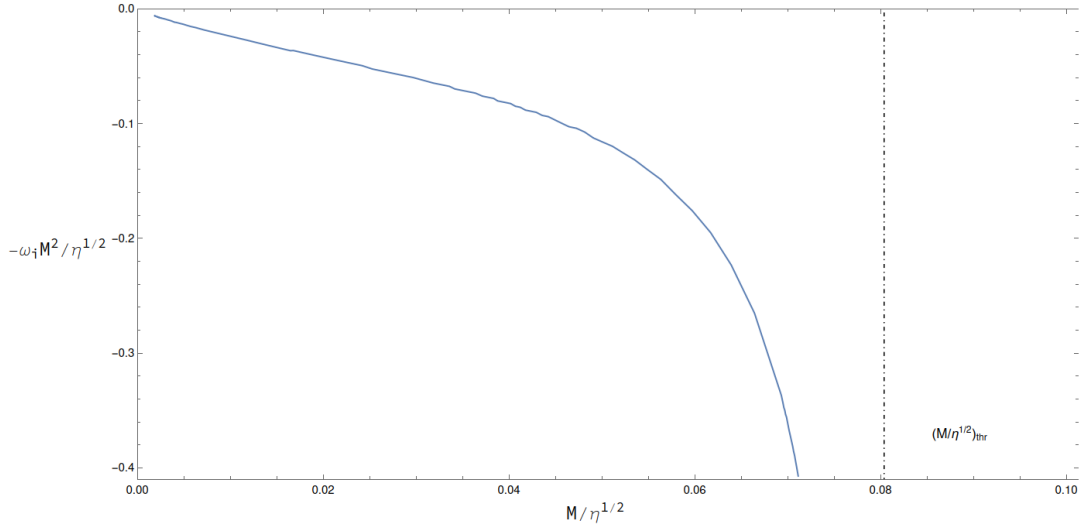


Figure 4.12: Dimensionless unstable eigenfrequencies $-\omega_I M^2 \eta^{1/2}$ as a function of the normalized mass \hat{M} for exponential coupling function with $\beta = 3$, as an example. The dot-dashed line represents the threshold mass value $\hat{M}_{thr} = 0.08033$, exposed in Tab. 4.2.

Our results are summarized in Fig. 4.13. Here we complete the representation of fundamental scalarized branches for exponential coupling shown in Fig. 4.10 with the depiction of instability. The dashed lines that refer to the unstable solutions are limited by the \hat{M}_{lim} value.

From Tab. 4.1 and from Fig. 4.13 we can conclude that by increasing the β parameter, the range of masses where scalarized solutions are stable is extended towards lower masses. In the next paragraph we will deal with the analysis of the effective potential in order to pursue a better understanding of the behavior of the width of stability range with respect to β .

4.3.3 Effective potential analysis

As discussed in Sec. 3.3.2, the stability of the scalarized solutions can be determined by the sign of the integral of the effective potential Eq. 3.45. Since we saw that the frequency of the unstable mode has an asymptote at $\hat{M} = \hat{M}_{thr}$, we can employ this method to search for the actual onset of instability \hat{M}_{thr} .

The expression for the Effective Potential given in Eq. 3.45 is not suitable for our purpose, because it needs the knowledge of the perturbation of the scalar field φ to be computed³. Thus, we should rewrite Eq. 3.45 just in terms of the coefficients of the perturbed equation Eq. 3.29, that depend only on the background fields.

We obtain

³The functions Z and f present in Eq. 3.45 can only be determined by knowing φ .

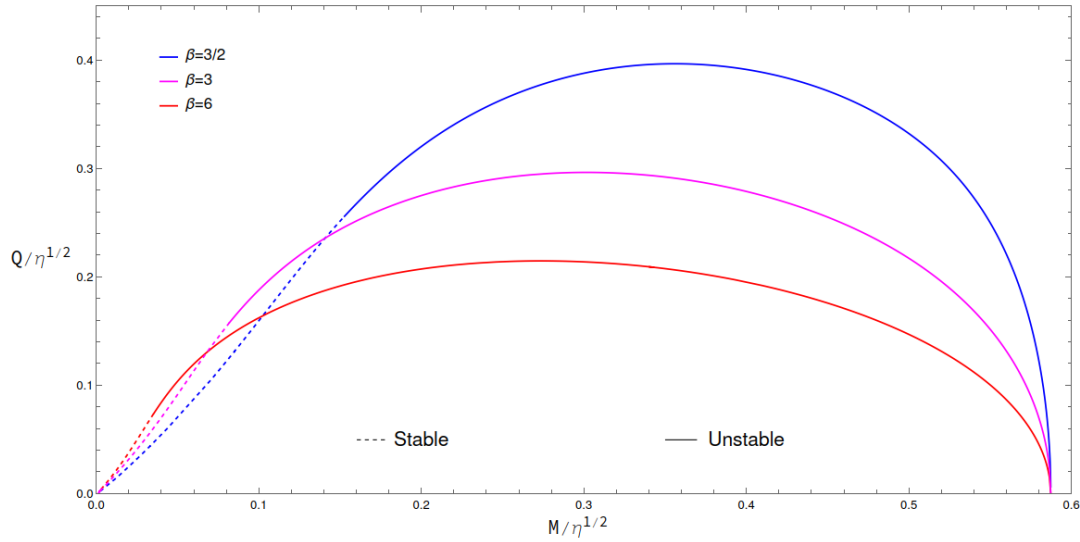


Figure 4.13: This Figure reports the same plot of Fig. 4.10, completed by the stability analysis. The dashed lines represent the unstable solutions while the straight lines the stable ones.

$$V_{eff} = \frac{1}{g^2} \left(U + \frac{k^2}{4} - \frac{k'}{2} - \frac{3}{4} \left(\frac{g'}{g} \right)^2 + \frac{g''}{2g} \right). \quad (4.12)$$

By plotting the effective potential for \hat{M} values lower than the \hat{M}_{lim} found through the frequency analysis, we noticed that it showed some divergences near the horizon. Hence, to understand this behavior, we examined the coefficients of the perturbed equation Eq. 3.29 in the region $\hat{M} < \hat{M}_{lim}$ and discovered that g^2 became negative. According to the zeros theorem, this indicates that g^2 inevitably vanishes at some point, causing the divergence of V_{eff} , as it appears in the denominator in Eq. 4.12.

Let us consider what this phenomenon implies. If $g^2 < 0$ then the tortoise coordinate of Eq. 3.42 is not well defined, since it is obtained by integrating g , which is now imaginary within a certain interval. Hence, if we cannot properly define the tortoise coordinate we cannot cast into a Schrödinger-like form the perturbed equation Eq. 3.29 either. This prevents us from using a QNM approach for the search of the unstable eigenfrequencies. Actually, the problem is even worse, because the whole theory becomes non radiative in the region $\hat{M} \in [0, \hat{M}_{thr}]$, as illustrated in the following paragraph.

Second order PDE The most general second order partial differential equation (PDE) can be written as

$$\left(a \frac{\partial^2}{\partial x^2} + b \frac{\partial^2}{\partial x \partial y} + c \frac{\partial^2}{\partial y^2} + d \frac{\partial}{\partial x} + e \frac{\partial}{\partial y} + f \right) \psi(x, y) = 0, \quad (4.13)$$

with the coefficients a, b, c, d, e, f depending on x and y . Depending on the value of the combination

$$\Delta = b^2 - 4ac \quad (4.14)$$

we can classify the PDE in three different types:

- if $\Delta > 0$ the PDE is **hyperbolic**;
- if $\Delta = 0$ the PDE is **parabolic**;
- if $\Delta < 0$ the PDE is **elliptic**.

The three types of PDEs have different properties and can be cast in canonical forms. The typical hyperbolic equation is the d'Alembert equation ($y = vt$)

$$\left(\frac{\partial^2}{\partial x^2} - \frac{1}{v^2} \frac{\partial^2}{\partial t^2} \right) \psi = 0, \quad (4.15)$$

that, defining new coordinates $\xi = x - vt$ and $\eta = x + vt$, can be written as

$$\partial_\xi \partial_\eta \psi = 0. \quad (4.16)$$

Eq. 4.16 is the *canonical form* of the hyperbolic PDE. Hence, we see that the general solution of Eq. 4.16 is

$$\psi(x, y) = f(x - vt) + g(x + vt), \quad (4.17)$$

which is the combination of two waves, propagating in opposite directions along x axis, with speed $|v|$.

On the other hand, elliptic PDEs are not radiative, with non-propagating solutions. An example is the Laplace equation

$$\nabla^2 \psi = \frac{\partial^2 \psi}{\partial x^2} + \frac{\partial^2 \psi}{\partial y^2} = 0. \quad (4.18)$$

whose general solutions are the *harmonic functions*. These represent a sort of "equilibrium" configuration of the function: no "forces" are felt.

In our case, referring to the perturbed Eq. 3.29, we can associate:

- $a \rightarrow g^2$;
- $c \rightarrow -1$;
- $b \rightarrow 0$;

with respect to the coefficients in Eq. 4.13.

The discriminant is $\Delta = 4g^2$. When g^2 is positive the equation is hyperbolic and we can search for wave solutions. On the contrary, the theory becomes elliptic when g^2 is negative in a certain region and the whole approach used thus far cannot be performed anymore. The solutions that we have found in the previous section should be interpreted as bare mathematical solutions of the perturbed equation with the boundary conditions Eq. 3.55, but their physical meaning should deserve a deeper understanding.

β	$\hat{M}_{thr}(\sigma)$
1.5	0.171(1)
2	0.119(5)
3	0.080(5)
4	0.063(1)
5	0.047(1)
6	0.039(1)
7	0.0332(1)
8	0.0290(1)
9	0.026(1)
10	0.022(1)
20	0.011(1)
30	0.008(1)
40	0.0056(5)
50	0.0045(5)
60	0.0038(3)
70	0.0032(1)
80	0.0028(1)
90	0.0025(1)
100	0.002(1)

Table 4.2: Values of the normalized mass \hat{M}_{thr} at which the perturbed equation Eq. 3.29 becomes elliptic for different values of β . The values in parentheses represent the uncertainties associated to the \hat{M}_{thr} .

4.3.4 Hyperbolicity Analysis

We study the onset of the ellipticity of the perturbed equation Eq. 3.29 by analyzing the sign of the discriminant $\Delta = 4g^2$. We try to figure out whether there is a link between the value of the β parameter and the threshold mass \hat{M}_{thr} below which the theory loses hyperbolicity. After computing the scalarized fundamental branches for different β values, we investigate the sign of the g^2 coefficient, naming the mass value of the solution that leads to a zero of g^2 as \hat{M}_{thr} . We also check that for all subsequent lower masses $\hat{M} < \hat{M}_{thr}$ function g^2 manifests a negative region.

In Tab. 4.2 we report the values of the threshold mass \hat{M}_{thr} for the onset of ellipticity for different values of β .

We can see that these values are slightly greater than the ones in Tab. 4.1 for the corresponding β values. They represent the upper limit that we wanted to find for the instability region. Nevertheless, we have actually discovered that for $\hat{M} < \hat{M}_{thr}$ a non-hyperbolic area for the theory arises, not an instability region.

Plotting the values of \hat{M}_{thr} of Tab. 4.2 as a function of β , we can observe that they are distributed roughly as $\propto 1/\beta$, as shown in Fig. 4.14.

We conduct a best-fit procedure with function

$$f_{fit}(\beta) = \frac{b}{\beta^k} \quad (4.19)$$

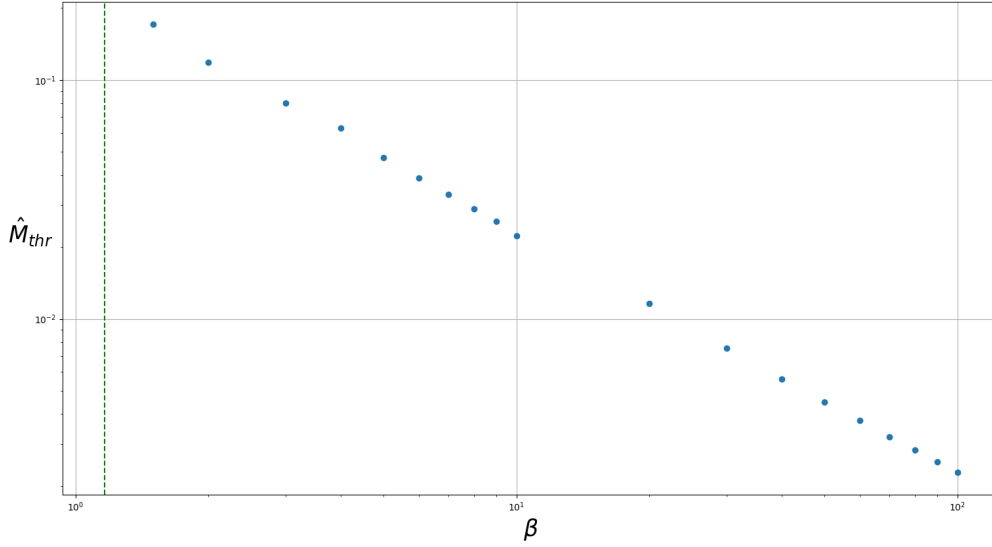


Figure 4.14: Logarithmic plot of the threshold mass \hat{M}_{thr} for the onset of ellipticity with respect to β . The vertical green dashed line represents the β_{crit} value.

to see the proper dependence.

For the uncertainties in the mass values, we proceed as follows. Initially, we consider the difference between the mass threshold \hat{M}_{thr} and the mass of the immediate preceding solution, where g^2 remains entirely positive. We infer that the actual threshold value lies within this range. Next, we account for the precision between two consecutive ϕ_{h_0} values used to generate solutions during the integration of the background fields. This precision is roughly 2-3 orders of magnitude larger than the previous difference and is considered as the uncertainty in the mass.

The result of the best-fit procedure is shown in Fig. 4.15.

We obtain the following results:

$$b = 0.248 \pm 0.005 \quad k = 1.032 \pm 0.009 \quad (4.20)$$

Actually we first tried to fit the data with a fixed power law $k = 1$ but we saw that the residuals were not distributed homogeneously around zero, so we decided to let the fit function free to vary also the power k . The power law is compatible with -1 within 4 standard deviations.

We have demonstrated that for growing values of β the threshold mass for the onset of ellipticity decreases down to infinitesimal values, i.e. $\hat{M}_{thr} \rightarrow 0$ as $\beta \rightarrow \infty$. Anyway for $\beta \rightarrow \infty$ the coupling function becomes trivial and we go back to GR-like equations of motion.

The theory is generally ill-defined in the low-mass regime and needs a further development to understand the nature of ellipticity in this context.

To conclude the analysis of the exponential coupling function, we also present the behavior of the maximum value of the normalized scalar charge \hat{Q}_{max} and its correspondent

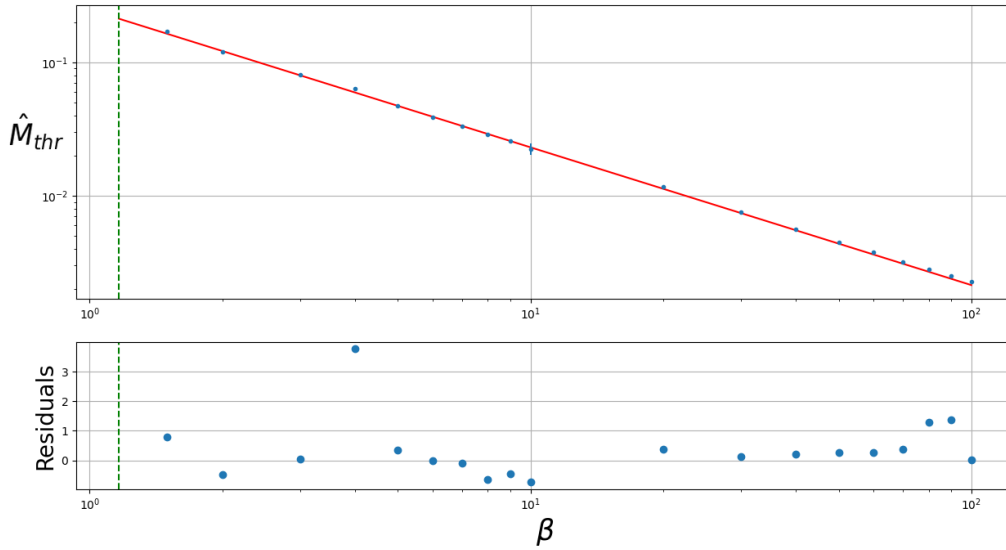


Figure 4.15: Best-fit line in red for the threshold mass \hat{M}_{thr} for the onset of ellipticity with respect to β parameter. In blue the data points. The graphic below shows the normalized residuals, namely $\frac{data-fit}{\sigma}$, where σ is the uncertainty in the mass.

normalized mass value \hat{M}_{max} with respect to β .

In Fig. 4.16 we see that \hat{Q}_{max} decreases as β grows with a behavior roughly proportional to a negative power law. A decreasing trend was expected, since the coupling function Eq. 4.10 tends to become trivial for large β values. The mass at which this maximum is reached decreases as well, but reaches a plateau for $\beta \geq 50$ and stabilizes around $\hat{M}_{max} \approx 0.22$.

4.4 Lorentzian coupling function

The last section of this chapter is aimed to determine the conditions for the onset of scalarized branches that can reach infinitesimal masses $\hat{M} \rightarrow 0$, standing to the left side⁴ of the bifurcation point. We should call these kind of branches *complete scalarized branches*. Let us summarize the information that we have collected thus far.

Conditions for complete branches

Firstly, we have seen that polynomial coupling functions are not yielding complete branches, since they are limited towards low masses (see Fig. 4.5). This is due to the fact that the regularity function Eq. 3.89, which has to be positive for the regularity condition Eq. 3.22 to be fulfilled, from a certain value of ϕ_h on is monotonically decreasing, as illustrated in Fig. 3.15 for example. This behavior impose a restriction on the choice of the value of the scalar field at the horizon that could bring scalarization. Conversely, for coupling functions like the

⁴Referring to \hat{Q}/\hat{M} plot.

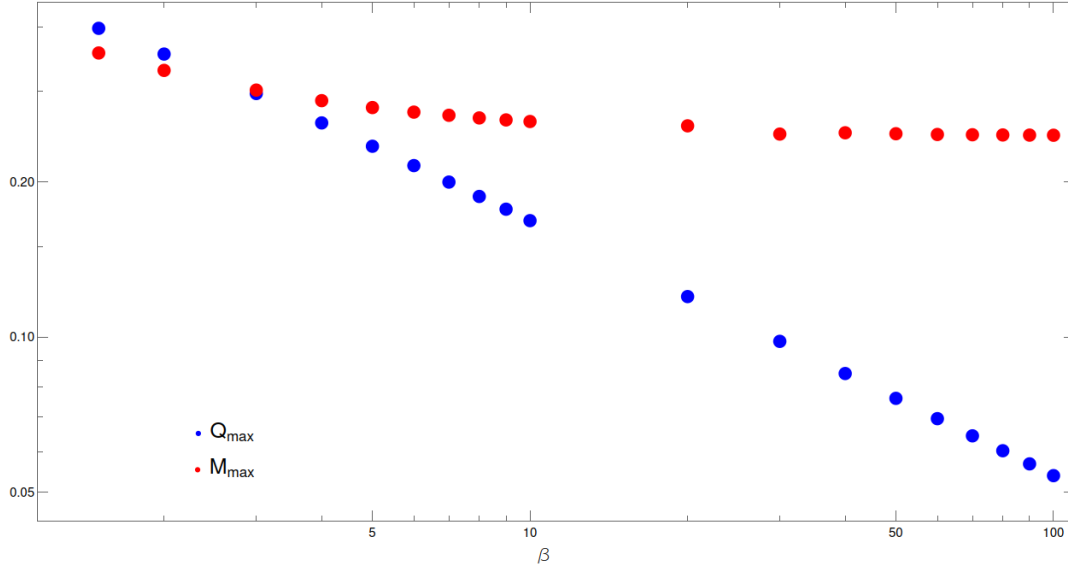


Figure 4.16: Logarithmic plot of the maximum value of the normalized scalar charge \hat{Q}_{max} (blue points) and its correspondent normalized mass \hat{M}_{max} (red points) for the exponential coupling as functions of β .

exponential one (Eq. 4.10), f_{reg} manifests a horizontal asymptote at 1, meaning that regularity condition is satisfied for all ϕ_h towards infinity. This feature provides more flexibility in selecting the scalar field at the horizon.

The difference between these types of couplings lies in their functional forms. Specifically, the exponential coupling exhibits a vanishing first derivative as $\phi_h \rightarrow \infty$, whereas polynomial couplings do not.

Another request that we have to impose is that our theory must admit a bifurcation point, that establishes the mass value below which Schwarzschild solution is not stable. This is crucial for the manifestation of stable scalarized solutions in the region where unstable GR ones stand. The quadratic term of qsGB does yield a bifurcation point, whereas the quartic and cubic one does not (see Sec. 4.1 and Sec. 4.2). The difference among these couplings is that the first derivative of the latter nullifies when evaluated in $\phi_0 = 0$, the value of the scalar field for which Schwarzschild solution can arise. This prevents to find a range of values for the coupling constant that could make the integral of the effective potential negative, guaranteeing unstable modes (see Eq. 4.3 as an example). Thus if we consider couplings whose expansion around $\phi = 0$ involves the quadratic term, the bifurcation point will be set exactly at \hat{M}_{bp} of quadratic theory.

Lastly, we have shown in Sec. 3.3.2 that negative values of the coupling constants of terms of order greater than the second one in the expansion may lead to stable branches. This is true unless the theory becomes ill-defined below some threshold mass \hat{M}_{thr} as shown Sec. 4.3 for exponential case.

We summarize the requests that we have just exposed for the coupling function \mathcal{F} as:

$$\lim_{\phi_h \rightarrow \infty} \mathcal{F}'(\phi_h) = 0 \quad (4.21)$$

$$\mathcal{F}(\phi) = \frac{\eta}{8}\phi^2 + \frac{\lambda}{16}\phi^4 + O(\phi^6) \quad (4.22)$$

$$\lambda < 0. \quad (4.23)$$

Moreover, \mathcal{F} may include a parameter β that can be modified in order to change the behavior of the regularity function f_{reg} and let arise the complete branch.

These conditions should be considered in conjunction with those outlined in Section 3.2 to determine the onset of spontaneous scalarization, when exploring other coupling scenarios.

Lorentzian function

The so-called Lorentzian function in Eq. 4.24 matches all the features that we demand

$$\mathcal{F}(\phi) = \frac{\eta}{8}\beta^2 \left(1 - \frac{\beta^2}{\phi^2 + \beta^2} \right). \quad (4.24)$$

Here β plays the same role of the β parameter of the exponential case Eq. 4.10, as said above. The expansion of the function Eq. 4.24 around $\phi = 0$ up to the forth order is

$$\mathcal{F}(\phi) = \frac{\eta\phi^2}{8} - \frac{\eta\phi^4}{8\beta^2} + O(\phi^6) \quad (4.25)$$

and its first derivative is

$$\mathcal{F}'(\phi) = \frac{x\beta^4\eta}{4(x^2 + \beta^2)^2} \quad (4.26)$$

So the first derivative vanishes both at $\phi = 0$ and for $\phi \rightarrow \infty$. The second derivative for $\eta > 0$ is positive, as demanded by condition 2 in Sec. 3.2. Moreover, the coupling function in Eq. 4.24 admits the quadratic term in the expansion and the quartic one, with negative contribution for $\eta > 0$ and has infinite even power terms.

Therefore, we can perform the same analysis conducted for the exponential coupling function in Sec. 4.3. We compute the scalarized branches for different values of β and we study the stability of the solutions. In Figs. 4.17 and 4.18 the results are illustrated.

As for the exponential case, β needs to satisfy a condition for the complete branch to manifest, and we observe that decreasing its value we could extend the range of masses where scalarized solutions arise. We thought that the critical value was around $\beta_{crit} = 0.05$ since for $\beta < \beta_{crit}$ we could reach infinitesimal masses as we can appreciate from Fig. 4.18.

Nevertheless, continuing to integrate down to even lower masses for Lorentzian coupling we always find a threshold value below which the integration fails. This behavior differs from

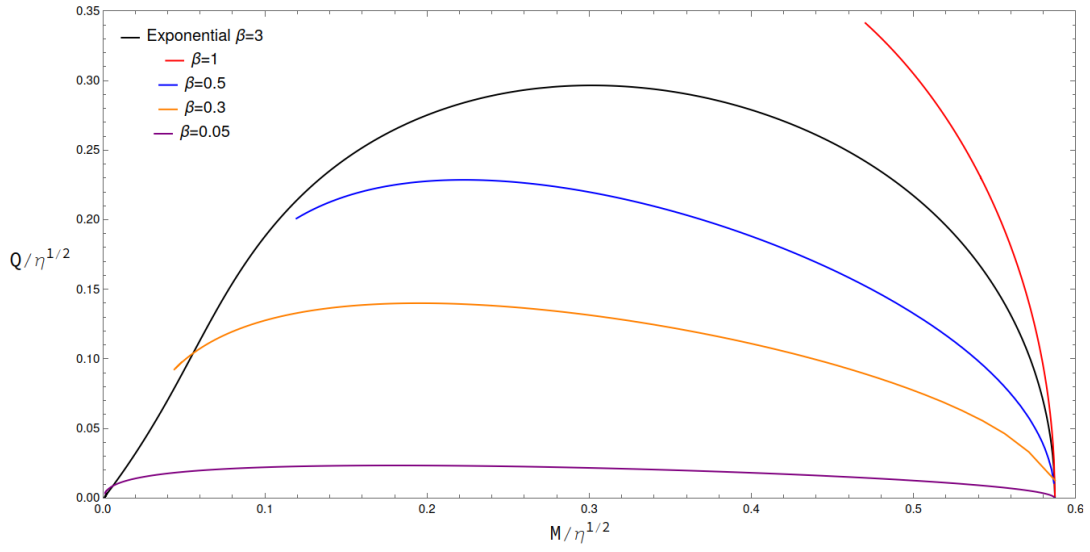


Figure 4.17: \hat{Q} - \hat{M} plot for Lorentzian coupling function with different values of β . The curve in Black is referred to the exponential coupling with $\beta = 3$, as a comparison with the Lorentzian case.

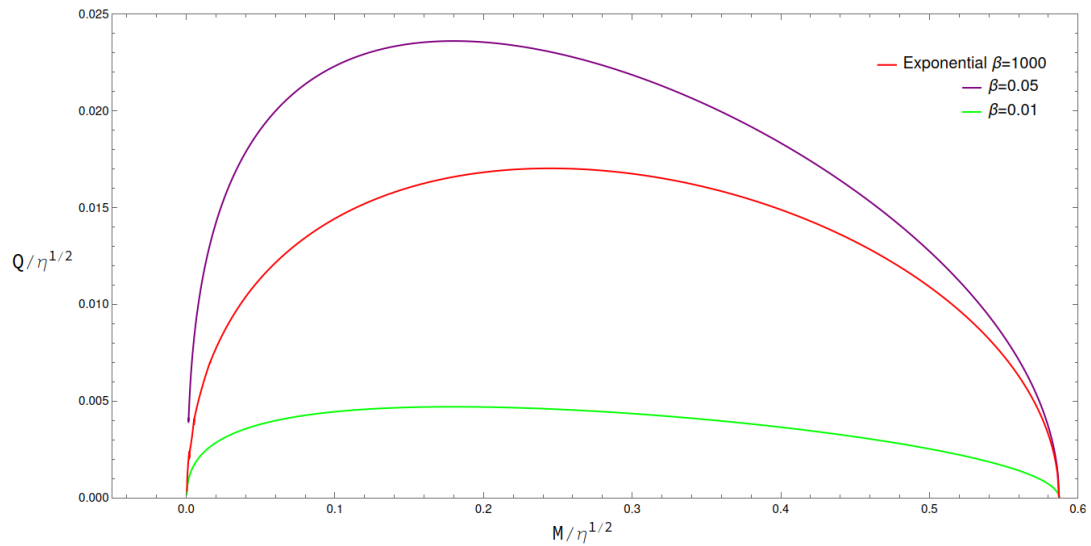


Figure 4.18: \hat{Q} - \hat{M} for the Lorentzian coupling function, with lower values of β with respect to Fig. 4.17

the exponential case, where we manage to find scalarized solutions no matter how large the constant coupling (how low the mass) is, given that $\beta > \beta_{crit}$ (Eq. 4.11). This is not due to numerical issues though, but to the fact that the regularity condition Eq. 3.22 restricts the choice of the scalar field at the horizon. Indeed, analyzing the regularity function Eq. 3.89 we see that increasing η value, both the suitable ϕ_h value that induces scalarization as well as the position of the second zero of f_{reg} increase in turn. The problem is that there is a certain value (for each β) of the coupling constant η (and consequently a certain mass) where the proper ϕ_h stands in the negative region of function f_{reg} , effectively terminating the branch of scalarized solutions.

The difference between the exponential and the Lorentzian coupling functions is that the first derivative of the former goes to 0 more rapidly than the latter's one. For example, if we fix the β of the Lorentzian coupling to $\beta_{lor} = 0.05$ and the exponential one to $\beta_{exp} = 800$, we see that the expansions towards $\phi \rightarrow 0$ up to forth order is the same:

$$\mathcal{F}_{lor}(\phi) = \frac{\eta}{8}\phi^2 - 50\eta\phi^4 + 20000\eta\phi^6 + O(\phi^8) \quad (4.27)$$

$$\mathcal{F}_{exp}(\phi) = \frac{\eta}{8}\phi^2 - 50\eta\phi^4 + \frac{40000}{3}\eta\phi^6 + O(\phi^8) \quad (4.28)$$

Computing the limit for $\phi \rightarrow \infty$ of the ratio between the first derivatives of exponential coupling (Eq. 4.10) and of lorentzian coupling (Eq. 4.24) we get

$$\lim_{\phi \rightarrow \infty} \frac{\mathcal{F}'_{exp}(\phi)}{\mathcal{F}'_{lor}(\phi)} = \frac{e^{-\beta_{exp}\phi^2} \times (\phi^2 + \beta^2)^2}{\beta_{lor}^4} = 0 \quad (4.29)$$

as expected.

Therefore, one last condition that we can add for a complete scalarized branch to arise is that the first derivative of the coupling function should go to zero for $\phi \rightarrow \infty$ at least as fast as the Gaussian one.

Chapter 5

Conclusions

In this thesis, we have investigated scalar-Gauss-Bonnet gravity, delving into the phenomenon of spontaneous black hole scalarization. After validating existing results in the literature to verify the reliability of algorithms designed for searching scalarized solutions and conducting stability analyses under radial perturbations, we advanced our research by considering alternative coupling functions. Here, we summarize the original results obtained.

Firstly, generalizing the exponential coupling function used in [14] with the coupling function in Eq. 4.10, we analyzed the stability of scalarized solutions for different values of the β parameter. This was aimed to complete the work of [15]. In that paper, the authors only studied the phenomenology of scalarized solutions, claiming that scalarized branch can reach infinitesimal normalized masses in the \hat{Q}/\hat{M} plot for $\beta > \beta_{crit}$ (Eq. 4.11). We have shown that the range of masses where scalarized solutions are stable is extended towards lower masses as β is increased. Nevertheless, those ranges are bounded by a mass limit \hat{M}_{thr} below which the theory becomes ill-posed. In this regime, the effective potential diverges near the horizon and the Eq. (3.29) for the perturbation of the scalar field becomes elliptic. We have shown that \hat{M}_{thr} decreases for growing β values, and we have found a power low dependence of the threshold mass for the onset of ellipticity with respect to β roughly described by $\hat{M}_{thr} \propto 1/\beta$.

The theory seems to be ill-defined in the low-mass/high-curvature regime, and further developments are needed to understand the nature of ellipticity in this context. For example in [5] the authors demonstrate how an additional coupling of the scalar field to the scalar curvature R in the action can somehow interfere with the extension of the ellipticity region.

Secondly, we showed how the quadratic term is of mandatory presence in the expansion of the coupling function for $\phi \rightarrow 0$ in order to manifest a non trivial *bifurcation point* \hat{M}_{bp} . This is crucial for the onset of at least one branch of stable scalarized solutions, that arise in the region where $\hat{M} < \hat{M}_{bp}$. Indeed, considering only quartic power term for the coupling function in Eq. 4.1, Schwarzschild solutions is stable for all mass values, moving the fictitious bifurcation point to $\hat{M}_{bp} \rightarrow 0$. Scalarized solutions do arise even for such a coupling, but only in unstable states.

The same behavior is expected for the cubic coupling function in Eq. 4.5. In both cases, not only the integral of the effective potential with Schwarzschild background is positive no matter the value of the coupling constant (Eqs. 4.3, 4.6), but we were also not able to find any unstable frequency through direct numerical investigation. These results justify our conclusions.

Cubic coupling function Eq. 4.5 does not satisfy the \mathbb{Z}_2 -symmetry that is usually assumed in literature. However, it is only sufficient that the coupling function has a stationary point for some finite value of the scalar field (condition Eq. 3.9) to guarantee the existence of GR solutions, as spontaneous scalarization mechanism requires. Motivated by the fact that pure cubic coupling did admit a scalarized branch (Fig. 4.3), even if unstable, we added a quadratic term to $\mathcal{F}(\phi)$ as in Eq. 4.7 and search for scalarized solutions. The phenomenology obtained is similar to the one of quadratic+quartic coupling (Eq. 3.88), with stable branches arising in the left side of \hat{M}_{bp} for sufficiently negative values of λ . On the contrary, when $\lambda > 0$ only unstable scalarized solutions occur (see Fig. 4.5). In both regions, branches are still limited by a minimum mass due to the restrictions imposed by the regularity condition Eq. 3.22.

Lastly, our intent is to determine all the features that a coupling function must present to yield a *complete scalarized branches*, i.e. branches that can reach infinitesimal masses with non trivial scalar charged solutions. We saw how polynomial couplings with finite number of terms in power of ϕ produce truncated branches. On the contrary exponential function Eq. 4.10, whose expansion for $\phi \rightarrow 0$ has infinite terms, for sufficiently big β can reach $\hat{M} \rightarrow 0$ with scalarized solutions. We suppose that this happens for those couplings whose first derivative vanishes for $\phi_h \rightarrow \infty$, preventing the regularity condition function f_{reg} to bring limitations on the choice of the scalar field at the horizon. We also want the \hat{M}_{bp} to be present at finite value, therefore the expansion of the coupling function must include the quadratic term. The quartic term must have negative coefficient to provide stable solutions. After considering all the above points, we examine the lorentzian coupling function Eq. 4.24 that satisfies all the conditions we have just exposed. We have shown that for $\beta < \beta_{crit} = 0.05$ scalarized solutions can reach infinitesimal masses. However, for lower masses the regularity condition restricts the choice of the scalar field at the horizon, effectively terminating the branch of scalarized solutions. We conclude that an additional condition for the onset of complete branches is that the first derivative of the coupling function should go to zero for $\phi \rightarrow \infty$ at least as fast as the Gaussian function.

These were the original findings of the thesis.

Now, we can connect our numerical results and phenomenological predictions of sGB gravity with experimental observations. Subsequently, we offer some suggestions for potential future developments of this work.

Constraints for the coupling constant

As stated in [9], empirical observations may give us some hints on the possible values of the coupling constants.

The minimum mass of a black hole observed in X-ray binaries¹ can be estimated to be around $M \sim 5M_\odot$. For example, in A0620-00 [12] a $6.6M_\odot$ BH has been observed; for the black hole candidate MAXI J1659-152 [23] the object's mass is estimated to be between $4.7 - 7.8M_\odot$. Taking the exponential coupling with a given β , e.g. $\beta = 3$, we demonstrated that its threshold mass below which no physical BH solutions are admitted, is $\hat{M}_{thr} \simeq 0.080$. The minimum

¹X-ray binaries are a class of binary systems that are luminous in X-rays. Those are emitted by matter falling from one component, called the donor (a normal star or a neutron star), to the other component, called the accretor.

admitted mass of the theory should consequently be smaller than the one observed, then

$$M_{thr} = \eta^{1/2} \times 0.080 < 5M_{\odot} \quad (5.1)$$

$$\eta^{1/2} < \frac{5M_{\odot}}{0.080} = 62.5M_{\odot}. \quad (5.2)$$

On the other hand we know that Gravitational Waves sources analyzed by the LIGO-Virgo collaboration are compatible with GR predictions, within the uncertainties. From spontaneous scalarization mechanism, with a quadratic term in the expansion of the coupling function, we saw that Schwarzschild solution is not stable for $\hat{M} < \hat{M}_{bp} = 0.58697$. Stable scalarized solutions arise for lower values of \hat{M}_{bp} . They also should occur for lower masses with respect to the ones empirically in accordance with General Relativity. Thus, taking $M = 5M_{\odot}$ as the confidence mass for GR solutions, we can state that

$$\hat{M}_{scal} < \hat{M}_{bp} \leq \frac{5M_{\odot}}{\eta^{1/2}} \quad (5.3)$$

$$\eta^{1/2} \leq \frac{5M_{\odot}}{0.58697} = 8.5M_{\odot}. \quad (5.4)$$

Actually GW observations managed to identify objects with masses lower than $3M_{\odot}$, as in GW190814 merger whose one of the two objects involved has $M = 2.6M_{\odot}$ [1]. However, we are not sure whether it is a BH or another object since we are in the "mass gap" region, a range of masses apparently too light for a black hole and too heavy for a neutron star. Anyway, assuming that it is indeed a BH, then we should verify if the merger signal is in accordance with GR within the accuracy of the measurements.

Future developments

Gravitational Waves Phenomenology

Future observations will provide us with more precise data such that we will be able to refine the constraints on the coupling constants [10]. However, we should also take into account the possibility that small mass BHs, even the ones observed thus far that we assumed to be Schwarzschild-like, may be scalarized. Indeed they could eventually carry scalar charge which is not sufficiently strong to bring visible effects for the precision of measures available at the moment².

Then, what are the main differences that we expect to observe experimentally between scalarized and GR black holes?

The main channel that should highlight the presence of scalarized BHs is represented by Gravitational Waves phenomenology. We have not introduced the theory of gravitational waves in this work, so we will give a brief overview in the Appendix B.

²For instance towards the bifurcation point on the left side of \hat{Q}/\hat{M} plot

In the case of a binary system, the scalar charge of the BHs will induce a scalar dipole moment, that will be radiated in the form of scalar waves. These waves will be emitted in addition to the tensorial ones associated to the GWs. This yields an increase in the orbital angular velocity of the binary and causes a dephasing in the gravitational waveform when compared to GR [37]. Moreover, the energy loss of the system will be greater than the one predicted by GR. Indeed, there is not only the gravitational wave luminosity L_{GW} that needs to be compensated as in Eq. B.6, but two additional contributions. These are brought [37] by the stress-energy tensor associated to the scalar field ($T_{\mu\nu}$) and the one caused by the coupling of the scalar field with the GB invariant ($\mathcal{K}_{\mu\nu}$), that have appeared in Eq. 3.4.

To be ready to test GR against scalar-Gauss-Bonnet theory with spontaneous scalarization as the new generation of interferometer will be operative as Einstein Telescope and LISA, we should develop the study of the phenomenology of GW emitted by scalarized BH. An analysis has already been performed in [4] for the quadratic+quartic case, showing that the frequency-mode of oscillation increases with respect to the GR case. The analysis should be extended to exponential coupling in the future to see also the behavior towards low masses and for different β values.

Further phenomenological analysis

In order to address the issue of the non-hyperbolicity of scalarized solutions in the low mass limit for exponential coupling, some interesting suggestions has been made. For instance, in [5] the authors propose to add a coupling of the scalar field to the scalar curvature R in the action. This only affects the characteristic of solutions, not directly the equations of motion, as it does not yield scalarization on its own.

Other terms in the action could be added to the scalar-Gauss-Bonnet theory to improve the stability of the theory in the low-mass regime and to fix the ellipticity problem. This can also be intended as potential terms for the scalar field or higher order curvature invariants, through an EFT approach.

Moreover, the phenomenon of loss of hyperbolicity has been widely discussed in the context of numerical relativity simulations of BH mergers in GB gravity, where the formation of elliptic region of spacetime can occur [29].

In conclusion, the mechanism of spontaneous scalarization in scalar-Gauss-Bonnet gravity is very promising within the context of modified gravity theories, and it is worth to be further investigated. It can lead to empirically testable predictions and it can provide a new insight into the nature of black holes and gravity itself, while maintaining the compatibility with the observations made so far.

References

- [1] URL: <https://www.virgo-gw.eu/science/gw-universe/catalog-of-gravitational-wave-events/>.
- [2] Tim Adamo and Ezra T Newman. “The Kerr-Newman metric: a review”. In: *arXiv preprint arXiv:1410.6626* (2014). URL: <https://arxiv.org/abs/1410.6626>.
- [3] G Antoniou, A Bakopoulos, and P Kanti. “Evasion of no-hair theorems and novel black-hole solutions in Gauss-Bonnet theories”. In: *Physical review letters* 120.13 (2018), p. 131102. URL: <https://journals.aps.org/prl/abstract/10.1103/PhysRevLett.120.131102>.
- [4] Georgios Antoniou, Caio FB Macedo, Andrea Maselli, and Thomas P Sotiriou. “Axial perturbations of hairy black holes in generalised scalar-tensor theories”. In: *arXiv preprint arXiv:2404.02479* (2024). URL: <https://arxiv.org/abs/2404.02479>.
- [5] Georgios Antoniou, Caio FB Macedo, Ryan McManus, and Thomas P Sotiriou. “Stable spontaneously-scalarized black holes in generalized scalar-tensor theories”. In: *Physical Review D* 106.2 (2022), p. 024029. URL: <https://journals.aps.org/prd/abstract/10.1103/PhysRevD.106.024029>.
- [6] Matthew Bailes, Beverly K Berger, PR Brady, M Branchesi, Karsten Danzmann, M Evans, Kelly Holley-Bockelmann, BR Iyer, T Kajita, S Katsanevas, et al. “Gravitational-wave physics and astronomy in the 2020s and 2030s”. In: *Nature Reviews Physics* 3.5 (2021), pp. 344–366. URL: <https://www.nature.com/articles/s42254-021-00306-7>.
- [7] Carlo Bernardini, Orlando Ragnisco, Paolo Maria Santini, et al. *Metodi matematici della fisica*. Carocci, 1993.
- [8] Emanuele Berti, Enrico Barausse, Vitor Cardoso, Leonardo Gualtieri, Paolo Pani, Ulrich Sperhake, Leo C Stein, Norbert Wex, Kent Yagi, Tessa Baker, et al. “Testing general relativity with present and future astrophysical observations”. In: *Classical and Quantum Gravity* 32.24 (2015), p. 243001. URL: <https://iopscience.iop.org/article/10.1088/0264-9381/32/24/243001>.
- [9] Jose Luis Blázquez-Salcedo, Daniela D Doneva, Jutta Kunz, and Stoytcho S Yazadjiev. “Radial perturbations of the scalarized Einstein-Gauss-Bonnet black holes”. In: *Physical Review D* 98.8 (2018), p. 084011. URL: <https://journals.aps.org/prd/abstract/10.1103/PhysRevD.98.084011>.
- [10] Jose Luis Blázquez-Salcedo, Caio FB Macedo, Vitor Cardoso, Valeria Ferrari, Leonardo Gualtieri, Fei Chen Khoo, Jutta Kunz, and Paolo Pani. “Perturbed black holes in Einstein-dilaton-Gauss-Bonnet gravity: Stability, ringdown, and gravitational-wave emission”. In: *Physical Review D* 94.10 (2016), p. 104024. URL: <https://journals.aps.org/prd/abstract/10.1103/PhysRevD.94.104024>.

- [11] Walter F Buell and BA Shadwick. “Potentials and bound states”. In: *American Journal of Physics* 63.3 (1995), pp. 256–258. URL: <https://aapt.scitation.org/doi/10.1119/1.17845>.
- [12] Andrew G Cantrell, Charles D Bailyn, Jerome A Orosz, Jeffrey E McClintock, Ronald A Remillard, Cynthia S Froning, Joseph Neilsen, Dawn M Gelino, and Lijun Gou. “THE INCLINATION OF THE SOFT X-RAY TRANSIENT A0620- 00 AND THE MASS OF ITS BLACK HOLE”. In: *The Astrophysical Journal* 710.2 (2010), p. 1127. URL: <https://iopscience.iop.org/article/10.1088/0004-637X/710/2/1127>.
- [13] Brandon Carter. “Axisymmetric black hole has only two degrees of freedom”. In: *Physical Review Letters* 26.6 (1971), p. 331. URL: <https://journals.aps.org/prl/abstract/10.1103/PhysRevLett.26.331>.
- [14] Daniela D Doneva and Stoytcho S Yazadjiev. “New Gauss-Bonnet black holes with curvature-induced scalarization in extended scalar-tensor theories”. In: *Physical review letters* 120.13 (2018), p. 131103. URL: <https://journals.aps.org/prl/abstract/10.1103/PhysRevLett.120.131103>.
- [15] Pedro GS Fernandes, David J Mulryne, and Jorge FM Delgado. “Exploring the small mass limit of stationary black holes in theories with Gauss–Bonnet terms”. In: *Classical and Quantum Gravity* 39.23 (2022), p. 235015. URL: <https://iopscience.iop.org/article/10.1088/1361-6382/aca010/meta>.
- [16] Valeria Ferrari, Leonardo Gualtieri, and Paolo Pani. *General relativity and its applications: black holes, compact stars and gravitational waves*. CRC press, 2020. URL: <https://www.taylorfrancis.com/books/mono/10.1201/9780429491405/general-relativity-applications-valeria-ferrari-leonardo-gualtieri-paolo-pani>.
- [17] Gary W Gibbons and Stephen W Hawking. “Action integrals and partition functions in quantum gravity”. In: *Physical Review D* 15.10 (1977), p. 2752. URL: <https://journals.aps.org/prd/abstract/10.1103/PhysRevD.15.2752>.
- [18] David J Gross and John H Sloan. “The quartic effective action for the heterotic string”. In: *Nuclear Physics B* 291 (1987), pp. 41–89. URL: <https://www.sciencedirect.com/science/article/pii/0550321387902692>.
- [19] Stephen W Hawking and George FR Ellis. *The large scale structure of space-time*. Cambridge university press, 2023. URL: <https://www.cambridge.org/9780521099066>.
- [20] Panagiota Kanti, NE Mavromatos, J Rizos, Kyriakos Tamvakis, and E Winstanley. “Dilatonic black holes in higher curvature string gravity. II. Linear stability”. In: *Physical Review D* 57.10 (1998), p. 6255. URL: <https://journals.aps.org/prd/abstract/10.1103/PhysRevD.57.6255>.
- [21] Panagiota Kanti, Nick E Mavromatos, John Rizos, Kyriakos Tamvakis, and Elizabeth Winstanley. “Dilatonic black holes in higher curvature string gravity”. In: *Physical Review D* 54.8 (1996), p. 5049. URL: <https://journals.aps.org/prd/abstract/10.1103/PhysRevD.54.5049>.
- [22] Caio FB Macedo, Jeremy Sakstein, Emanuele Berti, Leonardo Gualtieri, Hector O Silva, and Thomas P Sotiriou. “Self-interactions and spontaneous black hole scalarization”. In: *Physical Review D* 99.10 (2019), p. 104041. URL: <https://journals.aps.org/prd/abstract/10.1103/PhysRevD.99.104041>.

- [23] Aslam Ali Molla, Dipak Debnath, Sandip K Chakrabarti, Santanu Mondal, and Arghajit Jana. “Estimation of the mass of the black hole candidate MAXI J1659- 152 using TCAF and POS models”. In: *Monthly Notices of the Royal Astronomical Society* 460.3 (2016), pp. 3163–3169. URL: <https://academic.oup.com/mnras/article/460/3/3163/2609479>.
- [24] Filipe Moura and Ricardo Schiappa. “Higher-derivative-corrected black holes: perturbative stability and absorption cross section in heterotic string theory”. In: *Classical and Quantum Gravity* 24.2 (2006), p. 361. URL: <https://iopscience.iop.org/article/10.1088/0264-9381/24/2/006/meta>.
- [25] Attilio Palatini. “Deduzione invariante delle equazioni gravitazionali dal principio di Hamilton”. In: *Rendiconti del Circolo Matematico di Palermo (1884-1940)* 43.1 (1919), pp. 203–212. URL: <https://link.springer.com/article/10.1007/BF03014898>.
- [26] Paolo Pani and Vitor Cardoso. “Are black holes in alternative theories serious astrophysical candidates? The Case for Einstein-Dilaton-Gauss-Bonnet black holes”. In: *Physical Review D* 79.8 (2009), p. 084031. URL: <https://journals.aps.org/prd/abstract/10.1103/PhysRevD.79.084031>.
- [27] Eric Poisson. *A relativist’s toolkit: the mathematics of black-hole mechanics*. Cambridge university press, 2004. URL: <https://www.cambridge.org/9780521830916>.
- [28] CAC Quinzacara and Patricio Salgado. “Black hole for the Einstein-Chern-Simons gravity”. In: *Physical Review D* 85.12 (2012), p. 124026. URL: <https://journals.aps.org/prd/abstract/10.1103/PhysRevD.85.124026>.
- [29] Abhishek Hegade K. R, Justin L. Ripley, and Nicolás Yunes. “Where and why does Einstein-scalar-Gauss-Bonnet theory break down?” In: *Phys. Rev. D* 107.4 (2023), p. 044044. DOI: 10.1103/PhysRevD.107.044044. arXiv: 2211.08477 [gr-qc]. URL: <https://journals.aps.org/prd/abstract/10.1103/PhysRevD.107.044044>.
- [30] Hector O Silva, Caio FB Macedo, Thomas P Sotiriou, Leonardo Gualtieri, Jeremy Sakstein, and Emanuele Berti. “Stability of scalarized black hole solutions in scalar-Gauss-Bonnet gravity”. In: *Physical Review D* 99.6 (2019), p. 064011. URL: <https://journals.aps.org/prd/abstract/10.1103/PhysRevD.99.064011>.
- [31] Hector O Silva, Jeremy Sakstein, Leonardo Gualtieri, Thomas P Sotiriou, and Emanuele Berti. “Spontaneous scalarization of black holes and compact stars from a Gauss-Bonnet coupling”. In: *Physical review letters* 120.13 (2018), p. 131104. URL: <https://journals.aps.org/prl/abstract/10.1103/PhysRevLett.120.131104>.
- [32] Thomas P Sotiriou and Shuang-Yong Zhou. “Black hole hair in generalized scalar-tensor gravity”. In: *Physical Review Letters* 112.25 (2014), p. 251102. URL: <https://journals.aps.org/prl/abstract/10.1103/PhysRevLett.112.251102>.
- [33] Thomas P Sotiriou and Shuang-Yong Zhou. “Black hole hair in generalized scalar-tensor gravity: An explicit example”. In: *Physical Review D* 90.12 (2014), p. 124063. URL: <https://journals.aps.org/prd/abstract/10.1103/PhysRevD.90.124063>.
- [34] Kellogg S Stelle. “Renormalization of higher-derivative quantum gravity”. In: *Physical Review D* 16.4 (1977), p. 953. URL: <https://journals.aps.org/prd/abstract/10.1103/PhysRevD.16.953>.
- [35] Takashi Torii and Kei-ichi Maeda. “Stability of a dilatonic black hole with a Gauss-Bonnet term”. In: *Physical Review D* 58.8 (1998), p. 084004. URL: <https://journals.aps.org/prd/abstract/10.1103/PhysRevD.58.084004>.

- [36] Norbert Wex and Michael Kramer. “Gravity tests with radio pulsars”. In: *Universe* 6.9 (2020), p. 156. URL: <https://www.mdpi.com/2218-1997/6/9/156>.
- [37] Helvi Witek, Leonardo Gualtieri, Paolo Pani, and Thomas P Sotiriou. “Black holes and binary mergers in scalar Gauss-Bonnet gravity: scalar field dynamics”. In: *Physical Review D* 99.6 (2019), p. 064035. URL: <https://journals.aps.org/prd/abstract/10.1103/PhysRevD.99.064035>.
- [38] Richard Woodard. “Avoiding dark energy with $1/r$ modifications of gravity”. In: *The invisible universe: Dark matter and dark energy*. Springer, 2007, pp. 403–433. URL: https://link.springer.com/chapter/10.1007/978-3-540-68025-4_17.
- [39] Frank J Zerilli. “Gravitational field of a particle falling in a Schwarzschild geometry analyzed in tensor harmonics”. In: *Physical Review D* 2.10 (1970), p. 2141. URL: <https://journals.aps.org/prd/abstract/10.1103/PhysRevD.2.2141>.

Appendix

A Perturbed equation

Here we give the expression for sake of completeness of the coefficients written in Eq. 3.29. First of all, following Salcedo-Doneva notation [9], we recall here $A(r) = e^{2\varphi(r)}$ and $B(r) = e^{2\Lambda(r)}$.

The first coefficient g^2 , which is involved in the definition of the tortoise coordinate for sGB gravity, can be written as

$$g^2 = \frac{g_{up}}{g_{down}} \quad (\text{A.1})$$

with g_{up} and g_{down} given by

$$\begin{aligned} g_{up} = & -8e^{6\Lambda}\phi'_0 r^3 \frac{d\mathcal{F}}{d\phi_0} + e^{8\Lambda}r^4 + 16\phi_0'^2 \left(e^{2\Lambda} - 1\right)^2 e^{2\Lambda} \left(\frac{d\mathcal{F}}{d\phi_0}\right)^2 \frac{d^2\mathcal{F}}{d\phi_0^2} \\ & - 16\left(e^{2\Lambda} - 1\right) \left(e^{2\Lambda}\Lambda'\phi'_0 - e^{2\Lambda}\phi_0'' + 3\Lambda'\phi'_0 + \phi_0''\right) e^{2\Lambda} \left(\frac{d\mathcal{F}}{d\phi_0}\right)^3 \\ & - 4e^{4\Lambda} \left(e^{4\Lambda} - 4e^{2\Lambda}\Lambda'r - 4\phi_0'^2 r^2 - 2e^{2\Lambda} + 4\Lambda'r + 1\right) \left(\frac{d\mathcal{F}}{d\phi_0}\right)^2, \\ g_{down} = & -8e^{4\Lambda+2\varphi}\phi'_0 r^3 \frac{d\mathcal{F}}{d\phi_0} + e^{6\Lambda+2\varphi}r^4 + 16e^{2\varphi}\varphi'\phi'_0 \left(e^{4\Lambda} + 2e^{2\Lambda} - 3\right) \left(\frac{d\mathcal{F}}{d\phi_0}\right)^3 \\ & - 4e^{2\varphi+2\Lambda} \left(-4\phi_0'^2 r^2 + 4e^{2\Lambda}\varphi'r + e^{4\Lambda} - 4\varphi'r - 2e^{2\Lambda} + 1\right) \left(\frac{d\mathcal{F}}{d\phi_0}\right)^2. \end{aligned}$$

Then coefficient $k(r)$ can be expressed as

$$k(r) = \frac{C_2}{C_4} \quad (\text{A.2})$$

with

$$\begin{aligned}
C_4 = & \left[2 \frac{d\mathcal{F}}{d\phi_0} \phi_0' (e^{2\Lambda} - 3) + e^{2\Lambda} r \right] \times \left[-8 \frac{d\mathcal{F}}{d\phi_0} e^{4\Lambda} \phi_0' r^3 + e^{6\Lambda} r^4 + 16 \phi_0' \phi_0' (e^{2\Lambda} - 1) (e^{2\Lambda} + 3) \left(\frac{d\mathcal{F}}{d\phi_0} \right)^3 \right. \\
& \left. - 4e^{2\Lambda} (4\phi_0' e^{2\Lambda} r + e^{4\Lambda} - 4\phi_0'^2 r^2 - 4\phi_0' r - 2e^{2\Lambda} + 1) \left(\frac{d\mathcal{F}}{d\phi_0} \right)^2 \right] \\
C_2 = & \frac{d^2 \mathcal{F}}{d\phi_0^2} \left[4\phi_0'^2 r^4 (e^{8\Lambda} - e^{6\Lambda}) + 32\phi_0' \phi_0'^3 (15e^{4\Lambda} - 7e^{2\Lambda} - 5e^{6\Lambda} - 3) \left(\frac{d\mathcal{F}}{d\phi_0} \right)^3 \right. \\
& - 8\phi_0'^2 e^{2\Lambda} (8e^{4\Lambda} \phi_0' r + 8e^{2\Lambda} \phi_0' r - 16\phi_0' r + 9e^{4\Lambda} - 9e^{2\Lambda} - 3e^{6\Lambda} + 3) \left(\frac{d\mathcal{F}}{d\phi_0} \right)^2 \\
& + 4\phi_0' r e^{4\Lambda} (e^{4\Lambda} \phi_0'^2 r^2 - 6e^{2\Lambda} \phi_0'^2 r^2 + 5\phi_0'^2 r^2 + 8e^{2\Lambda} \phi_0' r + 2e^{4\Lambda} - 8\phi_0' r - 4e^{2\Lambda} + 2) \frac{d\mathcal{F}}{d\phi_0} \Big] \\
& + 32\phi_0' \left(\frac{d\mathcal{F}}{d\phi_0} \right)^4 \left[-7e^{4\Lambda} \phi_0'^2 \phi_0' - 11e^{4\Lambda} \phi_0' \Lambda' \phi_0' + 15e^{2\Lambda} \phi_0'^2 \phi_0' - 9e^{2\Lambda} \phi_0' \Lambda' \phi_0' + \phi_0'^2 \phi_0' e^{6\Lambda} \right. \\
& + 9\phi_0' \Lambda' \phi_0' e^{6\Lambda} + e^{4\Lambda} \phi_0'' \phi_0' + 13e^{4\Lambda} \phi_0' \phi_0'' + 9e^{2\Lambda} \phi_0'' \phi_0' - 25e^{2\Lambda} \phi_0' \phi_0'' - \phi_0'' \phi_0' e^{6\Lambda} \\
& \left. - 9\phi_0'^2 \phi_0' + 27\phi_0' \Lambda' \phi_0' - 3\phi_0' \phi_0'' e^{6\Lambda} - 9\phi_0'' \phi_0' + 15\phi_0' \phi_0'' \right] \\
& + 8e^{2\Lambda} \left(\frac{d\mathcal{F}}{d\phi_0} \right)^3 \left[6\Lambda' \phi_0' + 18\phi_0'' \phi_0' r + 6\phi_0' \phi_0'^3 r^2 - 6\Lambda' \phi_0'^3 r^2 + 12\phi_0'^2 \phi_0' r \right. \\
& + 40e^{2\Lambda} \phi_0' \Lambda' \phi_0' r + 3\phi_0'' + e^{4\Lambda} \phi_0'' + \phi_0'' e^{6\Lambda} - 5e^{2\Lambda} \phi_0'' + 24\phi_0'^3 r - 6e^{4\Lambda} \phi_0' \phi_0'^3 r^2 - 2e^{4\Lambda} \Lambda' \phi_0'^3 r^2 \\
& + 8e^{2\Lambda} \phi_0' \phi_0'^3 r^2 + 16e^{2\Lambda} \Lambda' \phi_0'^3 r^2 + 4e^{4\Lambda} \phi_0'^2 \phi_0' r - 16e^{2\Lambda} \phi_0'^2 \phi_0' r + 2e^{4\Lambda} \phi_0'' \phi_0' r - 12e^{4\Lambda} \phi_0' \phi_0'' r \\
& - 20e^{2\Lambda} \phi_0'' \phi_0' r + 32e^{2\Lambda} \phi_0' \phi_0'' r - 6\phi_0' \phi_0' - 8e^{2\Lambda} \phi_0'^3 r - 2e^{4\Lambda} \phi_0' \phi_0' + 6e^{2\Lambda} \phi_0' \phi_0' + 2\phi_0' \phi_0' e^{6\Lambda} \\
& \left. - 20\phi_0' \phi_0'' r - 72\phi_0' \Lambda' \phi_0' r - 6\Lambda' \phi_0' e^{6\Lambda} + 10e^{4\Lambda} \Lambda' \phi_0' - 10e^{2\Lambda} \Lambda' \phi_0' \right] \\
& + 4e^{4\Lambda} \left(\frac{d\mathcal{F}}{d\phi_0} \right)^2 \left[-1 - 4\Lambda' r - 34\phi_0'^2 r^2 + 6\phi_0' r + 26\phi_0' \Lambda' r^2 - 13\phi_0' \phi_0'^2 r^3 \right. \\
& - 2\phi_0'^2 r^2 - 4\phi_0'' r^2 + e^{4\Lambda} \phi_0' \phi_0'^2 r^3 - e^{4\Lambda} \Lambda' \phi_0'^2 r^3 + e^{4\Lambda} \phi_0' \phi_0'' r^3 - 4e^{2\Lambda} \Lambda' \phi_0'^2 r^3 - 6e^{2\Lambda} \phi_0' \phi_0'' r^3 \\
& + 5\phi_0' \phi_0'' r^3 + \Lambda' \phi_0'^2 r^3 + e^{4\Lambda} + e^{2\Lambda} + 8e^{2\Lambda} \phi_0'^2 r^2 + 4e^{2\Lambda} \Lambda' r + 2e^{4\Lambda} \phi_0'^2 r^2 + 2e^{2\Lambda} \phi_0'^2 r^2 \\
& \left. - 18e^{2\Lambda} \phi_0' \Lambda' r^2 - e^{6\Lambda} + 4e^{2\Lambda} \phi_0'' r^2 + 2e^{4\Lambda} \phi_0' r - 8e^{2\Lambda} \phi_0' r \right] - e^{8\Lambda} r^4 [-\Lambda' r + \phi_0' r + 2] \\
& - 2r^3 e^{6\Lambda} \frac{d\mathcal{F}}{d\phi_0} \left[e^{4\Lambda} \phi_0' - 2e^{2\Lambda} \phi_0'' r - 6\phi_0' \phi_0' r + 2\Lambda' \phi_0' r + 2e^{2\Lambda} \phi_0' + 2\phi_0'' r - 15\phi_0' \right]
\end{aligned}$$

In the end, the function $U(r)$ that is related to the effective potential (see Sec. 3.3.1) is written like

$$U(r) = \frac{C_3}{C_4} \quad (\text{A.3})$$

with

$$C_3 = D_0 + D_2 + D_4 + D_6 + D_8 \quad (\text{A.4})$$

and

$$\begin{aligned}
D_0 &= -\phi'_0 r^5 e^{8\Lambda} (-2\varphi' \phi'_0 r + 2\Lambda' \phi'_0 + e^{2\Lambda} \phi'_0 - 3\phi''_0 r - 5\phi'_0) \\
D_2 &= -2r^3 e^{6\Lambda} \left[e^{2\Lambda} \phi_0'^4 r^2 - 3\phi_0'^4 r^2 - 2e^{2\Lambda} \varphi' \phi_0'^2 r + 2e^{2\Lambda} \Lambda' \phi_0'^2 r - 3e^{2\Lambda} \phi_0' \phi_0'' r + 4\varphi' \phi_0'^2 r \right. \\
&\quad - 4\Lambda' \phi_0'^2 r + e^{4\Lambda} \phi_0'^2 - e^{2\Lambda} \varphi'^2 + e^{2\Lambda} \varphi' \Lambda' - 4e^{2\Lambda} \phi_0'^2 + 3\phi_0' \phi_0'' r - e^{2\Lambda} \varphi'' + \varphi'^2 \\
&\quad \left. - 3\varphi' \Lambda' + 3\phi_0'^2 + \varphi'' \right] \left(\frac{d^2 \mathcal{F}}{d\phi_0^2} \right) + 2r^4 e^{6\Lambda} \phi_0'^3 (e^{2\Lambda} - 1) \left(\frac{d^3 \mathcal{F}}{d\phi_0^3} \right) \\
&\quad + 2r^2 e^{6\Lambda} \left[10e^{2\Lambda} \phi_0'^3 r^2 + 4\Lambda' \phi_0'^3 r^3 - 4\varphi' \phi_0'^3 r^3 - 12\phi_0'^2 \phi_0'' r^3 + 4\varphi' \phi_0'' r^2 + 3\varphi' \phi_0' r \right. \\
&\quad + 2\Lambda' \phi_0' r - 30\phi_0'^3 r^2 - e^{4\Lambda} \phi_0' + 2e^{2\Lambda} \phi_0' - \phi_0'' r + e^{2\Lambda} \phi_0'' r + 4\varphi'^2 \phi_0' r^2 + 3\varphi'' \phi_0' r^2 \\
&\quad + 2e^{2\Lambda} \varphi' \Lambda' \phi_0' r^2 - \phi_0' - 2e^{2\Lambda} \varphi' \phi_0'' r^2 - 2e^{2\Lambda} \varphi' \phi_0' r - 14\varphi' \Lambda' \phi_0' r^2 + e^{4\Lambda} \varphi' \phi_0' r \\
&\quad \left. + 2e^{2\Lambda} \varphi' \phi_0'^3 r^3 - 2e^{2\Lambda} \Lambda' \phi_0'^3 r^3 + 2e^{2\Lambda} \phi_0'^2 \phi_0'' r^3 - 2e^{2\Lambda} \varphi'^2 \phi_0' r^2 - e^{2\Lambda} \varphi'' \phi_0' r^2 \right] \left(\frac{d\mathcal{F}}{d\phi_0} \right), \\
D_4 &= -4\phi_0'^4 r^3 (e^{8\Lambda} - 4e^{6\Lambda} + 3e^{4\Lambda}) \left(\frac{d^2 \mathcal{F}}{d\phi_0^2} \right)^2 \\
&\quad + \left[-8e^{8\Lambda} \varphi' \Lambda' \phi_0' r^2 - 16e^{6\Lambda} \varphi' \Lambda' \phi_0' r^2 + 8e^{4\Lambda} \varphi' \Lambda' \phi_0' r^2 - 8\phi_0'' e^{6\Lambda} r + 4e^{8\Lambda} \phi_0'' r \right. \\
&\quad - 24e^{4\Lambda} \phi_0'^5 r^4 - 4e^{4\Lambda} \phi_0' + 4e^{8\Lambda} \phi_0' + 4\phi_0' e^{6\Lambda} - 4\phi_0' e^{10\Lambda} + 4e^{4\Lambda} \phi_0'' r + 36e^{8\Lambda} \phi_0'^3 r^2 \\
&\quad - 104e^{6\Lambda} \phi_0'^3 r^2 + 68e^{4\Lambda} \phi_0'^3 r^2 + 8e^{6\Lambda} \phi_0'^5 r^4 - 56e^{4\Lambda} \Lambda' \phi_0'^3 r^3 + 8e^{8\Lambda} \phi_0'^2 \phi_0'' r^3 \\
&\quad - 56e^{6\Lambda} \phi_0'^2 \phi_0'' r^3 + 48e^{4\Lambda} \phi_0'^2 \phi_0'' r^3 + 8e^{8\Lambda} \varphi'^2 \phi_0' r^2 - 32e^{6\Lambda} \varphi'^2 \phi_0' r^2 + 24e^{4\Lambda} \varphi'^2 \phi_0' r^2 \\
&\quad + 8e^{8\Lambda} \varphi'' \phi_0' r^2 - 24e^{6\Lambda} \varphi'' \phi_0' r^2 + 16e^{6\Lambda} \varphi' \phi_0'' r^2 + 16e^{4\Lambda} \varphi'' \phi_0' r^2 - 16e^{4\Lambda} \varphi' \phi_0'' r^2 + 8e^{8\Lambda} \varphi' \phi_0' r \\
&\quad - 16e^{4\Lambda} \Lambda' \phi_0' r - 8e^{8\Lambda} \Lambda' \phi_0'^3 r^3 - 88e^{6\Lambda} \varphi' \phi_0'^3 r^3 + 32e^{6\Lambda} \Lambda' \phi_0'^3 r^3 + 124e^{4\Lambda} \varphi' \phi_0'^3 r^3 \\
&\quad \left. - 32\varphi' \phi_0' e^{6\Lambda} r + 16\Lambda' \phi_0' e^{6\Lambda} r + 12e^{8\Lambda} \varphi' \phi_0'^3 r^3 + 24e^{4\Lambda} \varphi' \phi_0' r \right] \left(\frac{d\mathcal{F}}{d\phi_0} \right) \left(\frac{d^2 \mathcal{F}}{d\phi_0^2} \right) \\
&\quad + 4\phi_0'^2 r \left[-6\phi_0'^2 e^{6\Lambda} r^2 + e^{8\Lambda} \phi_0'^2 r^2 + 5e^{4\Lambda} \phi_0'^2 r^2 + 4\varphi' e^{6\Lambda} r - 4e^{4\Lambda} \varphi' r - 2e^{6\Lambda} + e^{8\Lambda} \right. \\
&\quad \left. + e^{4\Lambda} \right] \left(\frac{d\mathcal{F}}{d\phi_0} \right) \left(\frac{d^3 \mathcal{F}}{d\phi_0^3} \right) + \left[8e^{8\Lambda} \varphi' \Lambda' \phi_0'^2 r^3 + 8e^{6\Lambda} \varphi' \Lambda' \phi_0'^2 r^3 + 80e^{4\Lambda} \varphi' \Lambda' \phi_0'^2 r^3 \right. \\
&\quad - 4e^{8\Lambda} \varphi' \phi_0' \phi_0'' r^3 - 16e^{6\Lambda} \varphi' \phi_0' \phi_0'' r^3 + 4e^{4\Lambda} \varphi' \phi_0' \phi_0'' r^3 + 4e^{4\Lambda} \varphi' + 24e^{4\Lambda} \phi_0'^2 r \\
&\quad + 24e^{6\Lambda} \varphi'^2 r + 168e^{4\Lambda} \phi_0'^4 r^3 + 4e^{10\Lambda} \varphi' - 4e^{8\Lambda} \varphi' - 4e^{6\Lambda} \varphi' + 8e^{8\Lambda} \phi_0'^4 r^3 - 32e^{6\Lambda} \phi_0'^2 r \\
&\quad - 8e^{8\Lambda} \varphi'^2 r + 8e^{6\Lambda} \varphi'' r - 4e^{8\Lambda} \varphi'' r - 8e^{6\Lambda} \varphi'^3 r^2 - 16e^{4\Lambda} \varphi'^2 r + 8e^{4\Lambda} \varphi'^3 r^2 \\
&\quad - 4e^{4\Lambda} \varphi'' r - 80e^{6\Lambda} \phi_0'^4 r^3 + 8e^{8\Lambda} \phi_0'^2 r - 16e^{6\Lambda} \varphi' \phi_0'^4 r^4 + 16e^{6\Lambda} \Lambda' \phi_0'^4 r^4 - 16e^{6\Lambda} \phi_0'^3 \phi_0'' r^4 \\
&\quad + 48e^{4\Lambda} \phi_0'^3 \phi_0'' r^4 - 8e^{8\Lambda} \varphi'^2 \phi_0'^2 r^3 + 16e^{6\Lambda} \varphi'^2 \phi_0'^2 r^3 - 40e^{4\Lambda} \varphi'^2 \phi_0'^2 r^3 - 4e^{8\Lambda} \varphi'' \phi_0'^2 r^3 \\
&\quad + 16e^{6\Lambda} \varphi'' \phi_0'^2 r^3 - 44e^{4\Lambda} \varphi'' \phi_0'^2 r^3 - 24e^{8\Lambda} \varphi' \phi_0'^2 r^2 - 24e^{8\Lambda} \Lambda' \phi_0'^2 r^2 + 40e^{6\Lambda} \varphi'^2 \Lambda' r^2 \\
&\quad + 104e^{6\Lambda} \varphi' \phi_0'^2 r^2 + 8e^{6\Lambda} \Lambda' \phi_0'^2 r^2 - 56e^{4\Lambda} \varphi'^2 \Lambda' r^2 - 128e^{4\Lambda} \varphi' \phi_0'^2 r^2 + 8e^{8\Lambda} \phi_0' \phi_0'' r^2 \\
&\quad \left. - 16e^{6\Lambda} \varphi'' \varphi' r^2 - 8e^{6\Lambda} \phi_0' \phi_0'' r^2 + 16e^{4\Lambda} \varphi'' \varphi' r^2 - 16e^{6\Lambda} \varphi' \Lambda' r + 16e^{4\Lambda} \varphi' \Lambda' r \right] \left(\frac{d\mathcal{F}}{d\phi_0} \right)^2
\end{aligned}$$

$$\begin{aligned}
D_6 = & 8e^{2\Lambda}\phi_0'^3 \left[2e^{4\Lambda}\phi_0'^2 r^2 - 8e^{2\Lambda}\phi_0'^2 r^2 + 6\phi_0'^2 r^2 - 12e^{4\Lambda}\phi_0' r + 32e^{2\Lambda}\phi_0' r - 20\phi_0' r \right. \\
& + e^{6\Lambda} + e^{4\Lambda} - 5e^{2\Lambda} + 3 \left. \right] \left(\frac{d\mathcal{F}}{d\phi_0} \right) \left(\frac{d^2\mathcal{F}}{d\phi_0^2} \right)^2 + 8e^{2\Lambda}\phi_0' \left[-9\phi_0'\phi_0'' + 2e^{2\Lambda}\phi_0'' \right. \\
& - 4e^{4\Lambda}\phi_0'' + 10e^{4\Lambda}\Lambda'\phi_0' + \phi_0'\phi_0''e^{6\Lambda} - 6\Lambda'\phi_0'e^{6\Lambda} - e^{6\Lambda}\phi_0'\Lambda'\phi_0' r + 13e^{4\Lambda}\phi_0'\Lambda'\phi_0' r \\
& - 11e^{2\Lambda}\phi_0'\Lambda'\phi_0' r + 12\Lambda'\phi_0'^3 r^2 - 2\phi_0'\phi_0'' r - 18e^{4\Lambda}\phi_0'^3 r + 2e^{6\Lambda}\phi_0'^3 r - 30\phi_0'^3 r \\
& + 6\Lambda'\phi_0' - 4e^{4\Lambda}\phi_0'^2\phi_0'' r^2 + 16e^{2\Lambda}\phi_0'^2\phi_0'' r^2 - 10e^{4\Lambda}\phi_0'\phi_0'^3 r^2 + 4e^{4\Lambda}\Lambda'\phi_0'^3 r^2 \\
& + 24e^{2\Lambda}\phi_0'\phi_0'^3 r^2 - 8e^{2\Lambda}\Lambda'\phi_0'^3 r^2 + 3e^{4\Lambda}\phi_0'^2\phi_0' r - 9e^{2\Lambda}\phi_0'^2\phi_0' r + \phi_0'^2\phi_0'e^{6\Lambda} r \\
& - 9e^{4\Lambda}\phi_0''\phi_0' r - 10e^{4\Lambda}\phi_0'\phi_0'' r + 11e^{2\Lambda}\phi_0''\phi_0' r + 12e^{2\Lambda}\phi_0'\phi_0'' r + \phi_0''\phi_0'e^{6\Lambda} r - 9\phi_0'\Lambda'\phi_0' r \\
& + 11e^{2\Lambda}\phi_0'\phi_0' - 3e^{4\Lambda}\phi_0'\phi_0' + 2\phi_0''e^{6\Lambda} - 3\phi_0''\phi_0' r - 12\phi_0'^2\phi_0'' r^2 - 10e^{2\Lambda}\Lambda'\phi_0' + 46e^{2\Lambda}\phi_0'^3 r \\
& - 30\phi_0'\phi_0'^3 r^2 + 5\phi_0'^2\phi_0' r \left. \right] \left(\frac{d\mathcal{F}}{d\phi_0} \right)^2 \left(\frac{d^2\mathcal{F}}{d\phi_0^2} \right) + 8e^{2\Lambda}\phi_0'^3 \left[-2e^{4\Lambda}\phi_0'^2 r^2 + 8e^{2\Lambda}\phi_0'^2 r^2 \right. \\
& - 6\phi_0'^2 r^2 + 2e^{4\Lambda}\phi_0' r - 20e^{2\Lambda}\phi_0' r + 18\phi_0' r + e^{6\Lambda} - 5e^{4\Lambda} + 7e^{2\Lambda} - 3 \left. \right] \left(\frac{d\mathcal{F}}{d\phi_0} \right)^2 \left(\frac{d^3\mathcal{F}}{d\phi_0^3} \right) \\
& - 8e^{2\Lambda} \left[3\phi_0'\phi_0'' + e^{4\Lambda}\phi_0'\phi_0'' + 7e^{2\Lambda}\phi_0''\phi_0' - 2e^{2\Lambda}\phi_0'^2\phi_0' - 5e^{2\Lambda}\phi_0'\phi_0'' + \phi_0'\phi_0''e^{6\Lambda} \right. \\
& + 2\phi_0'^2\phi_0'e^{6\Lambda} - 5e^{4\Lambda}\phi_0''\phi_0' + 6\phi_0'\Lambda'\phi_0' - 16e^{4\Lambda}\phi_0'\Lambda'\phi_0'^3 r^2 + 4e^{2\Lambda}\phi_0'\Lambda'\phi_0'^3 r^2 \\
& + 6e^{4\Lambda}\phi_0'\phi_0'^2\phi_0'' r^2 - 12e^{2\Lambda}\phi_0'\phi_0'^2\phi_0'' r^2 + 10e^{4\Lambda}\phi_0'^2\Lambda'\phi_0' r - 8e^{2\Lambda}\phi_0'^2\Lambda'\phi_0' r - 4e^{4\Lambda}\phi_0''\phi_0'\phi_0' r \\
& - 8e^{2\Lambda}\phi_0''\phi_0'\phi_0' r - 6\phi_0''\phi_0'^3 r^2 - 14\phi_0'^2\phi_0'' r + 6\phi_0'^3\phi_0' r - 3\phi_0''\phi_0' - 10e^{4\Lambda}\phi_0'\phi_0'^3 r \\
& - 4e^{2\Lambda}\phi_0'^3\phi_0' r + 22e^{2\Lambda}\phi_0'\phi_0'^3 r - 10e^{4\Lambda}\phi_0'^2\phi_0'' r + 24e^{2\Lambda}\phi_0'^2\phi_0'' r - 8e^{2\Lambda}\phi_0'^2\phi_0'^3 r^2 \\
& + 12\phi_0'\Lambda'\phi_0'^3 r^2 + 6\phi_0'\phi_0'^2\phi_0'' r^2 - 18\phi_0'^2\Lambda'\phi_0' r + 12\phi_0''\phi_0'\phi_0' r + 2e^{4\Lambda}\phi_0''\phi_0'^3 r^2 - 4e^{2\Lambda}\phi_0''\phi_0'^3 r^2 \\
& + 2e^{6\Lambda}\phi_0'\phi_0'^3 r - 2e^{4\Lambda}\phi_0'^3\phi_0' r - 6\phi_0'\Lambda'\phi_0'e^{6\Lambda} + 10e^{4\Lambda}\phi_0'\Lambda'\phi_0' \\
& - 10e^{2\Lambda}\phi_0'\Lambda'\phi_0' + \phi_0''\phi_0'e^{6\Lambda} - 30\phi_0'\phi_0'^3 r \left. \right] \left(\frac{d\mathcal{F}}{d\phi_0} \right)^3 \\
D_8 = & -32\phi_0'^4\phi_0' \left[3e^{6\Lambda} - 13e^{4\Lambda} + 25e^{2\Lambda} - 15 \right] \left(\frac{d\mathcal{F}}{d\phi_0} \right)^2 \left(\frac{d^2\mathcal{F}}{d\phi_0^2} \right)^2 \\
& - 32\phi_0'^4\phi_0' \left(e^{6\Lambda} - e^{4\Lambda} - 9e^{2\Lambda} + 9 \right) \left(\frac{d\mathcal{F}}{d\phi_0} \right)^3 \left(\frac{d^3\mathcal{F}}{d\phi_0^3} \right) - 64\phi_0'^2 \left[-\phi_0'^2\phi_0'e^{6\Lambda} \right. \\
& - 5\phi_0'\Lambda'\phi_0'e^{6\Lambda} + 3e^{4\Lambda}\phi_0'^2\phi_0' + 10e^{4\Lambda}\phi_0'\Lambda'\phi_0' - 5e^{2\Lambda}\phi_0'^2\phi_0' - 9e^{2\Lambda}\phi_0'\Lambda'\phi_0' \\
& + \phi_0''\phi_0'e^{6\Lambda} + 2\phi_0'\phi_0''e^{6\Lambda} - 4e^{4\Lambda}\phi_0''\phi_0' - 7e^{4\Lambda}\phi_0'\phi_0'' + 3e^{2\Lambda}\phi_0''\phi_0' + 8e^{2\Lambda}\phi_0'\phi_0'' \\
& + 3\phi_0'^2\phi_0' - 3\phi_0'\phi_0'' \left. \right] \left(\frac{d\mathcal{F}}{d\phi_0} \right)^3 \left(\frac{d^2\mathcal{F}}{d\phi_0^2} \right) + 64\phi_0'\phi_0' \left[\phi_0'^2\phi_0'e^{6\Lambda} - 5\phi_0'\Lambda'\phi_0'e^{6\Lambda} \right. \\
& - 4e^{4\Lambda}\phi_0'^2\phi_0' + 10e^{4\Lambda}\phi_0'\Lambda'\phi_0' + 3e^{2\Lambda}\phi_0'^2\phi_0' - 9e^{2\Lambda}\phi_0'\Lambda'\phi_0' + 2\phi_0''\phi_0'e^{6\Lambda} \\
& + \phi_0'\phi_0''e^{6\Lambda} - 8e^{4\Lambda}\phi_0''\phi_0' - 3e^{4\Lambda}\phi_0'\phi_0'' + 6e^{2\Lambda}\phi_0''\phi_0' + 5e^{2\Lambda}\phi_0'\phi_0'' - 3\phi_0'\phi_0'' \left. \right] \left(\frac{d\mathcal{F}}{d\phi_0} \right)^4
\end{aligned}$$

B Gravitational Waves

Here we provide a very rapid overview of gravitational waves (GW) from a theoretical point of view for the sake of completeness, in order to let the reader better understand the conclusions Chap. 5 of this work.

Gravitational waves are perturbations of space-time which propagate through the space-time itself at the speed of light. At linear level, we consider the metric as $g_{\mu\nu} = g_{\mu\nu}^0 + h_{\mu\nu}$, with a perturbation $h_{\mu\nu}$ much smaller than the background static metric $|h_{\mu\nu}| \ll |g_{\mu\nu}^0|$. Inserting this expression in Einstein equations of GR Eq. 2.20 we find

$$\begin{cases} \square \bar{h}_{\mu\nu} = -\frac{16\pi G}{c^4} T_{\mu\nu} \\ \partial_\mu \bar{h}^\mu_\nu = 0 \end{cases} \quad (\text{B.1})$$

with $\bar{h}_{\mu\nu} = h_{\mu\nu} - \frac{1}{2}g_{\mu\nu}^0 h$ and the second equation being the harmonic gauge condition [16]. We can then demonstrate that gravitational waves have only two degrees of freedom, corresponding to two different polarizations. These are clearly manifest for the choice of the TT gauge, i.e. in the gauge where the perturbation tensor is traceless (the first T) and transverse (second T), perpendicular to the direction of motion.

If the stress-energy tensor is well defined, it is possible to write the solution of the wave equation Eq. B.1 via the *quadrupole formula*

$$\begin{aligned} \bar{h}^{\mu 0} &= 0 \\ \bar{h}^{ij} &= \frac{2G}{c^4 r} \frac{d^2}{dt^2} q^{ij}(t - r/c) \end{aligned} \quad (\text{B.2})$$

where Greek indexes run from 0 to 3, while Latin ones from 1 to 3. q^{ij} is the quadrupole moment of the source, defined as

$$q^{ij} = \frac{1}{c^2} \int_V d^3x \left(T^{00}(t, \mathbf{x}) x^i x^j \right). \quad (\text{B.3})$$

Hence if the system does not present a non-trivial quadrupole moment, no gravitational waves are emitted.

The energy flux associated to gravitational waves, averaged over several wavelengths, can be expressed as

$$\frac{dE_{GW}}{dt dS} = \frac{G}{8\pi c^5 r^2} \left\langle \sum_{i,j} \left(\ddot{Q}_{jk}^{TT} \left(t - \frac{r}{c} \right) \right)^2 \right\rangle \quad (\text{B.4})$$

where \ddot{Q}_{jk}^{TT} is the third time derivative of the quadrupole moment of the source projected onto the TT gauge.

Integrating over the solid angle we can compute the gravitational wave luminosity L_{GW} , which is the energy emitted per unit time in the form of gravitational waves. When considering a binary system of two compact objects we have

$$L_{GW} = \frac{32}{5} \frac{G^4}{c^5} \frac{\mu^2 M^3}{a^5} \quad (\text{B.5})$$

with M being the total mass of the system $M = m_1 + m_2$, μ the reduced mass $\mu = \frac{m_1 m_2}{M}$, and a the orbital distance.

In the adiabatic regime where orbital parameters do not change significantly over a large number of periods (very far from merging), in the inspiral phase, the energy lost through gravitational wave emission is compensated by orbital rotational energy decreasing

$$\frac{dE_{orb}}{dt} = -L_{GW}. \quad (\text{B.6})$$

Considering circular orbit approximation, we can show that the temporal evolution of the orbital distance is given by

$$a(t) = a^{in} \left(1 - \frac{t}{t_c}\right)^{1/4} \quad (\text{B.7})$$

where a^{in} is the initial orbital distance and t_c is the time to coalescence $t_c = \frac{5}{256} \frac{c^5}{G^3} \frac{(a^{in})^4}{\mu M^2}$. Additionally, the Keplerian frequency of the inspiral motion, which is half of the frequency of the GW emitted, and the period of the orbit have time evolution expressed as

$$\omega_K(t) = \omega_K^{in} \left(1 - \frac{t}{t_c}\right)^{-3/8} = \frac{(GM)^{1/2}}{(a^{in})^{3/2}} \left(1 - \frac{t}{t_c}\right)^{-3/8} \quad (\text{B.8})$$

$$P(t) = \frac{2\pi}{\omega_K^{in}} \left(1 - \frac{t}{t_c}\right)^{3/8}. \quad (\text{B.9})$$

Thus we find out that the inspiral motion is characterized in time by decreasing period and orbital distance while increasing frequency, as expected.

Hence, during the **inspiral** phase, the two bodies lose energy and angular momentum due to the emission of gravitational waves, and the orbit shrinks, but they go through a sequence of stationary circular orbits, as far as the adiabatic approximation holds. The amplitude of the emitted gravitational waves increases as the two bodies get closer as

$$h_0(t) = \frac{4\pi^4 G^{5/3} \mathcal{M}^{5/3}}{r c^4} v_{GW}^{2/3} \quad (\text{B.10})$$

where $\mathcal{M} = \mu^{3/5} M^{2/5}$ is the so-called *chirp mass* of the system and $v_{GW} = 2\omega$ is the frequency of the emitted gravitational wave.

After the two body reach the ISCO³ the system becomes highly non-linear and we need to include more terms of higher power in (v/c) to the waveform formula Eq. B.2 derived above. However, the frequency keeps on increasing and the amplitude either until the coalescence is completed in the **merger** phase, a fully non-linear regime whose solutions can only be found numerically. This is the only scenario that provides us insights of strong-field regime through GW analysis by present and upcoming interferometers.

Ultimately, the remnant of the coalescence is a black hole that oscillates during the final phase, known as **ringdown**. During this phase, the black hole relaxes to a stationary state, emitting a gravitational wave (GW) signal characterized by a quasi-normal mode spectrum. The frequency and damping time of these modes are determined by the mass and angular momentum of the resulting black hole.

³Innermost Stable Circular Orbit, that corresponds to $r_{ISCO} = \frac{6GM}{c^2}$ for non spinning BHs